

DETECTING TIDAL DISRUPTION EVENTS WITH GAIA

David Lynn
11436328

This thesis is submitted to University College Dublin in fulfilment of the requirements for the degree of Research Masters.

School of Physics,
Science Centre North,
University College Dublin

Head of School:
Prof. Martin Grunewald

Principal Supervisor:
Dr. Sheila McBreen

February 2017

For my parents

Contents

Abstract	v
Statement of Original Authorship	vii
Acknowledgements	viii
Acronyms	x
List of Figures	xii
List of Tables	xiv
1 Introduction	1
2 Tidal Disruption Events	4
2.1 Black holes	4
2.1.1 Schwarzschild radius	4
2.1.2 Phenomenology	5
2.1.3 Distinctions	5
2.2 Accretion	7
2.2.1 Mechanics	8
2.2.2 Active galactic nuclei	8
2.3 Tidal disruption	10
2.3.1 Dynamics	10
2.3.2 Mass fallback rate	12
2.3.3 Accretion disk	13
2.3.4 Other features	15
2.4 Observation of TDEs	15
2.4.1 Photometry	16
2.4.2 Spectroscopy	17
2.4.3 Potential imposters	17
2.4.4 Current observation status	18
2.5 TDE rates	19
2.5.1 Theoretical vs measured rate	19
2.5.2 Galaxy bias	20
2.6 TDEs and Gaia	20

3	Gaia	23
3.1	Overview	23
3.2	Motivation	23
3.2.1	Hipparcos	23
3.2.2	Gaia	25
3.3	Spacecraft	26
3.3.1	Launch and operations	26
3.3.2	Payload module	30
3.3.3	Service modules	35
3.4	Instruments	35
3.4.1	The Sky Mapper	36
3.4.2	The astrometric instrument	37
3.4.3	The photometric instrument	37
3.4.4	The spectroscopic instrument	39
3.5	The astrometric solution	40
3.5.1	Parallax	40
3.5.2	Choice of geometry	42
3.5.3	AGIS	43
3.6	Mission science	44
3.6.1	Galactic structure and evolution	44
3.6.2	Variable stars	45
3.6.3	Binaries and exoplanets	45
3.6.4	Solar System	45
3.6.5	Extragalactic objects	46
3.7	Data products	46
3.7.1	Gaia photometric science alerts	46
3.7.2	GAVIP	47
4	Sample Generation and Simulation of Gaia Observations	49
4.1	Motivation	49
4.2	GIBIS	50
4.2.1	The Gaia Simulator	50
4.2.2	GIBIS operation	50
4.2.3	GIBIS input	51
4.3	Galaxy simulations	52
4.3.1	Galaxy samples	53
4.3.2	Galaxy simulation parameters	54
4.4	TDE simulations	59
4.4.1	Synthetic light curve	60
4.4.2	TDE simulation parameters	62
4.5	Performance of simulator	64
4.5.1	Simulation outputs	64
4.5.2	Preliminary simulations	66

4.5.3	Final simulations	68
5	Results	72
5.1	Galaxies	72
5.1.1	Ellipticals	73
5.1.2	Spirals	81
5.2	TDEs	87
5.2.1	Galaxy modelling	87
5.2.2	Detection efficiency	87
5.2.3	Detected brightness	88
5.2.4	Photometry	91
5.2.5	Potential of Gaia	100
6	Conclusions and Future Work	101
6.1	Summary conclusions	101
6.2	Future work	105
	Bibliography	107
	A Analysis	115

Abstract

The potential of Gaia for tidal disruption event (TDE) detection is investigated through simulation. Tidal disruption is the process whereby a star gets completely or partially torn apart by a black hole, generally a supermassive black hole at the centre of a galaxy. Half the disrupted debris forms an accretion disk and falls back onto the black hole at a rate of $t^{-5/3}$. This translates to a luminosity which rises to a peak and decays in a manner which tends to this $-5/3$ index power law. This luminosity decay has been observed at multiple wavelengths including the X-ray and optical bands. Many strong TDE candidates have been observed in the last number of years, particularly in optical transient surveys.

Gaia is a European Space Agency mission which has potential to detect TDEs. It was launched in 2013 after a decade and a half of planning. Gaia is primarily an astrometry mission which is making a map of approximately 1% of the Milky Way by measuring precise parallaxes over five years. Its focal plane consists of three instruments and almost one billion pixels. These instruments have astrometric, photometric and spectroscopic capabilities. Gaia continuously scans the sky recording data for objects brighter than 20.7th magnitude in its optical G band. Though the performance of Gaia has been optimised for point sources it is also detecting many extragalactic and transient objects. Many of these transients are released as they are observed so that photometric and spectroscopic follow-up may be performed, but many will not be released until the final Gaia data release, scheduled for 2023.

No TDE data have yet been released necessitating simulation. Simulations are carried out using the Gaia Instrument and Basic Image Simulator. This is an expansive Java simulation tool which was created to allow Gaia mission scientists to prepare for Gaia data, and to allow simulation of astrophysical sources which would not appear in the archive for several years. This tool facilitates simulation of Gaia's response to several predefined sources or a user-defined source. Galaxy simulations are carried out followed by TDE and galaxy simulations to investigate Gaia's response to these objects. Galaxy simulation parameters are chosen based on two samples taken from the SDSS database to give a broad representation of elliptical and spiral galaxies which could potentially harbour a TDE. TDE brightnesses are chosen by sampling from a synthetic light curve comprising a rise to a peak followed by a $t^{-5/3}$ decay.

The results of the galaxy and TDE simulations are presented and discussed. With 68% detected, elliptical galaxies have good detection potential down to 20th magnitude in the Johnson V band; however this figure is heavily dependent on the size of the galaxy. 0.5'' radius galaxies were observed down to 21st magnitude while 5'' radius galaxies were only observed to 18th

magnitude. This strong size dependence is due to the detection window which Gaia employs, optimised for point sources. This window is at largest $1.062'' \times 3.186''$. There is also a bias seen towards E7 and more elliptical galaxies. Spiral galaxy disks have a poor detection potential. This is seen through a relatively high detection efficiency for bulge dominated spirals which drops off with the bulge to total ratio of the galaxy. Overall 61% of the spirals were detected due to the bright bulges; as they are quite similar to ellipticals, spiral bulges have a high detection efficiency. A relationship between intrinsic galaxy parameters and equivalent Gaia window magnitude is derived.

The TDE light curves are folded through the Gaia detection process. Detection efficiency is quite high since these sources are a point source on top of an elliptical galaxy. After 500 days the detection efficiency was still 17% higher than before disruption (i.e. for just elliptical galaxies) indicating that bright TDEs may still be visible for 500 days and more after disruption. Unsampled light curves are presented to provide an overview of how Gaia responds to TDE light curves. Gaia's small window is advantageous in this regard as it focuses largely on the central point source. The light curves are fit with a $-5/3$ index power law and some other simple functions to investigate how the light curve is processed by Gaia and to simulate how one may look for TDEs in the Gaia archive. The power law provided a significantly better fit than the other functions. Though this will serve as a reduction criterion, the results will need to be investigated more rigorously for TDE characteristics. An arbitrary power law is also fit to investigate how Gaia processes the power law index. This returned a median index of -1.66 , indicating a very good match with the simulated data; however, this was seen to degrade with TDE peak luminosity indicating that Gaia may not be suitable for detection of very dim TDEs.

It is deemed that Gaia is suitable for detection of TDEs with peak magnitude above 16–18th magnitude. It is described how this work may be applied to detection of TDEs in the Gaia archive when it is released in full. Several suggestions are made to build on this work so that it may better be used to detect TDEs in the Gaia archive. In particular, supernovae, AGN and other transients will need to be filtered out.

Statement of Original Authorship

I hereby certify that the submitted work is my own work, was completed while registered as a candidate for the degree stated on the title page, and I have not obtained a degree elsewhere on the basis of the research presented in this submitted work.

David Lynn

Acknowledgements

Much love and gratitude to my parents and family for their unwavering support throughout the masters, the bachelor and even the stuff before then. I literally wouldn't be here without you.

Thank you to my supervisor Dr. Sheila McBreen for strong guidance and direction, both in getting started and throughout the project despite other important events! Thanks also to my enterprise mentor Prof. Lorraine Hanlon for support. And the rest Space Science group: Alexey, Antonio, Colin, Dave, Isaac, Maeve, Morgan, Oli and Sinead; you guys made the lab a more fun place to be, but also warmer. Special thanks to Ger for his bountiful support in the end despite having started a real job!

Thanks to the lunch crew: Andrew, Chris, Conor, Dave, Fionn, John, Sarah and Sean. It was always nice to know that no matter how bad a day I was having I could come down for lunch at one and get chastised over inconsequential things like not wearing a purple article of clothing. Special thanks to Shane for opening my mind to the vast number of ways to write the letter T, and for being sound.

I am grateful to the School of Physics and its inhabitants. Everyone is always very friendly and helpful. Thanks in particular to the admin staff: Bairbre, John and Sarah for putting up with my silly requests and for keeping the school running; and to the two Heads of School which served in my time: Prof. Pádraig Dunne, and Prof. Martin Grünewald.

Sincere thanks to Dr. Carine Babusiaux for running all GIBIS simulations and for many helpful discussions. Thanks also to DPAC, particularly Dr. Nadejda Blagorodnova and Dr. Diana Harrison for help in getting things going with the simulations and output parsing.

I wish to acknowledge funding from the Irish Research Council and Parameter Space Ltd. under the Enterprise Partnership Scheme (grant EPSPG/2015/26). Special thanks to Parameter Space for also giving me the opportunity to work within the company for several months. Cheers Dan, Derek, Fionn, Lorraine, Sean, Sheila and Sinead. I'm sure you will all continue to do great things.

Lots of love to my girl Sharon. You only came into my life a year ago but you've made the last year very special. We're often late for things but it's always because of me; you're always ready to go on time and it's one of the things I love about you. You're such a great listener and I feel like I could tell you anything without judgement or vilification, you don't even laugh at my singing! Sure we've had our bumps along the way: the incident with the deer, you banging

that cyclist, the NCT, and of course all the literal speed bumps, but I look forward to many more years together, until I replace you with a younger model.

This work has made use of SciPy and its many wonderful packages: NumPy, Matplotlib and pandas. This research has made use of NASA's Astrophysics Data System Bibliographic Services.

Acronyms

AC across-scan

AF Astrometric Field

AGIS the Astrometric Global Iterative Solution

AGN active galactic nucleus

Airbus DS Airbus Defense and Space

AL along-scan

ASTRO the astrometric instrument

AVI Added Value Interface

BAM basic angle monitor

BP Blue Photometer

CCD charge-coupled device

CNES le Centre national d'études spatiales

CSV comma separated value

DPA Deployable Sunshield Assembly

DPAC the Data Processing and Analysis Consortium

DR data release

ESA European Space Agency

ESAC the European Science Astronomy Centre

ESOC the European Science Operations Centre

FITS Flexible Image Transport System

FoV field of view

GASS the Gaia System Simulator

GAVIP the Gaia Added Value Interface Platform

GIBIS the Gaia Instrument and Basic Image Simulator

GOG the Gaia Object Generator

IDL Interactive Data Language

IMBH intermediate-mass black hole

ISM interstellar medium

MOC Missions Operations Centre

NSL nominal scanning law

PDHS payload data handling system

PMT photomultiplier tube

PSA Gaia Photometric Science Alerts

PSF point spread function

RP Red Photometer

RVS Radial Velocity Spectrometer

SDSS Sloan Digital Sky Survey

SED spectral energy distribution

SM Sky Mapper

SMBH supermassive black hole

SN supernova

SOC Scientific Operations Centre

SQL Structured Query Language

TDE tidal disruption event

TDI time-delay integration

TNO the Netherlands Organisation for Applied Scientific Research

VPA video processing algorithms

VPU video processing unit

WFS wave-front sensor

List of Figures

1.1	Refereed TDE papers published since 1997	2
2.1	Black hole from Interstellar	5
2.2	Orbits around Sgr A*	6
2.3	Unified AGN model	9
2.4	Tidal radius vs Schwarzschild radius	11
2.5	Basic dynamical picture of tidal disruption event	12
2.6	Simulations of TDE accretion giving desired fast fallback rate	14
2.7	Accretion TDE rates surpassing Eddington limit	14
2.8	Predicted TDE band luminosity decays	16
2.9	Strong TDE candidate detections to date	18
2.10	Light curve of PS1-10jh	19
2.11	Overrepresentation of TDEs in E+A galaxies	21
2.12	Brightness vs characteristic decay timescale of various transients	22
3.1	Gaia	24
3.2	Hipparcos	24
3.3	Focal plane of Hipparcos	25
3.4	Gaia's Lissajous orbit around L2	27
3.5	Gaia's nominal scanning law	29
3.6	Gaia's response loss due to water ice sublimation over time	30
3.7	Fibres in sunshield blanket which cause Gaia's straylight problem	31
3.8	Light path from two lines of sight in Gaia. Image from Charvet (2006).	31
3.9	Gaia focal plane	32
3.10	Gaia basic angle monitor bars	34
3.11	Gaia electrical service module	35
3.12	Gaia instrument bandpasses	36
3.13	Gaia astrometric field detection windows	38
3.14	Gaia BP and RP dispersive optics	39
3.15	Gaia RVS optics	40
3.16	Distance from parallax	41
3.17	Geometry of Gaia	42
3.18	Resonances in choice of basic angle	43
4.1	Structure of Gaia Simulator	51

4.2	Elliptical and spiral galaxy colours	55
4.3	Galaxy radii	57
4.4	Disk vs bulge radius	57
4.5	Hubble tuning fork	58
4.6	Disk vs bulge position angle	59
4.7	Hyperbolic tangent function	60
4.8	Synthetic TDE light curve	62
4.9	Light curve sampling	63
4.10	GIBIS output image	64
4.11	Detection windows	65
4.12	Higher detection rate at end of light curve	66
4.13	Coordinate bias in preliminary simulations	67
4.14	Detection bias in final simulations	69
4.15	Detection bias focused in bright galaxies	70
5.1	Elliptical detection efficiency for R vs V	73
5.2	Elliptical efficiency vs literature	74
5.3	Elliptical detection efficiency per input parameters	75
5.4	Detection efficiency across position angle	76
5.5	Elliptical intrinsic vs detected G magnitude	77
5.6	Elliptical intrinsic vs detected G magnitude separated by radius	78
5.7	Normal distribution fit to detected G magnitude data in ellipticals	79
5.8	Detection efficiency per input parameters	82
5.9	Spiral detection efficiency for B/T vs V	83
5.10	Spiral intrinsic vs detected G magnitude	84
5.11	Spiral intrinsic vs detected G magnitude separated by radius	85
5.12	Normal distribution fit to detected G magnitude data in spirals	85
5.13	TDE detection efficiency per input parameters	89
5.14	TDE detection efficiency variation with time	90
5.15	TDE intrinsic vs detected G magnitude	90
5.16	TDE intrinsic vs detected G magnitude separated by radius	91
5.17	Input vs detected unsampled light curves	92
5.18	Selection of high, medium and low sampled light curves	94
5.19	Light curve fits	97
5.20	Best-fit power law indices	98

List of Tables

4.1	Simulation detection efficiency for various spacings	68
5.1	Empirical relation between elliptical intrinsic parameters and detected G magnitude	80
5.3	Empirical relation between spiral intrinsic parameters and detected G magnitude	86
5.5	Interpolated galaxy detected Gaia magnitudes	95
5.6	Goodness of fit for exponential and linear functions relative to power law	96
5.7	Best-fit power law indices for each source parameter	99

Chapter 1

Introduction

A tidal disruption event (TDE) occurs when a star gets ripped apart by the tidal forces of a black hole and produces a flare. TDEs were first theorised in the late 1970s as the the existence of a supermassive black hole (SMBH) at the centre of galaxies became widely accepted. Rees (1988) and Phinney (1989) laid the theoretical groundwork, predicting the canonical $t^{-5/3}$ mass fallback rate, which has acted as the primary TDE ‘smoking gun’ since then. Several more papers were published in the following years, notably Evans and Kochanek (1989) gave some insights into the hydrodynamics and accretion physics present. From an observational standpoint, however, the field remained virtually uninhabited until the late 1990s when the *ROSAT* survey (Trümper 1982) made some promising X-ray observations. The observations taken were relatively poorly sampled but showed promise for TDEs and demonstrated that these events could be observed.

This marked the birth of TDE astronomy, inspiring searches in other telescopes, including a search by Gezari et al. (2008) with the ultraviolet telescope *GALEX* which yielded similarly successful results. Theoretical work continued with several estimates on the rates at which these events occur, particularly by Wang and Merritt (2004). From the early 2010s, observations branched out into other bands with *Swift* returning some events. In the last number of years, however, with the advent of dedicated optical transient surveys such as *PTF* and *ASAS-SN*, optical telescopes have been the discovery powerhouses.

With more strong candidates garnering interest from the scientific community, interest in the area has increased dramatically, both from a theoretical side as observations allow models to be better constrained, and from an observational side as new strategies to detect these events are developed. Figure 1.1 shows a histogram of refereed papers published since 1997, illustrating the dramatic increase in interest in the field. As technology continues to advance and more optical survey instruments come online, many more TDE candidates are expected, with suggestions from Gezari (2016) of 1000s of TDEs to be discovered in the *Large Synoptic Sky Survey*.

TDEs provide unique testbeds for black hole and accretion physics which are otherwise difficult topics to probe. Much is still speculative and much is still unknown in this field, with theory and observation taking turns to lead each other. In particular the exact processes occurring

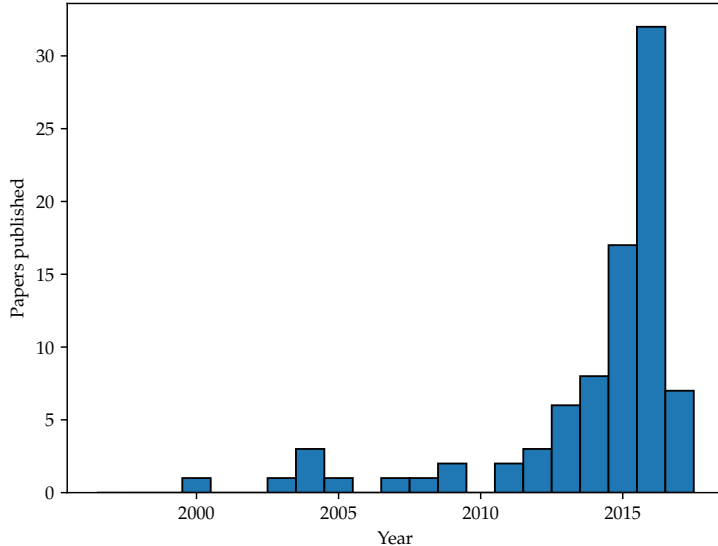


Figure 1.1: Refereed papers published with “tidal disruption event” in the title since 1997 showing a large increase in the last five years. Data retrieved from *The SAO/NASA Astrophysics Data System*, February 2017.

in the accretion disk remain uncertain, with a flurry of papers being published recently (e.g. Bonnerot, Rossi, Lodato and Price 2016; Piran et al. 2015; Shiokawa et al. 2015) in an effort to account for the uncharacteristically slow speed which theory predicted the accretion disk should circularise.

Among the instruments which has the potential to discover many TDEs is Gaia. Gaia is a unique European Space Agency (ESA) mission whose primary function is to make a map of 1% of the stars in the Milky Way. Gaia was incepted in the late 90s by Lindegren and Perryman (1997) as a successor to the revolutionary Hipparcos mission. The methodology behind Gaia is the same as was employed by the Hipparcos mission but twenty years of technological advances allow for massive increases in performance. Gaia was developed and constructed through the 2000s and finally launched in 2013 to its orbit around the second Lagrange point of the Sun-Earth system.

Gaia consists of two folded telescopes which simultaneously observe two separate regions of the sky and focus light onto a common focal plane. This focal plane consists of an array of charge-coupled devices (CCDs) comprising approximately one billion pixels, and is the most sophisticated camera ever launched into space. It contains an astrometric instrument, a photometric instrument and a spectroscopic instrument. Gaia continually surveys the universe as it rotates and precesses in orbit, building up a picture of the entire night sky. Due to the sophistication of the instruments, an optimised binning and windowing system is employed so that only potentially useful science is committed to the data. Even with these measures, the amount of data produced will be enormous.

Due to the nature of the astrometric solution which Gaia will employ, most data are released into an archive in slow stages. This will allow the star positions to be well constrained but is not

ideal for transient astronomy. However, Gaia has many other redeeming qualities for transient, and specifically TDE, astronomy. Its astrometry will allow extragalactic sources to be placed within a galaxy more precisely; its average cadence of approximately 30 days make it suitable for observing TDE decays; it will also produce spectra for every observation.

Transients initially identified with Gaia by detecting brightness changes are released as they are detected. This scenario is ideal as photometric and spectroscopic follow up can be achieved with other transient-optimised systems. However, a large fraction of transients are expected to miss this identification and enter the final archive unidentified. This will leave many TDEs unidentified in the Gaia archive with potentially well-sampled light curves.

This thesis presents work which was undertaken to explore the potential for TDE detection in the Gaia archive. As Gaia has a very unique response to sources, particularly extended sources, these objects are investigated using simulations. Galaxies are simulated on their own to provide insight into their response, followed by TDEs within galaxies. Gaia's response to the TDE light curve is of particular interest. The responses are presented and a simple method for potentially pulling TDE-like sources out of the archive for further analysis when they are available is explored.

Chapter 2 provides a description of some of the science motivating TDE interest and an account of TDEs themselves, including current theory and observation status. Chapter 3 details the Gaia mission which is important for understanding its response to the objects of interest. An account of the simulations performed is provided in Chapter 4, including the workings of the simulator and the motivation for the parameters chosen. This chapter also evaluates the performance of the simulator and presents its limitations. Chapter 5 presents and discusses the results of the simulations in the context of detecting galaxies and TDEs with Gaia. Conclusions and suggestion for future work are presented in Chapter 6.

A convention is used throughout this thesis whereby in all histograms resulting from simulations, green represents total simulated data, i.e. the sources which were folded through the simulator, and blue represents detected data, i.e. the sources which were simulated as detected by Gaia.

Chapter 2

Tidal Disruption Events

2.1 Black holes

A *black hole* is a massive object whose mass is large enough that light cannot escape its gravitational pull, i.e. its escape velocity is greater than the speed of light (e.g. Wald 1984).

2.1.1 Schwarzschild radius

The spherical region surrounding a black hole from which light cannot escape is known as the event horizon. Although classically light does not interact gravitationally, it is possible to derive the event horizon radius using a classical argument by deriving the radius at which an object's escape velocity is greater than the speed of light. This classical result happens to agree with the relativistic solution.

General relativity posits that gravity comes about as a result of the curvature of spacetime and couples to all forms of energy, including light, and this is why light is also unable to escape a black hole (e.g. Thorne 1995). General relativity is governed by the Einstein Field Equations. Schwarzschild discovered a solution to these equations in 1916 for a spherical, uncharged, unspinning mass, and found a physical singularity at the origin (Schwarzschild 1999). The event horizon around this singularity is at the *Schwarzschild radius*:

$$R_S \equiv \frac{2GM}{c^2}. \quad (2.1)$$

There are several other solutions to the field equations describing spinning and charged black holes which have different event horizons. Astrophysical objects are generally uncharged; however, spinning black holes are seen and are described by the Kerr solution (Kerr 1963). As no light escapes from beyond this radius, these objects are very difficult to observe and thus incredibly elusive. Though Einstein's general relativity predicted their existence, he himself did not believe they could form (Einstein 1939).

2.1.2 Phenomenology

Einstein did not like the idea of black holes¹ due to the singularity at their centre. Everything which crosses the event horizon eventually meets its end at this singularity (e.g. Wald 1984). This very dense object leads to extreme tidal forces capable of ripping apart other astrophysical bodies. As nothing can escape the event horizon, three parameters fully classify the black hole, which are the mass (seen in gravitational effects on nearby stars and accretion), charge (would be seen in electrostatic effects on nearby charged bodies) and angular momentum (seen in frame dragging). These three parameters contain all the information one can hope to obtain about a black hole; this is known as the no-hair theorem (Misner et al. 1973).

The existence of black holes can only be inferred using one of these three parameters, usually mass; though spin characteristics may also be observed (e.g. Reynolds and Fabian 2008). These parameters may lead to phenomena such as gravitational lensing (e.g. Fig. 2.1), accretion disks (discussed later), and *Hawking radiation*—a form of radiation emitted as a result of quantum mechanical effects near the event horizon (Hawking 1975). As the gravitational potential energy near a black hole is so large, these effects often result in emission of X-rays. Black holes are generally ‘observed’ through the dynamics of nearby orbiting matter (Freedman 2016).

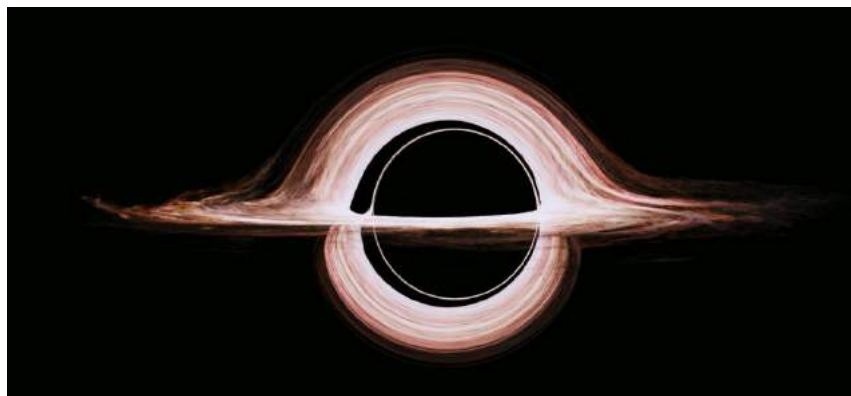


Figure 2.1: Image of a black hole portrayed in the movie Interstellar. This image was the result of computationally intense simulations (James et al. 2015) and provides an extremely accurate depiction of how a black hole would look to a nearby observer. The accretion disk can be seen to bend around the event horizon in an unusual way due to gravitational lensing.

2.1.3 Distinctions

Stellar mass black holes

Stellar mass black holes form from the gravitational collapse of an evolved massive star. Their masses range from about 5 to tens of solar masses (Özel et al. 2010), with the merger of two black holes around 30 solar masses leading to the first detection of gravitational waves (Abbott et al. 2016). Gravitational collapse occurs in all stars when their fusionable material is depleted and hydrostatic equilibrium is overcome as gravity starts to dominate. In the case of low-mass

¹He is quoted as saying they didn’t “smell right” (Thorne 1995).

stars, such as the Sun, this collapse will result in a *white dwarf* which will slowly radiate its thermal energy over time (Ostlie and Carroll 2007). *Neutron stars* form from the collapse of the lower range of high-mass stars. The highest mass stars may collapse with the formation of a black hole. This is usually preceded by a supernova where a lot of the matter is ejected away (Shapiro and Teukolsky 2004).

As stellar mass black holes are the inevitable end to a very high mass star's life, they are widely distributed in a galaxy. However, they are very difficult to detect on their own as they are not massive enough to wildly distort the orbit of nearby objects. They can exist within a binary system where they accrete matter from a nearby star. The accretion disc emits energy particularly in the form of X-rays which can be detected (Shapiro and Teukolsky 2004). It is possible for tidal disruption to occur around a stellar mass black hole; however, this is very unlikely due to the lack of the high stellar densities within its sphere of influence. It is important to mention them but stellar mass black holes will not be further considered in this thesis.

Supermassive black holes

SMBHs have masses on the order of 10^5 to 10^9 solar masses. There is a SMBH at the centre of our own galaxy and, it is believed, at the centre of most galaxies (Melia 2003). The black hole at the centre of the Milky Way is known as Sagittarius A* and has a mass of $4.02(16) \times 10^6 M_\odot$ (Boehle et al. 2016). This mass was inferred from the orbital dynamics of the surrounding stars. The orbits of six stars around Sgr A* are traced in Fig. 2.2. This method is generally not possible for distant galaxies where individual stars in the nucleus cannot be resolved.

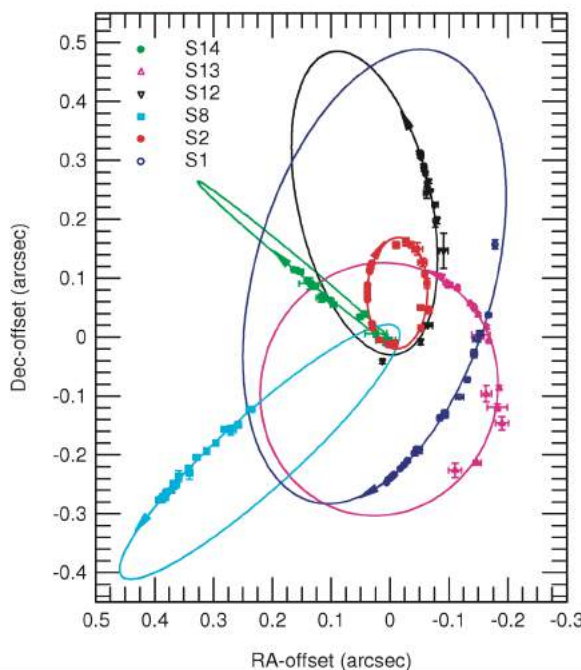


Figure 2.2: Orbits of six stars around Sgr A* which infer the existence of a very massive object at the centre of the galaxy. Image from Eisenhauer et al. 2005.

There is much uncertainty surrounding the formation of SMBHs and the topic is very preva-

lent in current research² (e.g. Bower et al. 2006). By looking into the universe, *quasars* (accreting SMBHs that are very luminous) can be seen out to redshift 7, suggesting that they may have formed first; however, it may be possible that some galaxies formed first with the central SMBH forming from collapsed matter within the galaxy over billions of years (Silk and Rees 1998). How and when black holes formed is an open question. It is generally believed that the formation of the SMBH and galaxy bulge are strongly linked. This is supported by the fact that the central SMBH and bulge stellar population are heavily correlated: The mass of the black hole is approximately 0.1% of the bulge mass. The velocity dispersion of the bulge stars is also related to the mass of the central SMBH through the *M- σ relation* (Gebhardt et al. 2000).

Intermediate mass black holes

Many supermassive and stellar mass black holes have now been discovered but few detections have been claimed of a mass between these two classes, and recently the question has been asked “where are the intermediate-mass black holes?”. Several SMBH formation models suggest that these objects formed through a large accretion of matter over time (Volonteri et al. 2003). If this is the case then intermediate mass black holes should exist in other astrophysical environments such as globular clusters where accretion did not continue for long enough (Miller and Colbert 2004).

Intermediate mass black holes are black holes with a mass between that of stellar mass black holes and SMBHs, i.e. 10^2 to 10^4 solar masses (Miller and Colbert 2004). There have been observations of potential intermediate-mass black hole (IMBH) (e.g. Voss et al. 2011); however, solid evidence of an IMBH was discovered by Kiziltan et al. (2017) in a globular cluster, exhibiting characteristics of a $2200 M_{\odot}$ black hole. It is possible for tidal disruption to occur from an intermediate mass black hole, thus they provide a unique opportunity to discover and investigate them (Shcherbakov et al. 2013).

2.2 Accretion

Accretion is the gravitational collapse of matter onto another astrophysical object. It occurs in many astrophysical settings and is believed to be responsible for the formation of structured systems such as galaxies (Pudritz 2002) and planetary systems (Montmerle et al. 2006). It can also be an extremely efficient energy source which is responsible for many bright flaring events.

²“Which came first: the black hole or the galaxy?” has become somewhat of a causal dilemma akin to the chicken and the egg.

2.2.1 Mechanics

Energy source

The gravitational potential energy released in accretion onto a body is given by

$$\Delta E = \frac{GM_*m}{R_*},$$

where M_* and R_* are the mass and radius of the accreting body respectively (Frank et al. 2002). It can be seen that the energy released is proportional to the compactness of the accreting object. Hydrogen burning yields an energy

$$\Delta E = 0.007mc^2.$$

Comparing these two mechanisms, it can be seen that for compact objects such as black holes and neutron stars accretion is the dominant energy release mechanism (Frank et al. 2002). This is the driving force behind X-ray binaries, where accretion leads to emission of high-energy electromagnetic radiation in the form of X-rays (Tauris and van den Heuvel 2003). Although hydrogen burning yields a higher energy over accretion in White Dwarfs, accretion often occurs on shorter timescales producing very bright flares in, for example, cataclysmic variables (Downes et al. 1997).

Matter is accreted in a disk perpendicular to the axis of rotation, due to gravitational flattening. These accretion disks comprise very fast moving particles which spiral in towards the central mass. The speeds of these particles are such that they are very hot. For a neutron star, the *Virial* temperature would be of order 10^{12} K; effective temperatures are typically around 10^7 K and release blackbody radiation to this effect (Spruit 2014). In accretion disks energy may be extracted from the particles and put into jets ejected from the object poles (see for example Netzer 2015 and references therein).

Eddington limit

The Eddington limit is the luminosity of an object, beyond which radiation pressure would exceed gravitational pressure of the object. This limit may also be applied to accretion where there is an inward pressure from the infalling material and an associated outward radiation pressure (Frank et al. 2002). If the radiation pressure exceeds the accretion pressure then accretion will cease. It is possible for objects to exceed the Eddington limit when spherical symmetry is broken and jets are emitted, or in bursts. Accretion rates beyond this limit, i.e. *super-Eddington* accretion rates, are believed to occur in many phenomena, such as active galactic nuclei (AGN) (discussed in the next section) and TDEs (Komossa 2015).

2.2.2 Active galactic nuclei

AGN are compact regions at the centre of otherwise normal galaxies which emit an inordinate amount of electromagnetic radiation. Their luminosities are such that they can be seen to great

distances, and are among the most distant objects observed in the sky (Mortlock et al. 2011); these high luminosities can be distributed across the entire electromagnetic spectrum (Volker and Shrader 2012). They are also often quite variable, depending on the sub-classification of AGN. AGN spectra also portray broad and narrow emission lines, and an overall blue colour (Jones and Lambourne 2007). These high luminosities and spectral features point to an extremely energetic environment.

A SMBH is widely believed to be the central engine of AGN. Through accretion processes described previously, vast amounts of gravitational energy are released in the vicinity of a black hole. Surrounding these SMBHs is a very hot accretion disk which can give rise to powerful jets (Volker and Shrader 2012). An *obscuring torus* accounts for the reprocessing giving lower energy emission. AGN are divided into several sub-classifications, which are unified under a single model; depending on the relative location of an observer, one may see a different type, as illustrated in Fig. 2.3. AGN are somewhat rare in the local universe compared to the distant (past) universe causing some to wonder if some galaxies are active and some are not, or if active is simply a phase that some or all galaxies go through (Jones and Lambourne 2007).

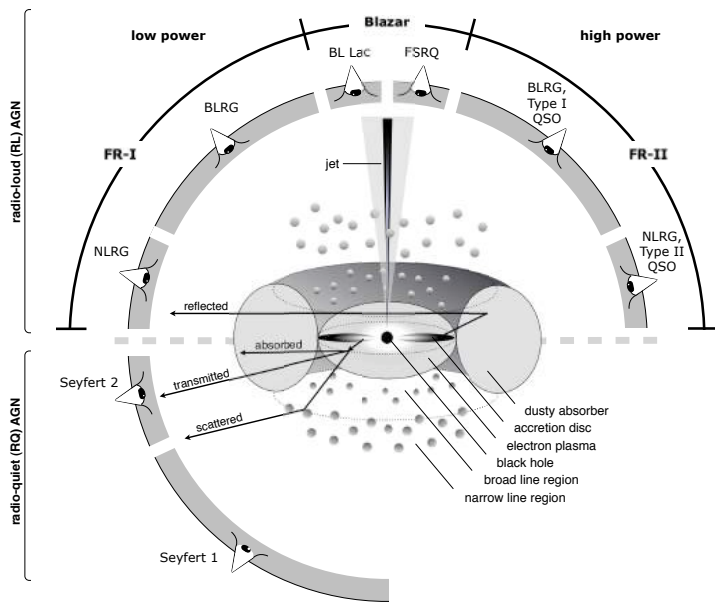


Figure 2.3: AGN model with black hole at its centre showing key observational features and types. The angle at which the AGN is observed affects the features seen, and thus can lead to a very different looking object; e.g. if an observer views the above figure from the top, they will see a bright jet, and would classify it as a *blazar*. The model does however discern radio-loud and radio-quiet AGN as separate types. Image from Volker and Shrader (2012).

As TDEs are described in the following sections, many similarities may be seen between them and AGN, and indeed one of the motivations for studying TDEs is to provide insight into black holes in quiescent galaxies. These similarities are useful in developing TDE physics, which is still very young, but may lead to confusion between these sources (e.g. Saxton et al. 2015). This is sensible since both occur as a result of accretion around a SMBH at the centre of a galaxy.

Thus both are seen as bright sources at the centre of a galaxy, and may exhibit similar spectral features. This is discussed further in later sections.

2.3 Tidal disruption

Despite the possibility for tidal disruption around all classes of black hole, all strong TDE candidates observed to date have been around SMBHs at the centre of galaxies. This thesis is concerned with these types of events and any future mention of black holes in this thesis will implicitly be referring to SMBHs unless explicitly stated.

2.3.1 Dynamics

The centre of most galaxies is widely believed to harbour a SMBH and millions to billions of orbiting stars (Laurikainen et al. 2016). The radius of the sphere of influence of a black hole is given by

$$r_h = \frac{GM_h}{\sigma^2}, \quad (2.2)$$

where σ is the central velocity dispersion (Peebles 1972). Using M_h and σ estimates from Gebhardt et al. (2000) puts the sphere of influence for Sgr A* at approximately 0.3 pc for example. Within this region, stars are influenced by the potential of the black hole, but also the potential of the other stars due to the very high stellar density. Stars are thus constantly being perturbed in orbital angular momentum around the SMBH and possess some probability of being perturbed into a *radial loss cone orbit*, where its trajectory takes it very close to the SMBH (Strubbe and Quataert 2009). The rate at which this occurs is discussed further in Section 2.5.

The *tidal radius* is the orbital radius at which the tidal forces exerted on a star from a black hole become comparable to the self gravity of the star (Hills 1975), i.e.

$$R_t = R_* \left(\frac{M_h}{M_*} \right)^{1/3}. \quad (2.3)$$

The exact radius at which the tidal forces overcome the star's self gravity also depend on the polytropic index of the star (Guillochon and Ramirez-Ruiz 2013); a polytrope (with a particular index) is a solution to the *Lane-Emden equation*, which describes the pressure and density of a star through fluid mechanics. There is a bias toward observable tidal disruption in low mass black holes: Equation (2.1) shows that the black hole event horizon scales linearly with black hole mass, whereas the tidal radius has just been shown to scale with black hole mass to the 1/3. There will thus be a black hole mass and solar mass pair where tidal disruption occurs within the black hole event horizon and is unobservable (MacLeod et al. 2012). This is illustrated in Fig. 2.4 for three different mass stars.

Defining a penetration factor as the ratio of the tidal radius to the stellar pericentre distance, i.e. the distance at which the star is closest to the black hole,

$$\beta \equiv \frac{R_p}{R_t},$$

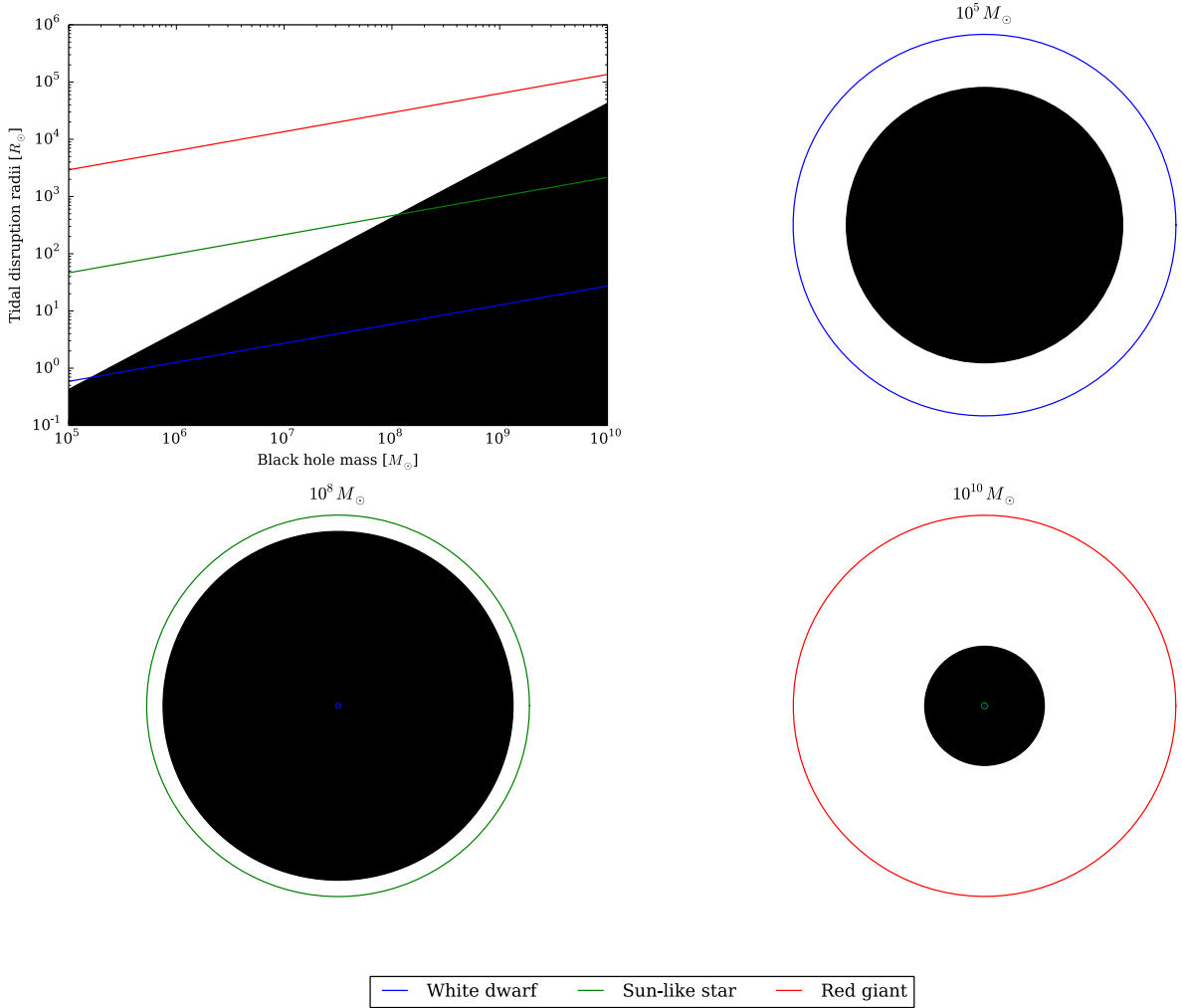


Figure 2.4: Tidal radius of various stellar types plotted with Schwarzschild radius. If the tidal radius is less than the Schwarzschild radius, i.e. if it falls inside the black region above, tidal disruption occurs inside the event horizon and will never be observed. Both are functions of black hole mass but R_S rises faster indicating a bias towards observable tidal disruption around lower mass black holes. For a 10^5 solar mass black hole all tidal radii above occur outside the event horizon (the tidal radius of a white dwarf falls just outside), while for a 10^{10} solar mass black hole, only tidal disruption of red giants may be observed. Note that these tidal disruption orbits are calculated by plugging typical values into Eq. (2.3), but in reality would also depend on the the polytropic index of the star.

the strength of the tidal disruption is given by this factor (Stone 2015). If the star is completely disrupted in the process then half of the debris enters a bound orbit where it is eventually accreted onto the black hole, and half is ejected in an unbound hyperbolic orbit (Rees 1988). This is the classic picture of tidal disruption and is portrayed in Fig. 2.5. Guillochon and Ramirez-Ruiz (2013) showed that these interactions are often weak and the star is often not completely disrupted, leaving behind a surviving core which may come back around to be disrupted again. The bound material circularises and accretes onto the black hole, heating up in the process and producing a characteristic flare (discussed in Section 2.2). The unbound material is ejected and may interact with the interstellar medium (ISM) (discussed in Section 2.3.4).

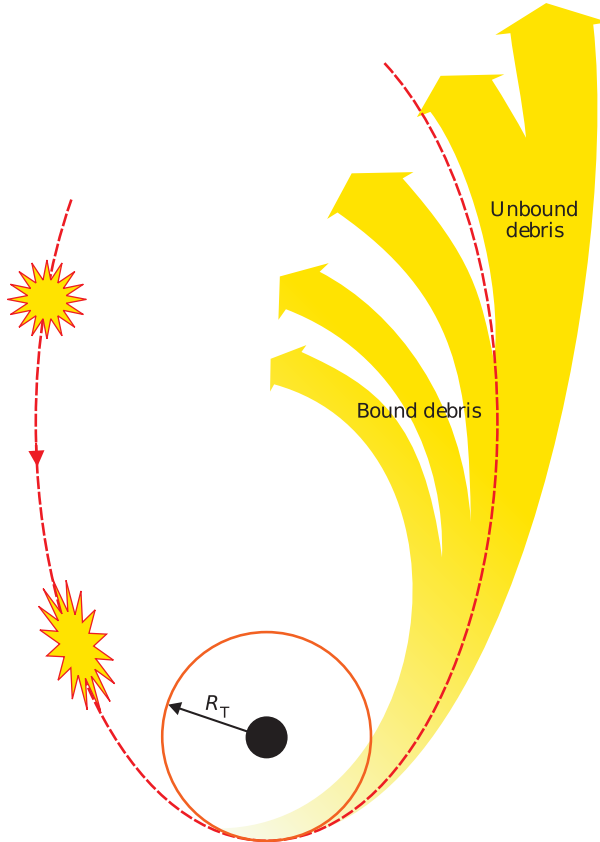


Figure 2.5: Basic dynamical picture of tidal disruption event showing star getting stretched as it approaches the tidal radius, and the remaining bound and unbound debris fields. A surviving core is not shown here but may be present after disruption. Image from Gezari (2014).

2.3.2 Mass fallback rate

Bound debris from tidal disruption falls back onto the black hole on roughly ballistic trajectories (Stone 2015). The mass fallback rate has been subject to notability since its derivation by Rees (1988). Rees mistakenly concluded that $\dot{M} \propto t^{-5/2}$, but this was corrected a year later by Phinney (1989) to the canonical $\dot{M} \propto t^{-5/3}$. By the chain rule the mass fallback rate may be expanded as

$$\frac{dM}{dt} = \frac{dM}{d\epsilon} \frac{d\epsilon}{dt},$$

where ϵ is the specific energy function. Once the star crosses the tidal radius the energy of the bound debris is frozen in and is given by the Keplerian potential

$$\epsilon = \frac{GM_h}{a}.$$

Kepler's third law gives

$$\begin{aligned} T &\propto a^{3/2} \\ \implies a &\propto T^{2/3} \\ \implies \epsilon &\propto T^{-2/3}. \end{aligned}$$

The rate of change of specific energy is thus

$$\frac{d\epsilon}{dt} \propto t^{-5/3}. \quad (2.4)$$

The rate of change of mass with respect to specific energy was assumed by Rees (1988) to be flat at late times; this assumption was later verified by Evans and Kochanek (1989) and Guillochon and Ramirez-Ruiz (2013) using hydrodynamical simulations.

The mass fallback rate is also expected to have a direct correspondence with the complete bolometric luminosity and should therefore also drop off with $t^{-5/3}$. The translation of this to band luminosity (particularly optical) is discussed in Section 2.4. Hydrodynamical simulations provide an estimate for $dM/d\epsilon$ across the duration of the disruption allowing one to describe t_{peak} as a function of M_h . This has the implication that if one can identify the location of peak luminosity and can make an estimate as to the type of star being disrupted then the black hole mass is accessible in principle (Guillochon and Ramirez-Ruiz 2013).

2.3.3 Accretion disk

Much work has been done in the past few years on the evolution of the bound material as it forms the accretion disk. Upon disruption, the bound material is largely believed to loop back around periodically, self-colliding, causing shocks which dissipate heat through the material. This leads to circularisation and a heated disk emitting approximately 10^5 K blackbody radiation (Strubbe and Quataert 2009). There is currently much debate about how this accretion disk evolves and there have been several recent attempts to model this evolution using simulations (e.g. Bonnerot, Rossi, Lodato and Price 2016; Piran et al. 2015; Shiokawa et al. 2015). General relativistic precession accounts for some discrepancies in accretion speeds (Shiokawa et al. 2015). This would indicate that black hole mass will affect the accretion rate; lower black hole masses may lead to much longer lived flares (Dai et al. 2015; Guillochon and Ramirez-Ruiz 2015)³.

Current models suggest that super-Eddington accretion may in tidal disruption of stars (Gezari 2014) which would infer the existence of jetted TDEs (Komossa 2015). Figure 2.7 shows how simple models expect accretion rates to cross the Eddington limit for low mass black holes.

³A long-lived flare Lin et al. (2017) was recently discovered in X-ray which may be linked to this theory.

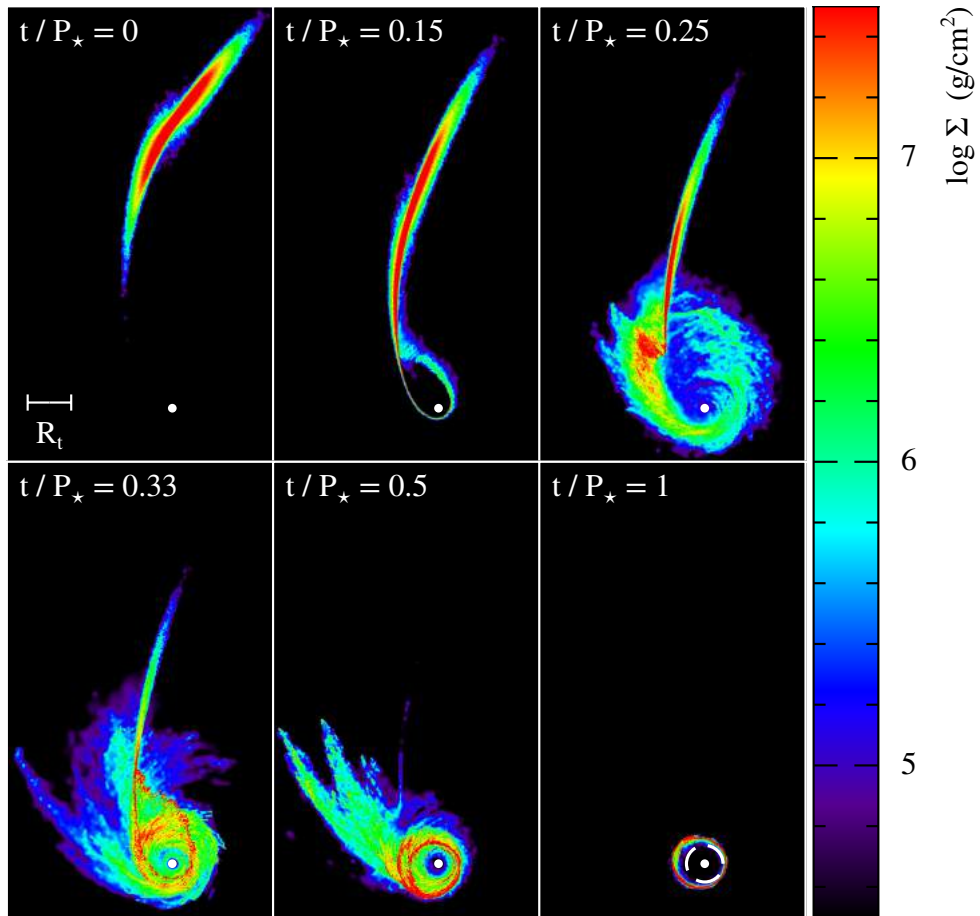


Figure 2.6: Snapshots of fallback from Bonnerot, Rossi and Lodato (2016) giving the fast initial fallback rate which has been observed. This particular model is for a highly elliptical (eccentricity of 0.95), highly penetrating ($\beta = 5$) stellar orbit in a relativistic potential with the resulting debris described by a locally isothermal equation of state. In this case the orbital period of the star, P_\star is 22 hours. Times are displayed as a ratio to this period and the gas is seen to fully circulate after one orbital period. The colour bar represents the gas column density, the white dot represents the black hole and the dashed line represents the theoretical circularisation radius.

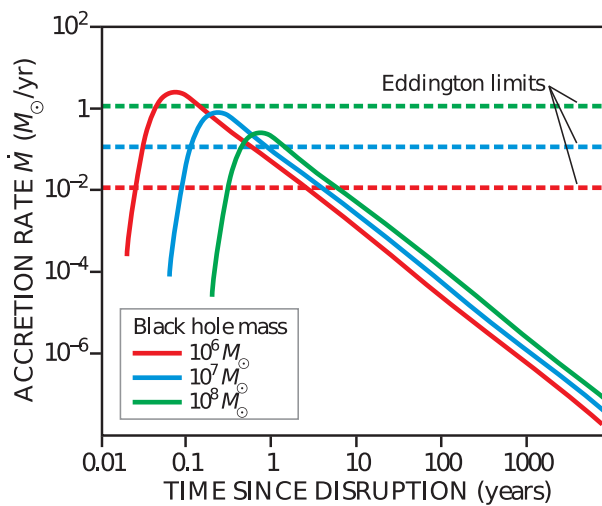


Figure 2.7: Simplified TDE accretion rates surpassing Eddington limit for lower mass black holes. These super-Eddington accretion rates can give rise to jets. Image from Gezari (2014).

2.3.4 Other features

Unbound debris

When a star gets tidally disrupted, half of the matter which is stripped from it gets accreted onto the black hole producing luminous flares but the other half gets ejected into the ISM. The unbound debris form very thin streams which vary largely in density and velocity. As the stream debris interacts with the ISM, the drag is such that they can quickly deposit large amounts of energy and can generate unbound debris remnants which can mimic supernova remnants (Guillochon, McCourt et al. 2016). This mechanism has been proposed as an alternative explanation for *Sgr A East* (Khokhlov and Melia 1996).

Jets

Due to the large accretion rates which are believed to surpass the Eddington limit in cases, similar to AGN, relativistic jets are also believed to occur in TDEs. This has sparked much interest as it provides the potential to witness the early evolution of jets in TDEs as they occur on human timescales, whereas AGN occur on cosmic timescales (Komossa 2015). The interaction of these jets with the ISM was also predicted to produce synchrotron emission in radio (Giannios and Metzger 2011). These jets, including radio emission, were observed in several candidate TDEs (Komossa 2015; Zauderer et al. 2011).

Unusual black holes

TDEs may occur around unusual black holes. Recoiling black holes are those which have been ejected from a galaxy nucleus through gravitational wave recoil. These black holes carry many stars with them, and though tidal disruption rates are expected to reduce in this case they are comparable to nuclear rates (Komossa and Merritt 2008). These events could account for off-nuclear TDEs (e.g. Wyrzykowski et al. 2017). Also possible is tidal disruption around binary black holes. These systems are such that stars are far more likely to be perturbed onto a loss cone orbit, and rates are boosted by 10^2 – 10^4 times (Ivanov et al. 2005). Tidal disruption by a binary black hole leads to unusual interruptions in the accretion stream (Liu et al. 2009) and there has already been a TDE around a binary black hole candidate (Liu et al. 2014; Saxton et al. 2012). As mentioned previously, tidal disruption of white dwarfs around IMBHs is also believed to be a strong avenue for their detection (Haas et al. 2012).

2.4 Observation of TDEs

The following section describes expected and past observations of TDEs. First discussed are the photometric and spectroscopic characteristics. A short section could also be added on astrometry; as these events generally occur around a SMBH, they should coincide with the nucleus of the galaxy. The nucleus of a galaxy has both the stellar density to perturb a star onto a loss

cone orbit to be tidally disrupted and the very high mass capable of very efficient accretion. It is possible for tidal disruption to occur outside the galactic nucleus; however, such events would be extremely rare or (relatively) unenergetic.

2.4.1 Photometry

As described previously, TDEs' mass fallback rate is generally expected to rise to a peak, followed by a decay. The rise is heavily dependent on the black hole mass and other system parameters, but the decay is believed to quite reliably tend to $t^{-5/3}$ (Komossa 2015). The assumption that this mass fallback rate translates to bolometric luminosity was confirmed at late times by Lodato et al. (2009). This however was assumed not to translate to observing band luminosities as the accretion disk cools and the spectral energy distribution shifts according to Wien's law (Strubbe and Quataert 2009). This was later confirmed analytically by Lodato and Rossi (2011). It was calculated that the luminosity in X-rays should approximately follow $t^{-5/3}$ for about a year before emission steepens exponentially.

It was also calculated that the optical luminosity should drop off a lot slower, at $t^{-5/12}$. Figure 2.8 compares these decays. However, as will be highlighted in Section 2.4.4, this is not what is observed. Optical light curves have been successfully fit by $t^{-5/3}$ decays (Gezari et al. 2012; van Velzen et al. 2011). This discrepancy may be accounted for by a lack of cooling in the accretion disk (Lodato 2012), or by the optical emission coming from reprocessing of emission by debris which is further out (Guillochon et al. 2014).

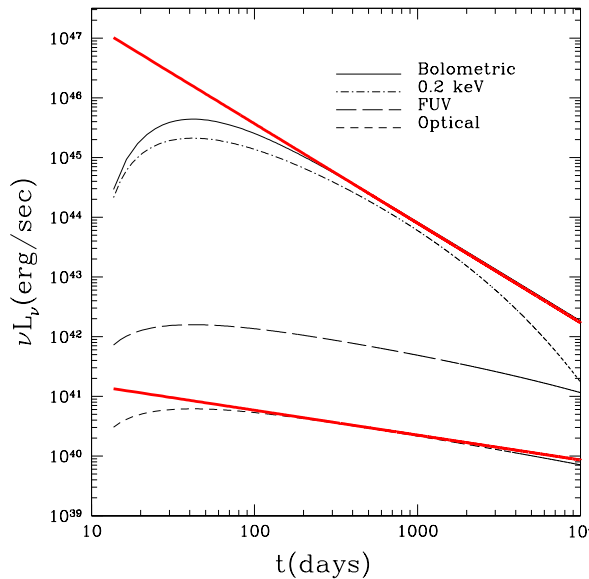


Figure 2.8: Predicted decays for bolometric, X-ray, ultraviolet and optical luminosities by Lodato and Rossi (2011). The red curves represent $t^{-5/3}$ and $t^{-5/12}$ respectively. The optical luminosity was predicted to follow this $t^{-5/12}$ decay but this has not been observed.

2.4.2 Spectroscopy

The spectral signature of a TDE should be broadly consistent with a blackbody spectrum (Kochanek 2016). This will lead to an optically blue spectrum. Similar to AGN, very broad emission lines are observed in the spectrum, potentially pointing to reprocessing. Strubbe and Quataert (2011) suggested this was due to photons from the accretion disk interacting with the unbound debris from disruption. However, the unbound debris streams are believed to be cylindrically self-gravitating and thus extremely thin, providing little reprocessing; instead the outer layers of the accretion disk are believed to be responsible for this reprocessing (Guillochon et al. 2014). Broad H and He features have been seen in several TDE candidates (Arcavi et al. 2014).

2.4.3 Potential imposters

In identifying TDEs, it is important to rule out other transient objects which may be mistaken for one. It is also important to consider that other common transients may falsely be identified as such and in reality may be a TDE (e.g Leloudas et al. 2016). Models of AGN and supernovae (SN) in particular share many physical similarities to those of TDEs, and the community's ability to discern these objects is especially important (e.g van Velzen et al. 2011).

AGN

AGN have been the subject of much interest and research in the past half century (Matthews and Sandage 1963) and are described in Section 2.2.2. Similar to TDEs, AGN are also widely believed to involve highly energetic accretion onto a central SMBH. Several aspects of the AGN model have also been ported into TDE models to account for observational features, and it is also believed to be possible for TDEs to occur around AGN (Karas and Šubr 2007).

The biggest similarity between TDEs and AGN is their nuclear location. They both involve accretion onto a galactic central SMBH so should both coincide with the centroid of a galaxy. Therefore astrometric measurements alone will not provide any sort of discrimination. The accretion disk reprocessing present in both objects leads to similar broad emission lines; however, while there is a narrow line region present in AGN, the accretion disk in a TDE is considered too dense for emission of the forbidden lines (Strubbe and Quataert 2011). AGN discrimination is necessary in detection of TDEs, and in some cases can involve detailed efforts (e.g. Holoi en et al. 2016; van Velzen et al. 2011).

Supernovae

As mentioned in Section 2.1.3, SNe occur at the end of a massive star's life or when a white dwarf accretes enough matter to reignite fusion. These events deposit vast amounts of energy into the ISM, similar to TDEs and AGN (Ostlie and Carroll 2007). They explode violently and then fade.

SNe are not constrained to the centre of a galaxy (but can still occur there), therefore precise astrometry can help to eliminate them. For example if a transient light curve is obtained which could point to a TDE or SN, astrometry may place the source outside of the galaxy centroid, pointing to a SN; SN rates also tend to be galaxy-wide therefore by constraining the source to the centre of the galaxy one effectively reduces the probability of it being a SN. The many types of SN also exhibit distinct light curves and/or spectra which are often used to eliminate their candidacy (see Komossa 2015).

2.4.4 Current observation status

Approximately 30 strong TDE candidates have been detected thus far (Komossa 2015). These are laid out by detection year and peak luminosity in Fig. 2.9. Detections can be seen across the full electromagnetic spectrum; radio components have been seen occurring from the jets of several TDEs (van Velzen et al. 2015; Zauderer et al. 2011). As can be seen in the figure, in the last number of years detection there have been many TDEs by optical surveys.

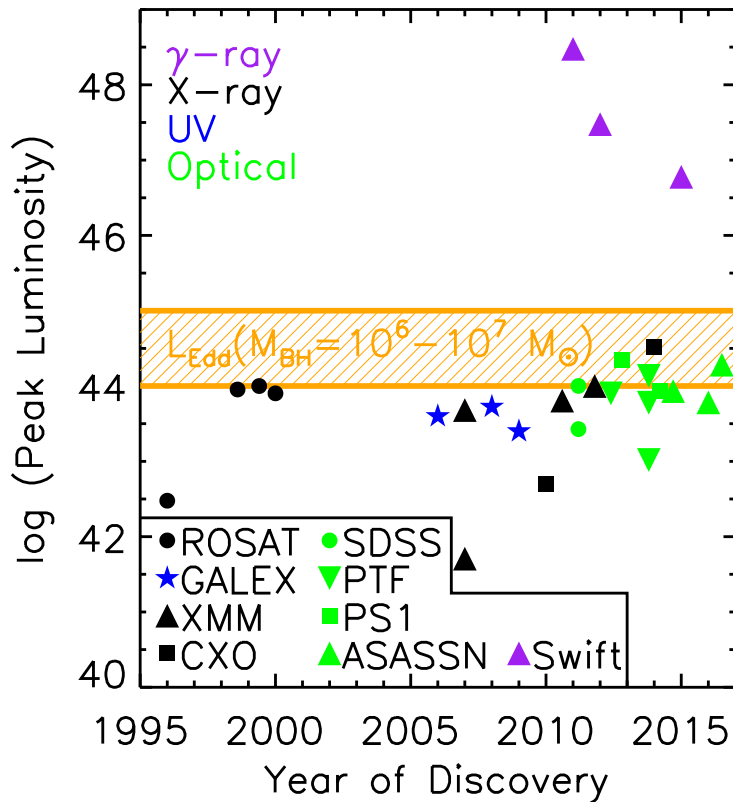


Figure 2.9: Strong TDE candidate detections since 1995 showing peak luminosity and marked by discovery observatory. These have been seen across a broad spectrum, though particularly in optical for the last five years. Also shown is the Eddington limit region for 10^6 – 10^7 solar mass black holes, which several TDEs have been seen to cross. Image from Gezari (2016).

The first TDE candidates were detected by the ROSAT mission (Trümper 1982), which detected soft X-ray outbursts from galaxies which had not shown any previous signs of AGN activity. These events showed promise of being TDEs which inspired searches in ultraviolet (Gezari et al. 2008) and then more recently in optical (e.g. van Velzen et al. 2011). Evidence for jetted TDEs

was also found in Swift (e.g. Zauderer et al. 2011). *The Open TDE Catalog*⁴ is a maintained list of possible TDE candidates. It endeavours to list all possible TDE candidates, including those which have favoured as other objects, and contains 62 entries as of February 2017, many of which have photometric and spectral data available.

One notable TDE candidate is PS1-10jh (Gezari et al. 2012). The light curve of PS1-10jh is shown in Fig. 2.10, along with the theoretical $t^{-5/3}$ fits to the data. The theory can be seen to fit the data very well. The peak luminosity is very well localised which allowed an estimate for the black hole mass to be made (Gezari et al. 2015). Spectroscopic follow up of this candidate was carried out where broad helium lines were observed, fitting with theory. No hydrogen lines were observed leading to the initial assumption that this was a helium rich star, however these are very rare. Other models allow for it to be a main sequence star where the hydrogen gets highly ionised and falls below the continuum (Gezari et al. 2015).

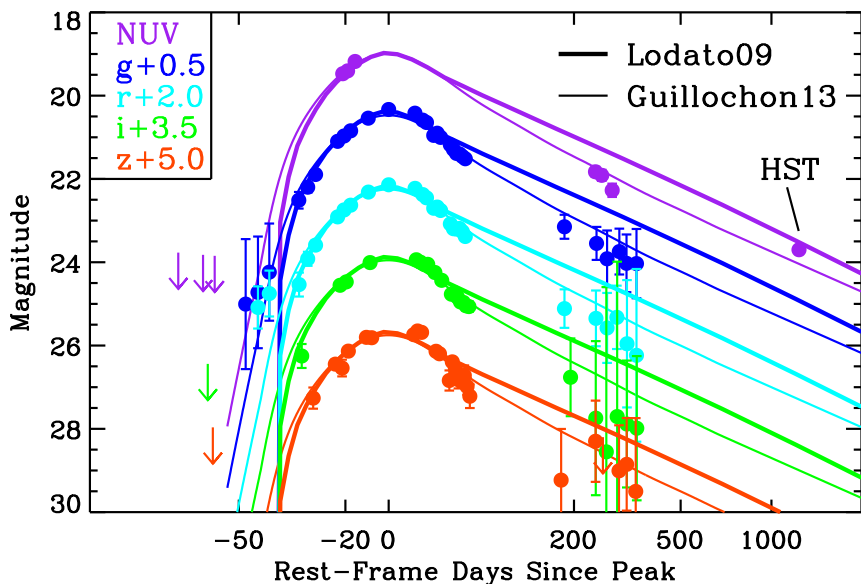


Figure 2.10: Light curve of PS1-10jh with $t^{-5/3}$ fits to data using two models. This light curve is very notable due to its high sampling in various bands, particularly around the peak. Image from Gezari et al. (2015).

2.5 TDE rates

2.5.1 Theoretical vs measured rate

Having defined the sphere of influence for a black hole in Eq. (2.2), the rate of tidal disruption around that black hole will be given by

$$\dot{N} = \frac{N(r_h)}{t_{\text{relax}}(r_h)},$$

⁴<http://tde.space>

where $N(r_h)$ is the number of stars within the sphere of influence, and $t_{\text{relax}}(r_h)$ is the relaxation time of the system, i.e. the time for it to decay into a state of equilibrium. The relaxation time comes from the analytic relaxation model chosen; *two-body relaxation* is favoured by Stone and Metzger (2015) as the most robust and ubiquitous model, though others may also contribute such as *resonant relaxation* (Hopman and Alexander 2006). $N(r_h)$ was estimated by Wang and Merritt (2004) using measured galaxy data. Alexander (2012) provides a summary of methods used to calculate the TDE rate; estimates generally put this value between 10^{-4} and 10^{-6} per year per galaxy. Stone and Metzger (2015) “conservatively” estimate a few $\times 10^{-4} \text{ yr}^{-1} \text{ galaxy}^{-1}$.

These theoretical predictions, however, differ from measured values by roughly an order of magnitude. Van Velzen and Farrar (2014) measured the rate of tidal disruption by searching Sloan Digital Sky Survey (SDSS) galaxy observations for flares fitting TDE models. As the search sample was very large and this search was systematic, this was a good sample to estimate the rate of observed TDEs. Combining the two detected SDSS TDE light curves with two other better sampled light curves a rate estimate of $\sim 2 \times 10^{-5} \text{ yr}^{-1} \text{ galaxy}^{-1}$ is attained. This discrepancy in rates could be due to selection bias in the observations (Stone and Metzger 2015). Much is still speculative, however, so this discrepancy could perhaps be accounted for by a subtle discrepancy in TDE models. More data are needed to further constrain these rates.

2.5.2 Galaxy bias

TDEs appear to be biased towards quiescent galaxies with strong Balmer absorption, known as E+A galaxies. French et al. (2016) classified the host galaxies of eight TDE candidates and found that this class of galaxy was extremely overrepresented in the sample. The strongest 0.2% of Balmer absorption galaxies within the SDSS sample hosted three of the eight TDEs investigated, and the strongest 2.3% hosted six of the eight TDEs. This can be seen in Fig. 2.11, where the TDE galaxies are clumped in a region which is outside the common SDSS group. These galaxies fall into a class where many have had recent mergers, increasing the possibility of black hole binaries or perturbed stellar orbits (French et al. 2016).

These galaxies show rates enhanced by ~ 190 and 33 times respectively. Adjusting previously calculated rates (Stone and Metzger 2015) gives approximately $2 \times 10^{-3} \text{ yr}^{-1} \text{ galaxy}^{-1}$ and $3 \times 10^{-4} \text{ yr}^{-1} \text{ galaxy}^{-1}$ for these galaxy types respectively. This would give an adjusted rate of $2.5 \times 10^{-6} \text{ yr}^{-1} \text{ galaxy}^{-1}$ for normal star-forming and early-type galaxies (French et al. 2016). Perhaps a bias such as this to galaxies where tidal disruption is obscured may account for discrepancies in theoretical and measured TDE rates.

2.6 TDEs and Gaia

It is argued here that Gaia is suited for detection of TDEs. As Gaia is described in the following chapter it will be seen that extragalactic and transient observation are among the low-priority

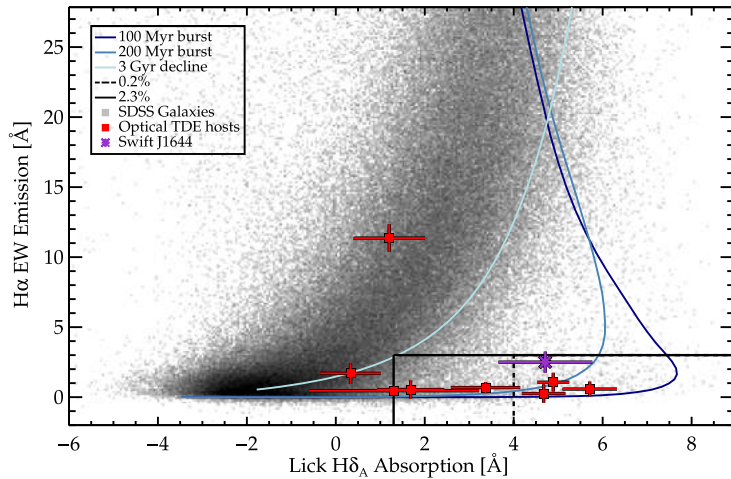


Figure 2.11: TDE host galaxies overlaid on SDSS galaxies plotted by $H\alpha$ EW emission vs $H\delta_A$ absorption. The curves represent star forming history tracks. The TDEs can be seen to largely occur in a small region of the plot, i.e. low $H\alpha$, moderate to high $H\delta_A$, where there are fewer SDSS galaxies suggesting that this area is over-represented in TDEs. The $H\delta_A$ index measures Balmer absorption but is optimised for absorption from A stars. Image from French et al. (2016).

science goals of the mission; however, many aspects of Gaia which have been optimised primarily for characterising a fraction of the stars in the Milky Way are also useful for TDE detection. Blagorodnova et al. (2015) predict that Gaia will detect 20–30 TDEs per year.

Gaia is a very precise astrometry mission so its ability to resolve sources and galaxy nuclei make it suitable for TDE detection, since this is usually the first filter when looking for TDEs (unless one is looking for TDEs around recoiling black holes). Over its five year lifetime Gaia will observe each part of the sky an average of approximately 70 times, giving it an average cadence of approximately 26 days. This makes it suitable for observation of the $t^{-5/3}$ decay which occurs over months. Figure 2.12 shows a comparison of transient characteristic decay timescales for reference. Although transients will not appear in the Gaia archive until years after it is decommissioned, there is an initiative which releases transients as they are detected so that follow-up measurements may be obtained (see Section 3.7.1).

Summary

SMBH and accretion physics are very interesting but are very difficult to probe due to their occurrence at large distances and, in the case of black holes, the fact that they have a weak electromagnetic signal. TDEs provide a unique laboratory for these phenomena. TDEs occur when a star in the nucleus of a galaxy is perturbed onto a loss cone orbit and passes within the tidal radius of a supermassive black hole. If the tidal radius is inside the event horizon of the black then the star will be swallowed whole and nothing will be observed. Depending on the structure of the star and how much it penetrates the tidal radius, it may be partially or completely disrupted. Half of the disrupted matter is bound to the black hole and is eventually accreted onto it, and half of the matter is ejected in an unbound orbit where it may interact with

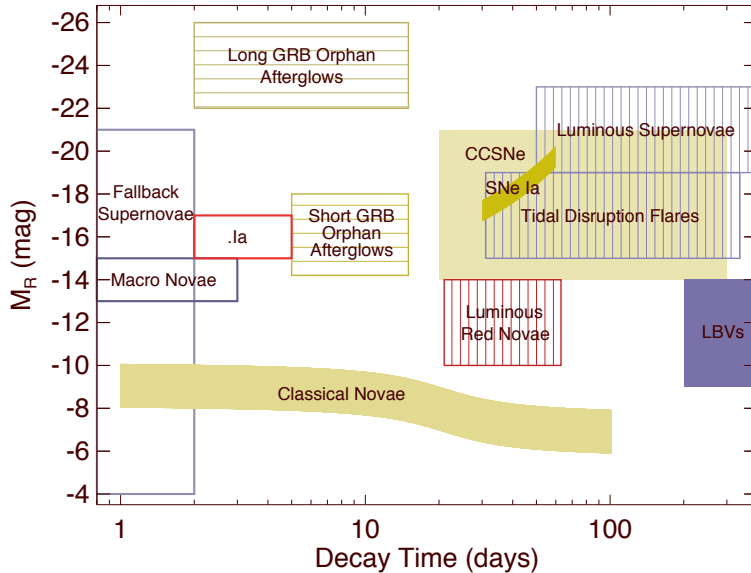


Figure 2.12: R band peak absolute magnitude as a function of characteristic decay timescale for various transients, including TDEs. TDEs are seen to decay on a timescale of 20–200 days indicating that they will largely be suitable for detection with Gaia. Image from Rau et al. (2009).

the ISM. This bound matter forms an accretion disk with matter falling back onto the black hole at a rate which tends to $t^{-5/3}$, which should correspond to the event bolometric luminosity at late times. Several of these events have been observed across the electromagnetic spectrum including candidates with jets and a candidate around a binary black hole. As will be explored in this thesis Gaia should be suitable for detection of these transients.

Chapter 3

Gaia

3.1 Overview

Gaia (Lindegren and Perryman 1997) is an ESA astronomical observatory that was launched in 2013 and is currently orbiting the second Lagrange point gathering data. The primary aim of the mission is to measure precise distances to approximately one billion stars in the Milky Way, making a three dimensional map of the galaxy. The observatory was launched into a Lissajous orbit around the second Lagrange point of the Earth-Sun system from a Soyuz-Fregat launch vehicle. Gaia is considered to be the successor to the Hipparcos mission (Perryman 1997) and is providing unprecedented astrometric measurements of the galaxy, both in quantity and precision (Lindegren and Perryman 1997). The payload has no moving parts and consists of two telescopes which focus light onto a common plane. This focal plane contains a CCD array with approximately one billion pixels. An astrometric, photometric and spectroscopic instrument are also located on the focal plane and provide a rich array of data. Due to the sophistication of its instruments, Gaia's data products will be vast. These data products will be released into an archive in stages over the course of several years. The mission has a nominal length of five years (2013–2018). The first data release was in September 2016 and the final release is currently scheduled for 2023. An artist's impression of Gaia in space is shown in Fig. 3.1.

3.2 Motivation

3.2.1 Hipparcos

Hipparcos (shown in Fig. 3.2) was the predecessor to Gaia, launched in August 1989 by ESA (Perryman 1997). Its name is an acronym for 'High Precision Parallax Collecting Satellite' while also being an acknowledgement to the ancient Greek astronomer, Hipparchus. Hipparcos was operational until 1993, and in 1997 the data were compiled into the Hipparcos and Tycho catalogues. The Hipparcos catalogue consisted of the positions, proper motions and trigonometric parallaxes of approximately 120 000 stars. This facilitated measurement of the distance to 20 000

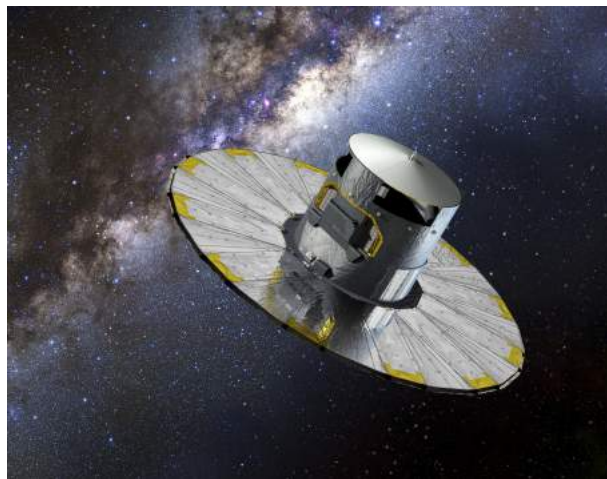


Figure 3.1: Artist's representation of Gaia. Image from ESA.

stars with a precision of less than 10% and 50 000 with a precision of less than 20% (Perryman et al. 1997).

The operation of Hipparcos was very similar to Gaia. Like Gaia, Hipparcos consisted of two apertures constantly gathering data as the satellite rotated. Unlike Gaia, Hipparcos operated from a geostationary orbit and rotated along its horizontal axis every two hours and eight minutes. Each of the fields of view subtended an area of $0.9^\circ \times 0.9^\circ$, and they were separated by an angle of 58° . Each aperture focused light through a Schmidt telescope onto a focal plane with a grid of 2688 parallel slits in an area of $2.5 \times 2.5 \text{ cm}^2$ in front of an image dissector tube (Perryman 2008).

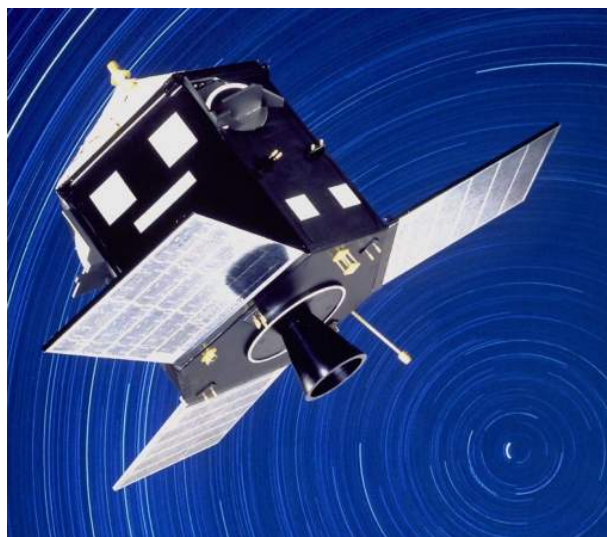


Figure 3.2: Artist's representation of Hipparcos. Image from ESA.

The main differences between Gaia and Hipparcos lie in the focal planes of the telescopes. This is primarily a result of twenty years of technological development. Gaia's focal plane contains a large array of modern CCDs and uses two star mapper strips to identify objects before they reach the astrometric field so that only privileged CCD rows are read out (described in Section 3.3.2). Hipparcos's focal plane contained two sky mappers as is in Gaia, however one

was placed before the focal plane and one after due to their shape. This did not affect operation as these data were used to identify the aperture from which an object originated *a posteriori* (see Fig. 3.3) (O’Flaherty 1997). During analysis, when a source was identified in the main grid, it was looked for in each of the starmappers; this allowed the aperture and thus position (given the time of the observation) to be inferred. Hipparcos also was provided a catalogue of objects to observe instead of finding its own sources (Prusti et al. 2016).

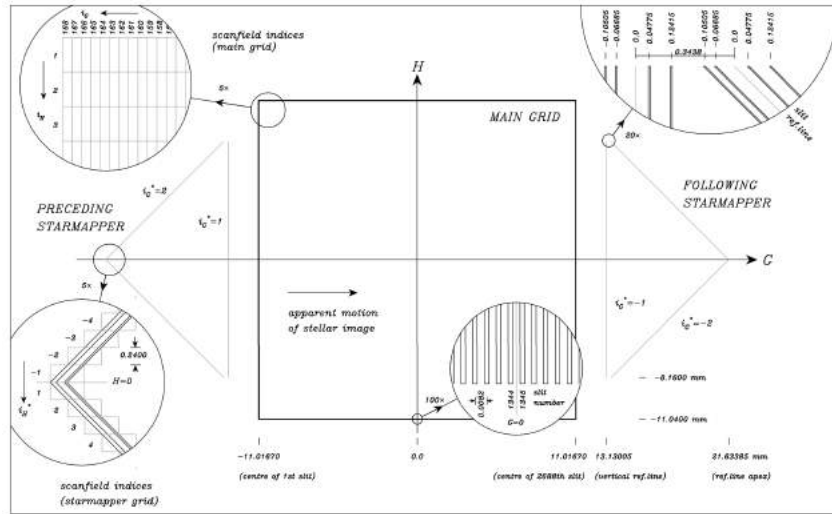


Figure 3.3: Focal plane of Hipparcos. In contrast to Gaia where only privileged data are read out, all data were read out in Hipparcos so the starmappers’ only function was to determine from which aperture a source came *a posteriori*, thus they could be placed either side of the main grid on the focal plane. Image from van Leeuwen (2007).

At the time, Hipparcos was an extremely difficult mission to undertake. It was first proposed in the 1980s (Perryman 2010), and was the first optical space astronomy mission launched (a year before NASA/ESA’s Hubble Space Telescope). Hipparcos still created the most accurate pre-Gaia map of the Milky Way contained in its main and Tycho catalogues (made from the star mapper data). It also served as a proof of concept, inspiring many mission proposals which would utilise the Hipparcos methodology and subsequent advances in technology to make a more precise map (Perryman 2011), principally Gaia. The astrometric techniques which were proven in Hipparcos and employed in Gaia are described in Section 3.5

3.2.2 Gaia

The name *Gaia* was originally chosen to be an acronym for ‘Global Astrometric Interferometer for Astrophysics’ (Lindegren and Perryman 1997) as it was proposed to utilise interferometry for its purpose. This technique was later dropped in favour of photometry, identical to Hipparcos.

Gaia improved on Hipparcos in almost every way while the main operating principle remains the same. Gaia has a larger collecting area which allows it to collect significantly more light (two entrance pupils of $1.45 \times 0.5 \text{ m}^2$ (Gieleson et al. 2013) compared to Hipparcos’s entrance pupil

of 0.29 m diameter (O’Flaherty 1997). Since Hipparcos used photomultiplier tubes (PMTs), it could only track one object at a time, whereas Gaia utilises advanced CCDs. It is able to measure a star’s position and proper motion 200 times more accurately.

Gaia also provides low-resolution spectroscopy in the blue and red photometers and high-resolution spectroscopy in the radial-velocity spectrometer. However, these instrument improvements and addition of instruments create significantly more data. This excessively large volume of data is mitigated on-board whereby only pixels containing useful science data are read out and downlinked to Earth. These measures significantly reduce the amount of data produced by Gaia; however, there will still be an unprecedented amount of data created which presents a huge challenge to data scientists within ESA.

3.3 Spacecraft

3.3.1 Launch and operations

Launch

Gaia was launched on Thursday, December 19, 2013 from Kourou, French Guiana. It was launched by Arianespace on a Soyuz-ST-B launcher. The Fregat was lifted off the Earth via three stages which fell back to the sea, and was then separated from the mission payload and put into a graveyard orbit. A total of 2105 kg was launched, 2034 kg of which composed the launch stages. Gaia was injected from a low-Earth parking orbit into an L2 transfer orbit (Arianespace 2013). After separation from the launch adapter, the Deployable Sunshield Assembly (DPA) (discussed in Section 3.3.3) was successfully deployed.

After a sequence of orbital manoeuvres Gaia was placed in a Lissajous type orbit around the second Lagrange point (L2), about 1.5 million kilometres from Earth (Milligan 2016). This orbit is quite far from Earth and is thus more difficult and expensive to reach, compared to Hipparcos’s geostationary orbit for example, but there are many advantages to placing Gaia in orbit around L2. Since L2 is along the Earth-Sun line and rotates with the Earth, the location of the Earth and the Sun with respect to Gaia is extremely consistent and relatively simple to avoid. The Earth also occupies a smaller solid angle since it is much farther from Gaia’s field¹. Gaia also avoids negative (and positive) effects from proximity of the Earth such as the Van Allen radiation belts². Gaia rotates around the shadow of Earth to avoid any major temperature fluctuations (as shown in Fig. 3.4).

¹A simple back-of-the-envelope calculation shows that the Earth will be over 1200 times smaller to an observer at L2 than one in a geostationary orbit

²However being outside the Earth’s magnetosphere means that it is exposed to other forms of radiation such as cosmic rays (Crowley et al. 2016).

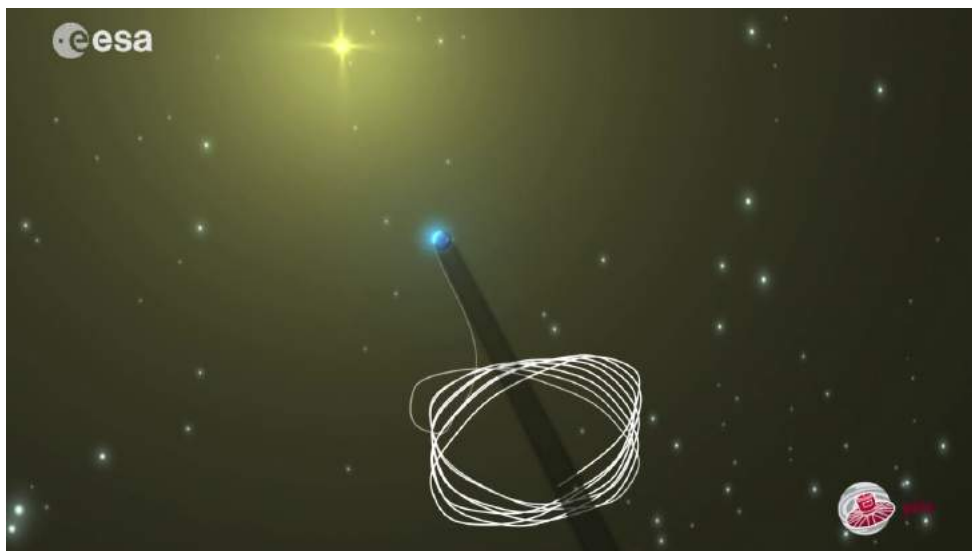


Figure 3.4: Gaia's Lissajous orbit around L2. This orbit was chosen to keep Gaia out of the Earth's shadow and thus to avoid larger thermal fluctuations. Image from ESA.

Operations

The Missions Operations Centre (MOC) is located at the European Science Operations Centre (ESOC) in Darmstadt, Germany. From here, any required mission planning is done and the spacecraft is monitored and controlled. Data downlinked from the spacecraft to the ground stations are also sent here to be relayed to the Scientific Operations Centre (SOC). The SOC is located at the European Science Astronomy Centre (ESAC) near Madrid, Spain and coordinates the scientific aspects of the mission through a consortium of coordination units responsible for various aspects of data handling and analysis, i.e. the Data Processing and Analysis Consortium (DPAC) (Rudolph et al. 2014).

Due to the quality of the data being collected by Gaia on a daily basis, it downlinks to three ground stations, located at Cebreros in Spain, New Norcia in Australia and Malargüe in Argentina. The spread in these ground stations gives Gaia a visibility of up to 24 hours (12.5 hours on average). The data are downlinked in *X-band* with speeds around 7.6 Mbps (Rudolph et al. 2014). Gaia's DPAC (described in Mignard et al. 2007) was set up in 2006 and is a consortium made up of groups from various institutions around the world. It is responsible for processing and releasing Gaia data, including the final Gaia catalogue.

Scanning law

Gaia will be operational for five years (with the possibility of being extended to six), observing constantly for that time; for this reason it is necessary to optimise its *scanning law* to best achieve the desired scientific goals. Gaia will obtain parallaxes (among other measurements) of the brightest one billion stars in the sky. In order to achieve this it has two fields of view separated by approximately 90° (known as the basic angle) sweeping great circles across the sky, while precessing around another axis. This is called the scanning law and has been motivated mathematically (see Lindegren et al. 2012), and was demonstrated on Hipparcos (Perryman

et al. 1997).

The parameters that Gaia uses to achieve its performance goals comprise Gaia’s nominal scanning law (NSL) (Fig. 3.5). The angle (ξ) between the satellite spin axis and the Sun is kept constant at 45° ; this achieves good parallax sensitivity as the along-scan (AL) parallax displacement is proportional to $\sin \xi$ (discussed further in Section 3.5 and Lindegren et al. 2012). If the Sun is fixed at $\theta = 0^\circ$ (polar angle), $\phi = 0^\circ$ (azimuthal angle) this maps out a small circle at $\phi = 45^\circ$, i.e. the precession axis. The satellite rotates around its spin axis mapping out great circles. This is represented in Fig. 3.5a. Gaia spins on its axis once every six hours and precesses once every 63 days. Its fields of view will move as it orbits the Sun, allowing it to get a complete view of the sky. By the end of its lifetime Gaia will have observed each object an average of approximately 70 times and have a sky coverage shown in Fig. 3.5b.

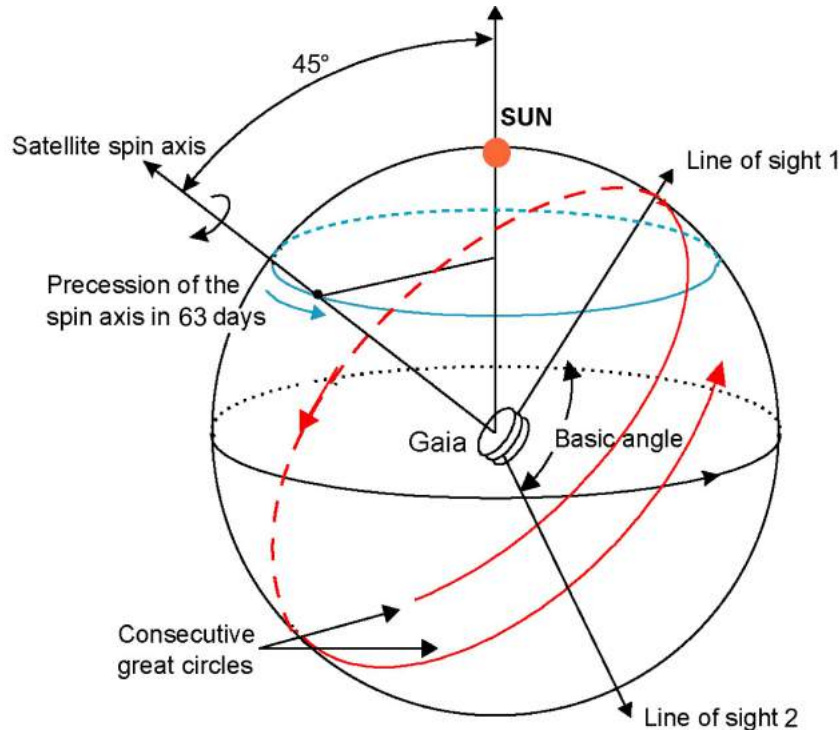
Issues encountered after launch

Upon reaching L2 the payload was passively cooled to working temperature and final checks were done as the system was brought to full working capacity (Rudolph et al. 2014). In L2, Gaia was put into micropulsion control mode; it was quickly realised that one of the microthrusters was showing a significantly increased calibration offset, however the attitude and orbit control loop was still successfully controlling the attitude. An on-ground investigation was conducted and it was concluded that this was related to a fault in the circuitry measuring the fluid flow. Some minor adjustments were made without a software patch to account for this. Later in the mission it was discovered that these flow values were drifting over time requiring more frequent calibration (time which could not be used for science), however this was corrected with a new flow measurement method (Milligan et al. 2016).

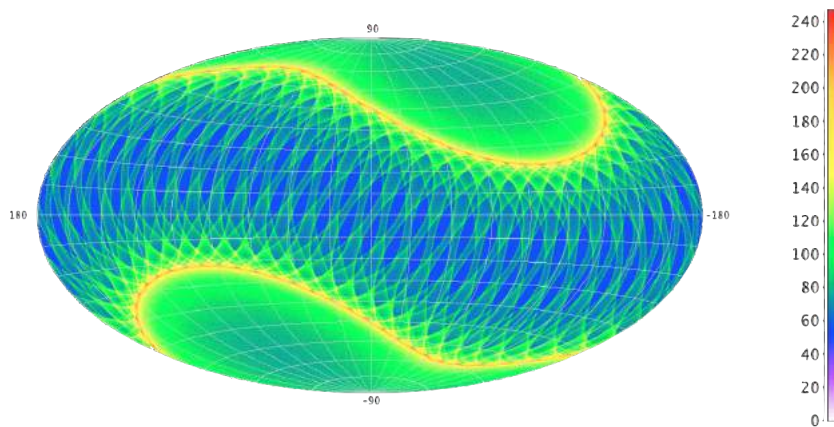
One of the redundancy thrusters was also lost during launch. Airbus Defense and Space (Airbus DS) performed a feasibility study and concluded that two of the thrusters which had been fitted to bring Gaia to L2 had sufficient residual torque to be used in place of the defunct redundancy thruster. New redundancy software was developed utilising these two thrusters instead of the defunct one and uploaded, restoring full redundancy.

On first operation of the telescope, it was noticed that the laser light from the basic angle monitor (BAM) (described in Section 3.3.2) and star light were diminishing. This was found to be due to water ice sublimating on the telescope optics. This affected imaging by reducing the light from a star hitting the focal plane, and distorting the point spread function (PSF). The ground teams constrained the problem to particular mirrors and activated decontamination heaters to successfully clear the problem. During this decontamination phase thermal fluctuations affect the ultra-sensitive setup; therefore during this period and a subsequent cool down period, mission science is impacted (Milligan et al. 2016). The ice periodically resublimates and the decontamination is thus performed periodically (four times so far). This effect is lessened over time, possibly due to the water vapour escaping or it sublimating somewhere which does not affect Gaia’s performance (shown in Fig. 3.6).

Perhaps the most significant issue discovered after Gaia’s launch was an abundance of stray-



(a) Geometry of Gaia in spherical polar coordinates where the Sun is fixed at a polar and azimuth angle of 0. The red circles represent Gaia's rotation every six hours. Gaia also precesses around the sun every 63 days. All this occurs as Gaia orbits L2, while L2 orbits the Sun. Image from ESA.



(b) Sky coverage of Gaia's nominal scanning law in equatorial coordinates. Colour is representative of the number of times Gaia observes a patch of sky. Video of scanning law trace may be found at <https://youtu.be/lRhe2grA9wE>.

Figure 3.5: Gaia's nominal scanning law.

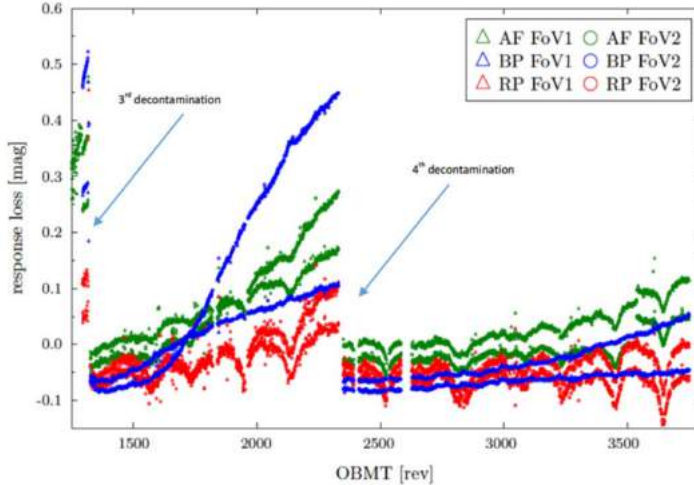


Figure 3.6: Gaia’s response loss due to water ice sublimation on the telescope optics vs on-board time management (OBTM) time in revolutions from September 2014 to May 2016. Decontaminations are periodically performed to remove the ice. The effect is seen to diminish over time. Image from Milligan et al. (2016).

light varying with spacecraft rotation. This straylight was some two orders of magnitude brighter than expected and provided a larger background level. This straylight was traced to scattered sunlight (Mora et al. 2016). The sunshield blocks much of the light from the telescopes, however the shield contains a blanket made up of Nomex fibres (Prusti et al. 2016). Bundles of these fibres were left to protrude from the edge of the sunshield (Fig. 3.7) as they were deemed too risky to cut in the clean room. These fibres cause unwanted sunlight to scatter into the apertures. As a result of this straylight there is extra noise associated with the object data, which particularly affects faint sources. This effect is very difficult to mitigate, however a software update was applied to better account for this increased noise level in the Astrometric Field (AF), and an augmented Radial Velocity Spectrometer (RVS) windowing system was applied (Milligan et al. 2016).

3.3.2 Payload module

Gaia’s payload module was built by EADS Astrium (now Airbus DS. The payload module is primarily situated around a hexagonal Silicon-Carbide (SiC) optical bench, on which two telescopes are mounted. This bench is approximately 3 m in diameter and made of 17 segments brazed together (Prusti et al. 2016). Most structural components in the spacecraft are made of SiC. This material is very strong and stable while being relatively light (De Bruijne et al. 2010).

Optics

Gaia consists of two telescopes which focus light from objects onto a common focal plane on which the three scientific instruments are located (described in Section 3.4). Each telescope



Figure 3.7: A flight spare sunshield blanket showing the bundle of fibres protruding from edge. These fibres cause unwanted light to scatter into the apertures. Image from ESA.

consists of three focusing mirrors (M_1 – M_3 and M'_1 – M'_3) and two flat folding mirrors (M_5 and M_6); M_4 and M'_4 make up a beam combiner. Each telescope has a $1.45\text{ m} \times 0.5\text{ m}$ aperture and a 35 m focal length (hence the folding mirrors). They point in two directions, separated by the *basic angle*, which is 106.5° (discussed further in this section and Section 3.5.2). The light path for the two lines of sight is shown in Fig. 3.8.

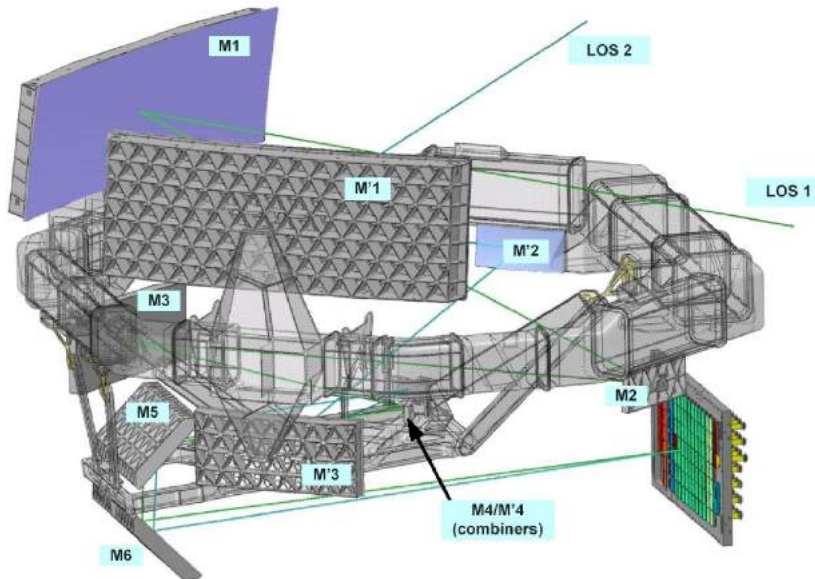


Figure 3.8: Light path from two lines of sight in Gaia. Image from Charvet (2006).

Each mirror is silver-coated to ensure that little light is lost to inefficiencies. Small chromatic aberrations exist in the mirrors which would normally be ignored but due to the accuracy that Gaia is designed to achieve these must be calibrated out of the data. These aberrations cause small yet significant (for Gaia) displacements in the focused image. The aberrations' effect is proportional to the wavelength of the incoming light so these displacements may be calibrated

out of the system. There are some diffracting optics in front of the Blue Photometer (BP) and Red Photometer (RP) and the RVS which are discussed in Section 3.4.3.

Focal plane

Gaia's optics focus each telescope's field of view onto a common focal plane which is shown schematically in Fig. 3.9. The focal plane contains 106 back-illuminated full-frame CCDs arranged in seven across-scan (AC) rows and 17 AL columns (strips) (Prusti et al. 2016). These CCDs were constructed by e2v technologies especially for Gaia (Crowley et al. 2016). Each CCD operates in a *time-delay integration (TDI)* mode whereby the satellite rotation rate and the CCD readout rate are synchronised. Each CCD is made of 4500×1900 pixels giving Gaia a total of 938 million pixels. The pixels are rectangular and are physically $10\text{ }\mu\text{m} \times 30\text{ }\mu\text{m}$, which corresponds to $59\text{ mas} \times 177\text{ mas}$ in the field. These rectangular pixels imply that detection of asymmetric features in sources will depend on their position angle as they cross the focal plane.

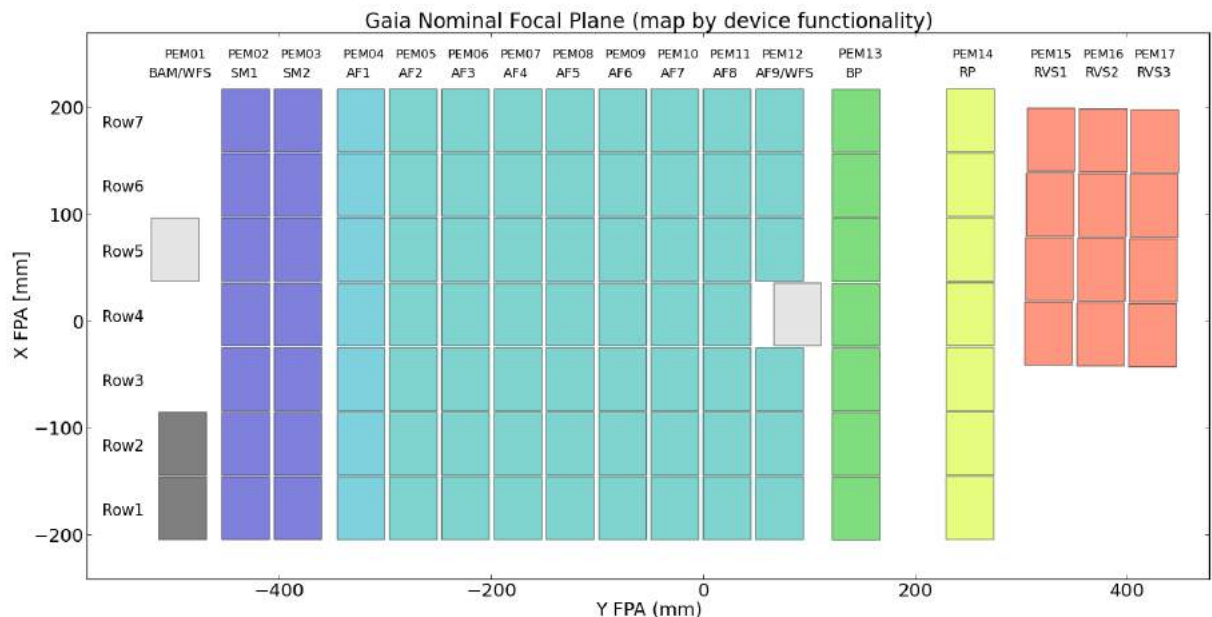


Figure 3.9: Gaia focal plane showing 106 CCDs in 17 strips and 7 rows. These make up the three scientific instruments, the sky mapper and the metrological instruments. Image from Crowley et al. (2016).

An object takes 0.9828 ms to cross a pixel and thus ~ 4.42 s to cross a CCD (Crowley et al. 2016). There are three variants of CCD used in Gaia, whose quantum efficiencies are optimised for the appropriate wavelength band: The broadband CCD optimised for the whole G band and used in the AF, the Sky Mapper (SM) and the wave-front sensor (WFS); the blue-optimised CCD used in the BP; and the red-optimised CCD used in the RP, the RVS and the BAM (Crowley et al. 2016). Gaia does not have a shutter or a lamp and thus cannot perform biasing or flat-fielding; however, in using the Astrometric Global Iterative Solution (AGIS) (discussed further in Section 3.5 or Lindegren et al. 2012) calibration is done using real data. The CCDs are passively cooled to 163 K to reduce dark currents. The focal plane sits with a cold radiator box

and each CCD has its own proximity electronics module where heat is dissipated to cold space (Prusti et al. 2016).

As Gaia rotates, object images move in the AL direction on the focal plane (from left to right in Fig. 3.9). They first strike the SM CCD row which corresponds to the aperture through which they passed. Baffles are used to ensure that light striking each SM is coming from the corresponding field of view. The SM is thus used to identify which field each image is coming from. It also determines whether an object is bright enough (i.e. above 20.7 mag) to be of interest.

If the image is deemed to be of interest it is tracked along the AF and read out from each CCD. After the image has passed through the last AF CCD column, it is sent through a prism which disperses the light from blue to green onto the BP, and then a prism which disperses the light from red to green onto the RP (discussed further in Section 3.4.3). If the image is brighter than 16 mag it is dispersed across RVS where a high resolution spectrum is taken around the calcium triplet (discussed further in Section 3.4.4). Also located on the focal plane are four CCDs used for metrology; two WFSs and two BAMs which are discussed further in Section 3.3.2.

Data handling

If all CCDs were continuously being read out, the amount of data generated would be unmanageable both by the spacecraft and DPAC; thus measures have been taken on board the spacecraft to reduce the amount of data being generated. Not all pixel data are read out; as mentioned previously, a window is drawn around an object of interest, whose size and binning are defined by the detected brightness of the object, and this window alone gets read out and saved to memory. Data are also binned and compressed without loss of scientific information (Prusti et al. 2016). The read windows are defined by the corresponding CCD video processing unit (VPU).

The payload data handling system (PDHS) consists of seven VPUs which operate in parallel; one for each CCD row on the focal plane. These VPUs are fed input from the SMs and spacecraft sensors and do some real-time analysis in the form of *video processing algorithmss* (VPAs) to determine if an object is of interest and draw object read windows (Charvet 2006). The VPUs generate several formats of data including *star packets* which are usually the raw CCD output, and *auxiliary science data* which provide information such as logs to ease analysis done on-ground. Gaia carries onboard a Rubidium atomic clock which keeps the time very precisely as it is important to know the precise time of each observation to perform high-precision astrometry. VPU data are then fed into the onboard ~ 120 GB solid state drive where they wait to be downlinked to a ground station. The data are then downlinked at a rate of ~ 8.7 Mb/s (40 GB/d) to one of the ground stations (Prusti et al. 2016).

Metrology

Gaia contains two primary metrological systems; these are the BAM and the WFS. The basic angle is the angle separating the two telescopes on Gaia, fixed at 106.5° (Hipparcos used 58°). It is imperative that this angle is kept constant for the duration of the mission. In order to perform accurate astrometry Gaia needs to measure absolute parallax rather than differential parallax which is typically what is measured (discussed in Lindegren and Bastian 2011 and Section 3.5.1). This is primarily why two fields of view are used.

In order to maintain the accuracy of Gaia's astrometry, this basic angle must be kept constant during the course of Gaia's lifetime. The BAM measures this basic angle and makes adjustments to the mirrors to maintain the desired angle. The BAM consists of two Fizeau interferometers (see Loreggia et al. 2004) which each form an interference pattern on a CCD. There is an extra BAM CCD for redundancy as maintaining (or at least knowing) this angle is mission critical (Gieleson et al. 2013). The relative positions of the fringes in the interference patterns indicate any shifts in the basic angle. The light originates from a laser diode mounted on a bar opposite the M1 mirror. This light is split into two pairs of beams directed at M1 and M1' (via a bar opposite M1'). These bars are mounted onto the SiC optical bench and are extremely solid; they are shown in Fig. 3.10. The beams hit an allocated area on the mirrors and make their way to the BAM CCD, interfering along the way. The basic angle is measured with an accuracy of $0.5 \mu\text{as}$ every five minutes (Gieleson et al. 2013).

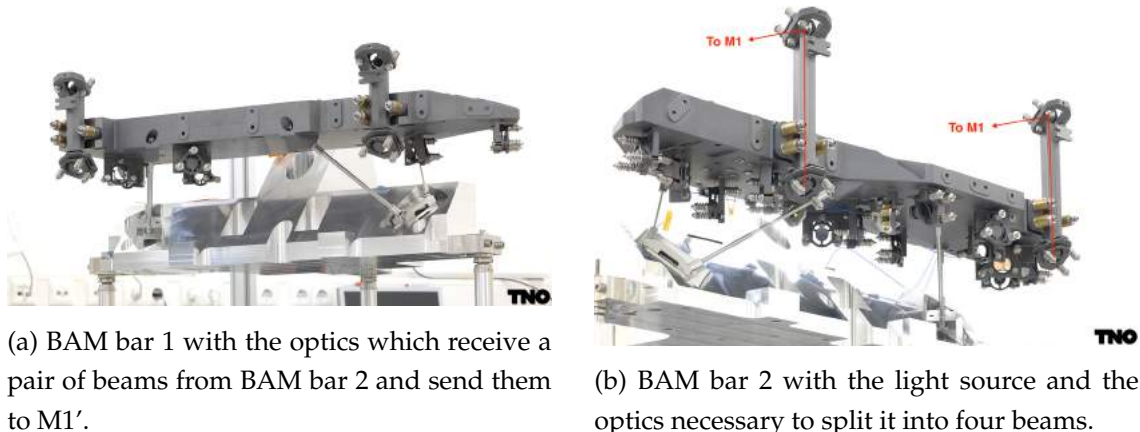


Figure 3.10: basic angle monitor bars which direct laser light onto the primary mirrors mounted opposite. The beam is split and bounced around on the underside of the bars before they are brought to the top and sent to the mirrors as indicated on bar 2. Images from the Netherlands Organisation for Applied Scientific Research (TNO).

There are two WFSs located on Gaia's focal plane. The purpose of each WFS is to measure the optical performance of each telescope (i.e. the prevalence of aberrations such as defocus), so that the system may be adjusted for optimisation. The WFSs are Shack–Hartmann WFSs. They contain an array of micro-lenses which focus star light crossing the focal plane onto a CCD (Mora et al. 2016). Comparing this image to a calibration source, adjustments may be made to

the M2 mirror using actuators to achieve the optimal image quality (Prusti et al. 2016). More information on Gaia’s WFSs can be found in Vosse et al. (2009).

3.3.3 Service modules

The mechanical service module consists of all the structural and thermal components of the spacecraft, as well as the propulsion systems, DPA and solar panels (de Bruijne 2012). Because of Gaia’s extreme stability requirements there are essentially no moving parts on-board (particularly heavy objects such as a reaction wheel). Gaia must move very slowly or suffer a loss of science. The Attitude and Orbit Control subsystem is thus custom built for Gaia. Every second each VPU sends up to 60 AL and AC star rate measurements from both telescopes to the Attitude and Orbit Control subsystem which are used to infer the spacecraft’s attitude and motion (Milligan 2016). Gaia contains a chemical propulsion system which is used for spacecraft manoeuvring (such as that during launch), and a micro-propulsion system which is used to make fine attitude adjustments (Prusti et al. 2016). The DPA was folded up prior to launch and is used to better thermally insulate the payload from the Sun. It also houses the solar panels and the *phased-array antenna*.

The electrical service module contains all the power and electrical components of the spacecraft, managing power distribution, data handling and communications. A schematic is shown in Fig. 3.11 illustrating many of these components.

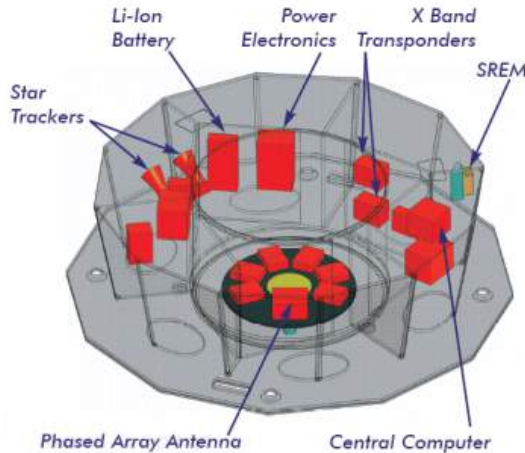


Figure 3.11: Electrical service module schematic showing component layout. Image from ESA.

3.4 Instruments

Gaia features three scientific instruments, utilising its two telescopes and an array of CCDs mounted on its focal plane (discussed in Section 3.3.2). These are the primary astrometric instrument which generates astrometric data and measures parallax, the blue and red photometers which take low resolution spectra, and the radial velocity spectrometer which takes high

resolution spectra of the calcium triplet. Also mounted on the focal plane are the sky mapper and metrology devices (discussed in Section 3.4.1 and Section 3.3.2 respectively).

As mentioned in Section 3.3.2 Gaia has three CCD variants which are optimised for particular electromagnetic regions. The instrument passbands are calculated as the CCD quantum efficiency convolved with the optics' (mirrors and dispersive optics) response curves and are shown in Fig. 3.12.

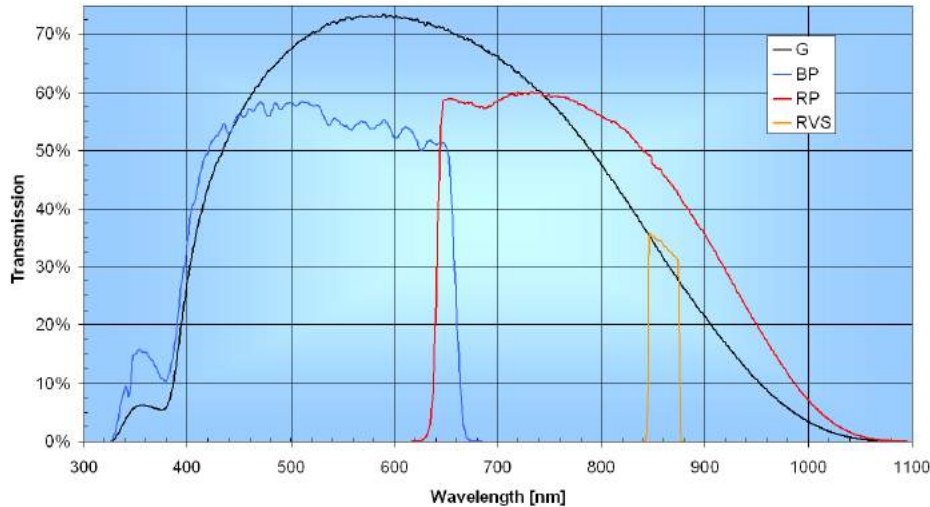


Figure 3.12: Transmissions of Gaia's instruments, accounting for telescope transmission, dispersive optics throughput and CCD quantum efficiency. Low resolution spectra are obtained across the entire G band. Image from ESA.

3.4.1 The Sky Mapper

The SM, though not usually considered as one of the scientific instruments on board Gaia, plays an extremely important role in measuring astrometry, and (it is expected) will produce its own scientific data at the end of the mission (Prusti et al. 2016). It plays the same, albeit updated, role as Hipparcos's star mappers³. There are two SMs which each consist of a strip of seven AF-type CCDs. Each SM corresponds to a particular field of view. There is a mask for each field of view at the M4/M4' beam combiner which blocks light from each field of view striking the opposite SM (de Bruijne 2012).

Unlike all other CCDs within the scientific payload of Gaia, SM CCDs are read out constantly in full-frame mode (as opposed to just reading out from a window). As such, fast pixel sampling is required and thus CCD readouts are noisier (Crowley et al. 2016). SM data also have reduced spatial resolution as they are binned into 2×2 pixel bins. The SM is thus used for initial detection to find objects of interest so that the other instruments may be ready for their transit.

³Though slightly confusingly they have subtly different names: *sky mapper* cf. *star mapper*.

Detection of an object works as follows: The SM CCDs are constantly being read-out; these data are sent to the VPUs which search for objects that are above 20.7th magnitude and that meet certain PSF and other requirements (as specified by the VPAs); if an object is deemed to be of interest the VPU marks from which field of view it came and calculates when it will arrive at each of the instruments, and draws a window around this region, whose size is dependent on the brightness of the object; the AF1 window is read out quickly to verify that the object is indeed an astronomical source, and not a false detection such as a cosmic ray; this window moves synchronously with the object across the focal plane and each of the instruments.

3.4.2 The astrometric instrument

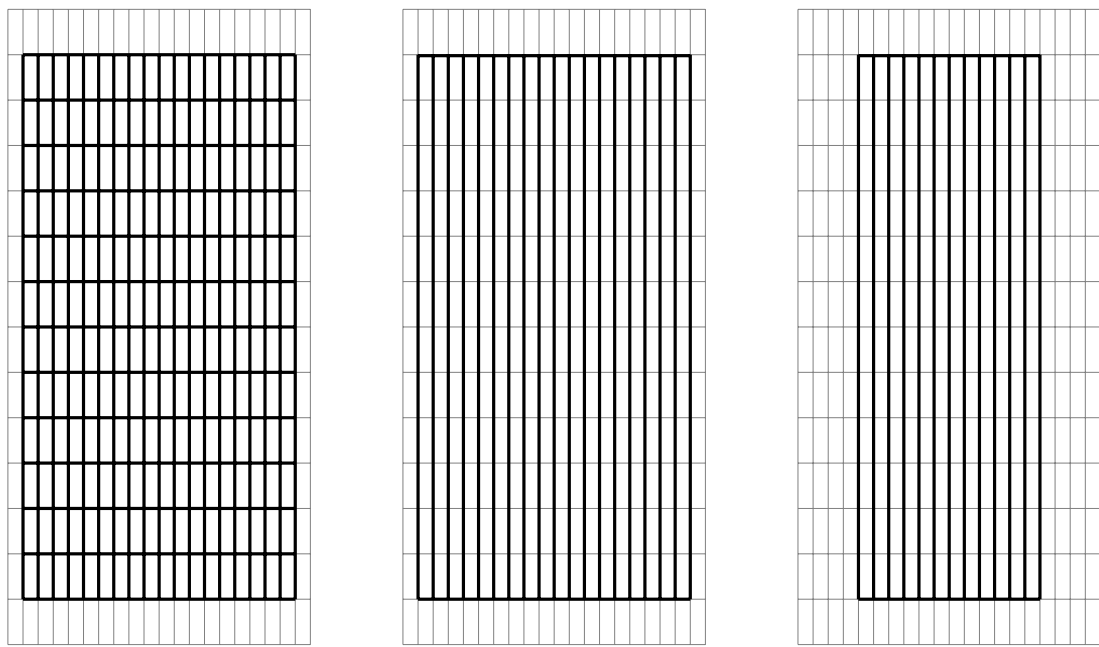
The astrometric instrument (ASTRO) is the primary scientific instrument on Gaia. ASTRO (along with the SM) is sensitive to light between approximately 330 nm and 1050 nm, known as the *G* band. It comprises 62 CCDs: nine strips (AF1–9), each with seven CCDs, except for AF9 which has six (one is used for the WFS, see Section 3.3.2). AF1 is somewhat separate as it is used to confirm or reject the SM detection of an object, to eliminate spurious detections (van Leeuwen et al. 2016). AF1 pixels are binned in pairs in the AC direction and have a higher readout frequency and noise level than the other AF strips (Crowley et al. 2016).

A provisional brightness and position is assigned to each object which is detected by the SM. AF1 implements its window and gate settings according to this brightness. The VPU also uses the difference in the SM’s and AF1’s position to refine the AL and AC spacecraft motion (see Section 3.3.3). The AF1 data are sent to the VPU to further refine the objects’ parameters, including brightness (van Leeuwen et al. 2016). These parameters determine what the position of the object will be as it crosses the other eight AF strips.

The brightness is used in drawing the readout window as it crosses the AF (shown in Fig. 3.13). All windows are 12 pixels AC, and objects brighter or dimmer than 16th mag are 18 pixels or 12 pixels AL respectively (Prusti et al. 2016). Pixels for objects which are brighter than 13th magnitude are not binned AC, and windows are thus two-dimensional providing AC localisation within the window. Conversely objects dimmer than 13th magnitude employ windows with their AC pixels binned providing no AC localisation within the window (Crowley et al. 2016). ASTRO can handle object densities of up to $1\,050\,000$ objects deg^{-2} (Prusti et al. 2016). Precise times are recorded as an object traverses the AF as it is extremely important to have precise times with each position measurement. These times are originally from the onboard mission timeline but are later transformed to barycentric coordinate time (Lindegren et al. 2016).

3.4.3 The photometric instrument

The photometric instrument consists of the BP and RP. This instrument is used to measure the spectral energy distribution (SED) of each object marked by the SM and AF1. The BP and RP contain a strip of the blue and red flavoured CCDs respectively, and a coated fused-silica prism (shown in Fig. 3.14) which disperses light from an incoming object across the strip in the AL direction (Carrasco et al. 2016). This light gets spread across approximately 45 pixels, therefore



(a) 18×12 pixel window used for objects with G mag in range 6–13.
(b) 18×12 pixel window used for objects with G mag in range 13–16. All pixels are binned in AC direction.
(c) 12×12 pixel window used for objects with G mag in range 16–20.7. All pixels are binned in AC direction.

Figure 3.13: Astrometric Field windows used for detection of various magnitude sources. AC pixels are binned for objects dimmer than 13th mag and the window therefore is one-dimensional. The size of the windows will have a large effect on extended sources as some of the light may fall outside the edge.

an AL window size of 60 pixels is used to record this spectrum to allow for background subtraction, as well as errors associated with choosing the window (Hudec et al. 2010; Prusti et al. 2016).

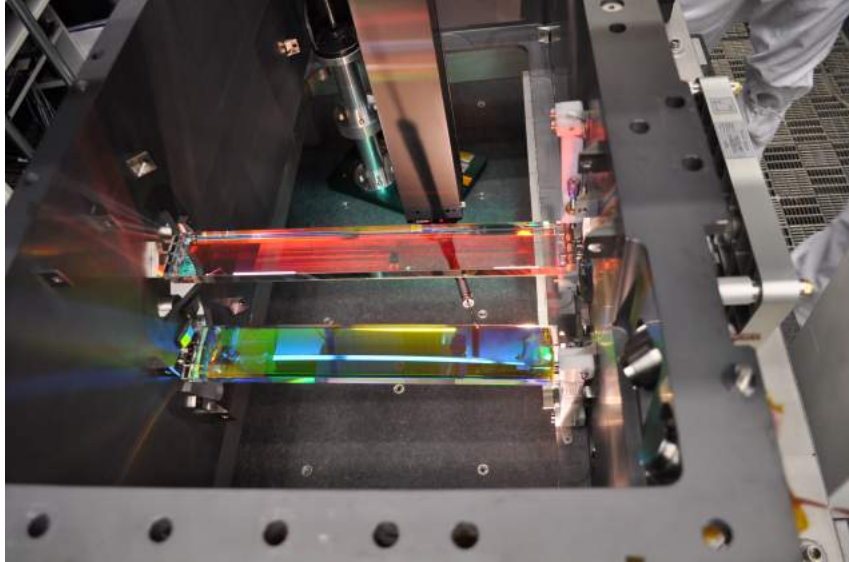


Figure 3.14: BP and RP prisms during testing. These disperse incoming light across the BP and RP CCDs. Image from ESA.

Windows of $60 \text{ pixels} \times 12 \text{ pixels}$ are used to record spectrophotometric data. As in the AF, AC pixels are binned for objects below a certain brightness. This brightness is 11.5 G mag for the photometric instrument. The photometers approximately bisect the G band as can be seen in Fig. 3.12, whereby the BP is sensitive in the range 330–680 nm, and the RP in the range 640–1000 nm (Jordi et al. 2010). This gives essentially even spectral coverage of the whole G band. The resolutions of the BP and RP vary across their bandpasses, however they are approximately 15 and 25 respectively. This instrument can handle the detection of up to 750 000 objects deg^{-2} (Hudec et al. 2010).

The photometric instrument is secondary to ASTRO but is extremely useful. As it is a broad band spectrograph (albeit low resolution) it provides another layer of information on top of the photometry obtained from ASTRO, which may be used to classify objects by temperature, metallicity, surface gravity, etc. It may also be used to infer reddening and extinction in the interstellar medium (Bailer-Jones 2010). The photometric instrument also plays an important metrological role as it is used to measure chromatic aberrations of the optical system and apply corrections to the astrometric data (Prusti et al. 2016)

3.4.4 The spectroscopic instrument

The RVS, also known as the spectroscopic instrument, is primarily responsible for measuring objects' radial velocities. It does this by measuring Doppler shifts around the Ca II triplet. Using a series of optics located between the M6 mirror and the focal plane, incoming light is greatly dispersed and cut off outside the range 845–872 nm before it reaches the RVS CCD array (Prusti et al. 2016). These optics consist of four fused-silica prismatic lenses, shown in

Fig. 3.15. The CCD array consists of three strips, each with four RP type CCDs. Because each strip has three less CCDs than all others (excluding AF9), it receives 43% less transits than the other instruments. This is acceptable as the RVS only detects objects below $G \approx 17$ (Brown et al. 2016).

By the time the RVS light reaches the focal plane, its light has been dispersed AL and is spread over approximately 1100 pixels, giving it a resolution of ~ 11700 . As an object traverses the focal plane, the VPU uses the RP data to estimate its RVS magnitude (G_{RVS}). Objects brighter than $G_{\text{RVS}} = 12.5$ may have their radial velocities directly inferred from a spectrum (Brown et al. 2016). Objects brighter than $G_{\text{RVS}} = 16$ may have their radial velocities derived from combining many measurements made over the course of the mission (see Recio-Blanco et al. 2016). The RVS employs a window size of 1296 pixels \times 10 pixels, slightly wider than the spectrum to allow for background subtraction and window errors (similar to the photometric instrument). AC pixels are binned for objects dimmer than $G_{\text{RVS}} = 7$ (Prusti et al. 2016). This instrument can handle the detection of up to 35 000 objects deg $^{-2}$ (Recio-Blanco et al. 2016).

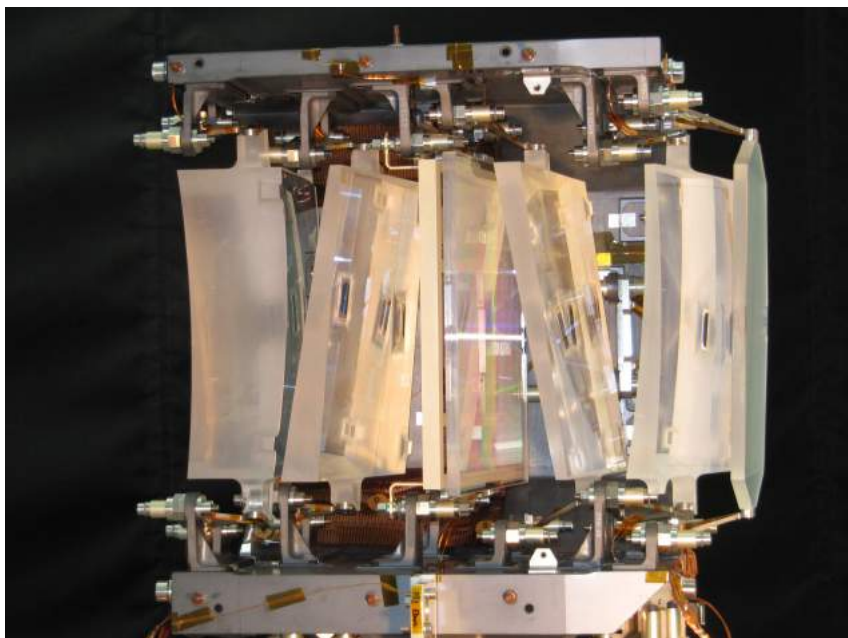


Figure 3.15: RVS optics used to disperse 845–872 nm light across the RVS CCDs. Image from ESA.

3.5 The astrometric solution

3.5.1 Parallax

Parallax is the apparent angular displacement of an object due to the displacement of the observer (Moore 2007). This effect is seen in everyday life but is particularly important in astronomy for measuring distances. The classic picture is shown in Fig. 3.16: If a star (or other astronomical object such as a planet) is relatively nearby compared to background stars, then a displacement will occur as the Earth moves from one side of the Sun to the other. This dis-

placement is called the parallax and by measuring it (and knowing the distance to the Sun), the distance to the star may be calculated. This is one of the most effective ways of measuring distance in astronomy but is challenging as these angles are typically very small and thus obscured by the atmosphere.

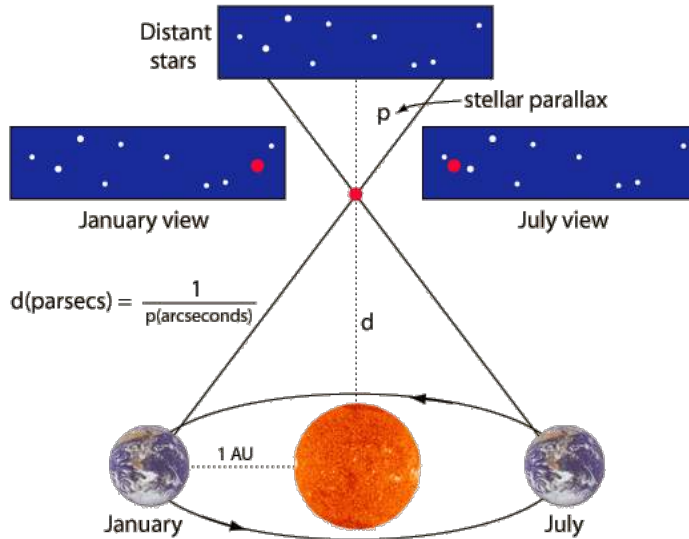


Figure 3.16: By measuring the parallax of a star from the opposite side of the Sun the distance to the star may be inferred from simple trigonometry. It is this principle on which Gaia distance measurements are based. Image from <http://joyceproject.com>.

Another problem with this method is that the background stars which are used as a reference are also moving themselves (always in the direction of the Sun), but it is the relative parallax between them which is measured. When observing stars within a small field of view, the measured quantity (made through multiple observations in a year), M , is given by

$$M = f(p_1 - p_2), \quad (3.1)$$

where f is the parallax factor of a telescope and is proportional to the sine of the angle which the telescope subtends to the Sun-observer axis (f will be 0 if the star is on the axis and no parallax will be observed, whereas max parallax will be observed if the star is perpendicular), and p_1 and p_2 are the parallax values of the star and background stars respectively. This is called *differential parallax* and is the standard distance measuring tool in astronomy. If p_2 is ignored then there exists an error in all parallax measurements and all distances are overestimated. p_2 is usually estimated and has an uncertainty of order mas (Lindegren and Perryman 1997). This is clearly unacceptable for a mission hoping to achieve μ as precision.

It is however possible to measure *absolute parallax*, i.e. the true value of p_1 , using two telescopes. By using two telescopes, Eq. (3.1) becomes

$$M = f_1 p_1 - f_2 p_2. \quad (3.2)$$

Separating these telescopes by a large angle ensures that $f_1 \neq f_2$. By making observations at various times in a year with two telescopes separated by a large angle, it is possible to solve for p_1 (and p_2) (Lindegren and Perryman 1997). By having an observatory in space (thus above the

atmosphere and its distortions) with two telescopes separated by a large angle mapping out great circles, a large number of M 's are measured and thus a large number of p_1 's can be very well constrained, leading to an ‘astrometric solution’ and a catalogue of precise distances. This principle was successfully demonstrated with Hipparcos and is currently being implemented by Gaia. It can be seen from Eq. (3.2) that the optimal choice for this separation is 90° as this will lead to a situation where $f_2 = 0$ and f_1 is maximal.

3.5.2 Choice of geometry

The AC parallax measurements contribute little towards the astrometric solution (see Lindegren and Bastian 2011), hence the rectangular pixels and AC pixel binning (see Section 3.3.2). The spacecraft geometry is therefore chosen to reflect the optimal setup for achieving the best AL parallax measurements. Keeping in mind that stars always move along the baseline towards the Sun in parallax leads to the setup of Fig. 3.17. The AL displacement of a star due to its parallax, ω , is given by $\omega \sin \theta$. We have seen from the previous section that in each field, the AL parallax is also proportional to $\sin \psi$. Therefore if $\psi_P = 0^\circ$, then the AL parallax for the following field is $\omega_F \sin \theta \sin \psi = \omega_F \sin \xi \sin \Gamma$, where ξ is the Sun separation angle and Γ is the basic angle employed by Gaia; conversely, for the preceding field the AL parallax is given by $-\omega_P \sin \xi \sin \Gamma$ (Lindegren and Bastian 2011). The parallax is thus proportional to $\sin \xi \sin \Gamma$.

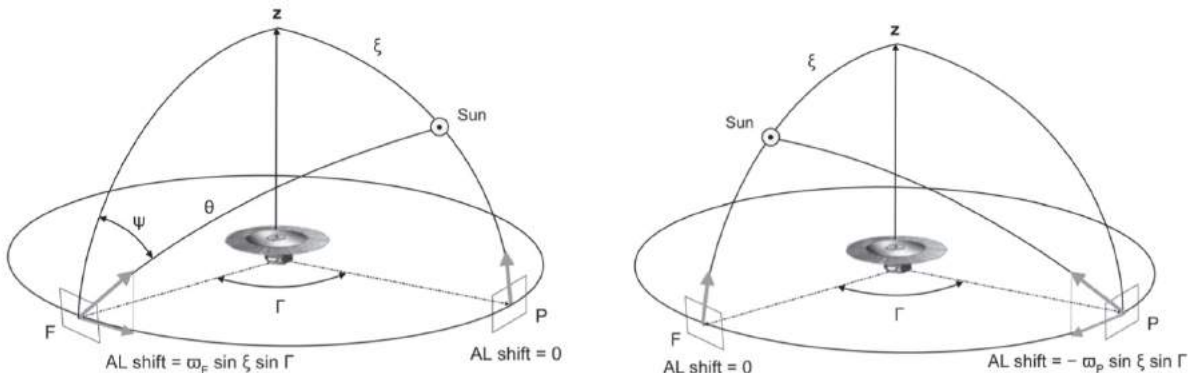


Figure 3.17: Geometry of Gaia where F refers to the ‘following’ field of view (FoV) and P refers to the ‘preceding’ FoV. Having two FoVs separated by an angle close to 90° allow precise measurement of absolute parallax. Image from Lindegren and Bastian (2011).

Mathematically the best choice for ξ and Γ is 90° , however neither were chosen as such. Setting $\xi = 90^\circ$ would cause the Sun to constantly shine on the payload, heating it to undesirable temperatures, and would even cause both FoVs to cross the Sun⁴. For optimal parallax 90° is ideal, but for optimal thermal performance 0° is ideal (leading to no parallax); 45° was chosen as high enough to achieve a good parallax while still being thermally stable (Prusti et al. 2016). In subtending a great circle many times resonances occur for $\Gamma = 360^\circ \times m/n$ when m and n are small integers. This means that it will only be possible to ‘connect’ (for parallax measurement)

⁴Hopefully it is clear to the reader that this would be bad.

a small group of stars; for example if Γ was set to 90° then each FoV could only possibly be connected to three other fields on that great circle. The relative variance of the positions on the great circle gives an indication of these resonances; a low relative variance implies that there is a good spread of positions on the great circle and there are few resonances, thus it is a good choice. Figure 3.18 indicates where these resonances occur. Interestingly these resonances actually disappear in the *global solution* (linking the whole sky sphere and not just a great circle) (Makarov 1998).

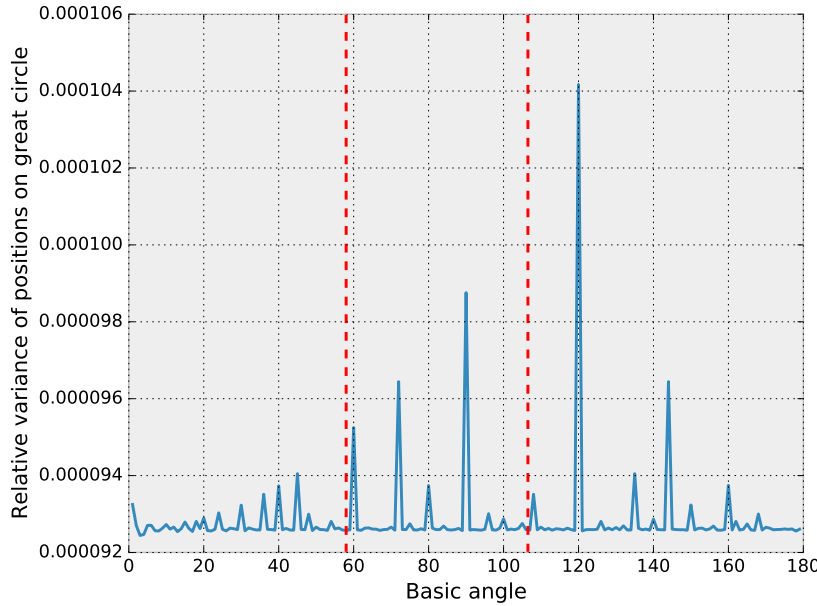


Figure 3.18: Relative variance of positions vs basic angle. Resonances can be seen at 90° , 60° , etc. due to them being ‘nice’ fractions of 360° . The dashed lines indicate the basic angle choice for Hipparcos (58°) and Gaia (106.5°).

The basic angles of Hipparcos and Gaia were still chosen to avoid these resonances so that a ‘local’ solution may be calculated intermittently. Several suitable basic angles were suggested for Gaia to avoid these resonances and 106.5° was chosen for design reasons. It is extremely important to keep the basic angle constant so as to maintain the validity of the parallax measurements. This is done using the BAM as discussed in Section 3.3.2.

3.5.3 AGIS

Gaia will acquire astrometric data for approximately one billion objects, which will feed into a global astrometric solution. This problem can be formulated as a minimisation problem, given by

$$\min_{s, n} \left\| f^{\text{obs}} - f^{\text{calc}}(s, n) \right\|_{\mathcal{M}} \quad (3.3)$$

where f^{obs} is the vector of all observations, f^{calc} is the vector of all corresponding calculations, s is the vector of astrometric parameters, n is the vector of ‘nuisance parameters’ which are not astrometric parameters but are still necessary to work out the solution (such as spacecraft

attitude), and \mathcal{M} is a metric defined by the data statistics (which need not be Gaussian) (Lindegren et al. 2012). The astrometric parameters for each object are two position coordinates, two proper motion elements and the annual parallax. The radial velocity is determined from RVS measurements and is thus not included in the astrometric solution. The astrometric solution will operate on a subset of particularly stable (primary) sources which will comprise about 10% of the total number of objects detected, leaving $\sim 5 \times 10^8$ unknown astrometric parameters. There are also $\sim 10^7$ nuisance parameters (O'Mullane et al. 2011).

A direct astrometric solution would require order 10^{25} floating point operations and would be infeasible (O'Mullane et al. 2011); rather, a global astrometric solution is obtained through a block iterative approach. Software was written to this effect by DPAC's CU3 (core processing); the Astrometric Global Iterative Solution (AGIS) was implemented in Java. AGIS models the effects of source, attitude, calibration and global parameters independently, whereby it fixes three and models the remaining effect. It repeats this process, and the effects are found to converge after 40–100 iterations (O'Mullane et al. 2011)⁵.

3.6 Mission science

As has been discussed previously, the primary scientific goal of the Gaia mission is to make a three-dimensional map of the Milky Way. This map is important in and of itself but also makes a direct contribution to many other science topics. As distance is such a difficult quantity to measure, and Gaia is doing so in an unprecedented way (both in terms of precision and volume) it will have a lasting scientific legacy. The so-called ‘distance ladder’ is the building of distance measurements upon each other out to larger scales; in this model each level directly depends on the level below. Gaia will provide a solid foundation on which to refine the rest of the ladder.

The final Gaia database is expected to be 1–2 petabytes in size (Luri et al. 2014). These data will contain astrometric, photometric and spectroscopic information about over one billion objects across the whole sky, taken over five years; by sheer richness and volume of data, the scientific reach of the Gaia mission will be vast, even into areas outside astronomy and physics such as data science. Some of the core scientific goals of Gaia are outlined below.

3.6.1 Galactic structure and evolution

As previously mentioned Gaia will create a three-dimensional map of the galaxy containing velocities as well as positions. This map will encompass 1% of the Milky Way’s stars but will extend far beyond 1% of the Milky Way’s volume as many stars within the brightest 1% fall outside this region. The map will extend to kpc in distance (Prusti et al. 2016). The positions of the stars describe galaxy features such as clusters, arms, bulge, etc. The velocities provide

⁵The process by which this is done is extremely involved and is excluded from this thesis. The reader is directed towards Lindegren et al. (2012) and O'Mullane et al. (2011) for in-depth descriptions of the mathematics and implementation respectively.

dynamical information about various parts of the galaxy but also may provide insight into the formation of these components through past accretion and merger events (de Bruijne 2012). Encoded in the positions and velocities is gravitational information which may provide insights into dark matter distribution in the galaxy (Lindegren and Perryman 1997).

The photometric and spectroscopic data may also be used to infer stellar types, temperatures, metallicities, etc.. This information will also feed into the galaxy map providing information about the distribution of these quantities across the galaxy. This information can also be used to estimate stellar ages (Perryman et al. 2001), and thus provide insight into the state of the galaxy at various times. As well as contributing to the understanding of the galaxy, a large sample stellar data also allows star models to be refined.

3.6.2 Variable stars

Gaia makes an average of 70 observations per object, giving it an average cadence of approximately 30 days. This allows it to detect variability on this time scale. Variable stars such as RR Lyrae and Cepheid variables are being detected by Gaia. Like parallax, these stars are often used as a distance measures in astronomy (known as standard candles), as their luminosity is connected to their period. Gaia data will further increase understanding of these objects and provide better calibration data (Prusti et al. 2016).

3.6.3 Binaries and exoplanets

The astrometric precision of Gaia is such that it may be able to resolve binaries (or multiple stars), and exoplanets. The astrometric data are complemented by the photometric and spectroscopic data which may also provide insight into these orbital systems. Gaia may permit measurements of masses in these systems (Prusti et al. 2016). Recent estimates suggest that Gaia will detect over 20 000 exoplanets (Perryman et al. 2014).

3.6.4 Solar System

Gaia will also detect thousands of Solar System bodies, primarily asteroids. Physical characteristics of several thousands of asteroids will be determined such as size, spin, shape, etc., as well as their positions and velocities. Masses may be determined from close encounters for approximately 100 asteroids (Lindegren et al. 2008). By looking close to the ecliptic plane, Gaia may also detect near-Earth asteroids and asteroids with exotic orbits to create samples of each. These asteroids move relatively fast and thus leave a characteristic smearing in the AF; an alert (see Section 3.7.1) may be sent to the ground so that photometric follow-up may be carried out on these objects (Prusti et al. 2016).

3.6.5 Extragalactic objects

About 500 000 quasars will be detected by Gaia and these provide anchors for the extragalactic reference frame which Gaia uses for alignment. Distances will not be obtained for these quasars but the photometric and spectroscopic data will be very useful in studying them (Lindegren et al. 2008). Though Gaia is optimised for point sources it will detect millions of unresolved galaxies (Prusti et al. 2016). It will provide an even sample of the sky for galaxies brighter than \sim 20th magnitude and the photometric and spectroscopic data will be useful for their study. Resolved galaxies may also be detected; these are very complicated for Gaia and their detection will depend heavily on the galaxy features (see de Souza et al. 2014 for a more detailed description).

Gaia will also detect many extragalactic transients such as SNe, gamma-ray bursts and TDEs. The photometric data may be used to compile a light curve, and the spectroscopic data may also provide insight. If a transient is identified an alert may be sent to the ground so that follow-up may be carried out (see Section 3.7.1). Investigating Gaia’s potential for detection of TDEs is the focus of this thesis and is discussed in later chapters.

3.7 Data products

As alluded to in Section 3.5.3, Gaia will produce a very large final dataset (1–2 PB). These data will be released into an archive after data processing has finished and the final global astrometric solution derived. Data processing is expected to continue for three–four years after the spacecraft is retired, so this final release is currently scheduled for 2022/2023 (Brown et al. 2016). DPAC will release certain data in stages preceding the final release⁶.

The first data release (e.g. Brown et al. 2016; Fabricius et al. 2016) took place on September 19 2016, 1000 days after launch. Astrometry and photometry were released for approximately one billion sources, including the 2 million Hipparcos/Tycho stars (Brown et al. 2016)⁷. There are three more releases scheduled to occur between the first and the last data releases.

3.7.1 Gaia photometric science alerts

The *Gaia Photometric Science Alerts* (Hodgkin et al. 2013) is an alternate Gaia data release channel for transient objects. Because Gaia primarily releases its data in stages (with a cadence of years), it was feared that interesting transients would be detected by Gaia and immediately lost as no one would be aware of the detection for years. For this reason a team was set up within Gaia tasked with detecting and releasing potentially interesting transient events observed by Gaia such as SNe, cataclysmic variables and TDEs. These detections are released soon after they are detected so that follow-up may occur on the ground.

⁶The *data release scenario* describes what data will be released and when, and may be found at <http://www.cosmos.esa.int/web/gaia/release>.

⁷A full summary and list of published papers relating to the first Gaia data release may be found on <http://www.cosmos.esa.int/web/gaia/dr1>.

Photometric Science Alerts began searching for transients in 2014, after the entire sky was observed at least once (approximately six months after initial operation). Currently raw data are downlinked from Gaia and receive some initial processing, these data are then sent through the Alerts Pipeline which searches for new sources (i.e. that weren't detected on a previous Gaia scan of that region of sky), and sources which have changed magnitude; the change in magnitude must be larger than a tunable specified value so that the number can be reduced to a manageable amount.

The Photometric Science Alerts are released from a website maintained by the team (<http://gsaweb.ast.cam.ac.uk/alerts/alertsindex>). Many astronomers around the world have subscribed to the Alerts stream where they are notified of alerts and can follow-up with an on-ground telescope. Currently average magnitudes (across all CCDs for a transit) are published along with unprocessed BP/RP data, though it was originally intended to release all instrument data (Hodgkin et al. 2013); however, transient astronomers are primarily concerned with photometric data in the interest of producing light curves. On-ground spectroscopic follow-up may be done if necessary.

Several transient detections have been made following Gaia observations. One notable example is *Gaia14aae* (Campbell et al. 2015) where an AM CVn star was discovered by Gaia. Detections were also found in Pan-STARRS-1 and ASAS-SN. An alert was published and a number of follow-up observations were made which allowed the orbital parameters of the system to be constrained. This was only the third eclipsing AM CVn star discovered (Campbell et al. 2015). Some SNe discoveries have also been claimed (e.g. Kangas et al. 2016).

3.7.2 GAVIP

The Gaia Added Value Interface Platform (GAVIP) (Vagg et al. 2016) is a platform which will provide access to the Gaia archive through a portal system. Traditionally astronomers would download a large dataset containing some data they are interested in; they would do some (usually undisclosed) processing and analysis on this data to extract their science, and publish the results. GAVIP provides a platform where astronomers can upload their (probably small) algorithms to the (potentially very large) data and download their results. It may be accessed through a web interface making it suitable for sharing code and data (and making the science more transparent). GAVIP was developed by *Parameter Space Ltd.* in Dublin.

GAVIP is based in *Python*, which has a rich set of libraries used for data analysis, and strong community support. Software is uploaded to the platform in the form of Added Value Interfaces (AVIs). AVIs contain the data processing and analysis which an astronomer may want to perform on Gaia data, and can be *RESTful*, or wrapped in a web-based frontend to provide a user-friendly experience; the latter is particularly useful for sharing algorithms or outreach. The platform also encourages transparency in data analysis by facilitating code sharing, a feature which is becoming increasingly important in science. As data continues to increase these platforms will become ubiquitous.

Summary

Gaia is an optical observatory currently orbiting the second Lagrange point of the Earth-Sun system. Gaia's primary function is to measure precise distances to approximately one billion stars in the Milky Way. To do this, it employs the same methodology as its predecessor Hipparcos, but utilises decades of advancements in technology. Gaia continually scans the whole sky gathering data which is fed into its astrometric solution to refine astrometric parameters. Gaia consists of a very sophisticated payload comprising an astrometric instrument, photometric instrument and spectroscopic instrument collectively utilising approximately one billion pixels. The readout software on board Gaia is such that it minimises the amount of useless data, and the final archive, which is scheduled for release in 2023, is expected to be PB in size. The scientific reach of Gaia is widespread and will include transient astronomy.

Chapter 4

Sample Generation and Simulation of Gaia Observations

4.1 Motivation

Gaia is continuously scanning the sky and gathering data during its five-year nominal lifetime. It is optimised for detecting point sources such as stars but will observe many extragalactic sources such as galaxies, and transients (e.g. SNe and TDEs). These data will contain rich photometry and spectroscopy, particularly useful for classification and analysis of transient sources. Gaia data, however, is mostly being released in stages (see Section 3.7), and transient data will not appear in the archive until the final release. As described in Section 3.7.1, some transient data will be released as they are detected so that photometric follow-up may be achieved.

This thesis is assessing the suitability of Gaia for detecting TDEs. Gaia may detect TDEs (or other transients) which it will release through the Gaia Photometric Science Alerts (PSA); in this case, Gaia need merely detect a magnitude change according to the PSA team's specifications (0.5–1 mag) and on-ground follow-up may be done with instruments such as ASAS-SN (Shappee et al. 2012), Pan-STARRS (Kaiser and Pan-STARRS Team 2002), the Intermediate Palomar Transient Factory (Rau et al. 2009) or the Watcher telescope (French et al. 2004), which are more suited to transient observation than Gaia. Data will be gathered as Gaia makes successive passes over the transient object but Gaia's role here lies in identification of 'a transient' before passing over to astronomers who may utilise optimised observatories. This scenario is ideal as it affords astronomers the chance to gather data in real time according to specifications best suited for each object.

It is also anticipated¹ that Gaia will detect many TDEs which will not be released as alerts, either because they were missed by the detection pipeline or because they did not meet the alert criteria. As mentioned in Section 3.7.1, it took some time for PSA to become fully operational and it is continually being developed, but reduced performance and down time at the start will

¹According to estimates (Blagorodnova et al. 2015), Gaia should already have observed some TDEs but none have yet been released as an alert.

have caused transients to be missed. By the time these data are released in the final archive, it is likely that most or all of the observable part of the light curve has been missed, and it may be too late to perform photometric follow-up. This thesis aims to determine the photometric appearance of a TDE in the final archive and what these data can contribute to understand this family of sources.

As the final archive, and thus these data, will not be available for several years, it is therefore necessary to simulate these sources. This was one of the motivations behind DPAC’s CU2 (data simulation); another being to prepare for the stream of data that Gaia would be generating. CU2 produced various tools to simulate instrumental effects, primarily the Gaia Object Generator (GOG), the Gaia System Simulator (GASS) and the Gaia Instrument and Basic Image Simulator (GIBIS) which together form the *Gaia Simulator*.

GOG (Antiche et al. 2014) simulates transit catalogues for various data releases (including the end-of-mission release). It provides data in the format that is being used for real data releases. GASS (Masana et al. 2005) simulates the telemetry stream which is transmitted from Gaia. It was primarily used in the pre-launch stage to test data ingestion and processing algorithms. GIBIS (Babusiaux 2004) is a pixel level simulator of sources observed by Gaia. Though Gaia does not produce typical CCD images, GIBIS also renders images so that users may better understand Gaia’s detection process. GIBIS was chosen for this project as it provides a flexible facility for defining source and observation parameters, and removes the need to interface with the archive. The images also provide a useful diagnostic tool for performing test simulations to choose optimal parameters.

4.2 GIBIS

4.2.1 The Gaia Simulator

GIBIS forms a part of the Gaia Simulator. This software consists of a ‘common toolbox’ known as `gaiasimu` and the three ‘data generators’ mentioned in Section 4.1 (Luri et al. 2005). GIBIS is a pixel level simulator of Gaia observations, GASS simulates Gaia’s telemetry stream, and GOG simulates Gaia catalogue data. The structure of these tools is illustrated in Fig. 4.1. `gaiasimu` is integrated with each of the data generators and includes models for celestial objects and the spacecraft (motion and instruments), which are used to simulate what and how the data generators ‘observe’.

4.2.2 GIBIS operation

GIBIS was developed during the design phase of Gaia primarily for testing and optimising the mission design and testing on-board algorithms. As it simulates a real Gaia response it could also be used to provide data to GASS to test and optimise Gaia’s telemetry. With the chosen Gaia design integrated into later versions it also provides a means to test how Gaia observes particular sources. GIBIS, along with `gaiasimu`, produces realistic Gaia data by folding a sky

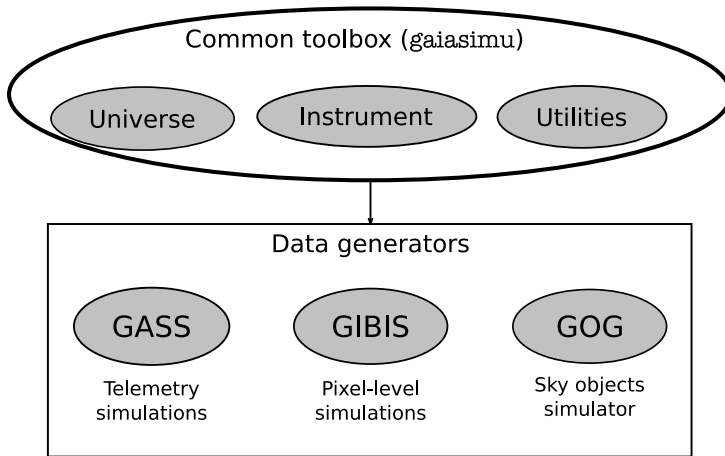


Figure 4.1: Structure of Gaia Simulator. The three high-level components are GASS, GIBIS and GOG, which all make use of gaiasimu.

model (often with additional user-defined sources) through the instrument’s response and the on-board data handling process (Babusiaux 2004).

GIBIS is an extensive *Java* application, separate to but packaged with gaiasimu. It is capable of simulating stars and other point sources (such as quasars), unresolved galaxies, solar system objects (primarily asteroids), and user-defined sources. A background may be added to the field which is then passed through the instrument response model. This model simulates the response to the telescope pointing (from the scanning law), telescope optics, CCD response, and data handling (Babusiaux 2004). GIBIS utilises other external simulation tools for some simulations such as *Stuff* and *SkyMaker* (Bertin 2009).

Also integrated in GIBIS is the VPA response. This response is packaged in binary files developed by Astrium, which act identically to Gaia’s VPA response² (Babusiaux et al. 2015). Unlike Gaia, however, GIBIS simulations return Flexible Image Transport System (FITS) files as well as Gaia’s response to allow a user to visualise exactly how Gaia responds to particular sources. GIBIS was previously wrapped in a web platform which allowed users to define simulations using a ‘point and click’ interface, hosted by le Centre national d’études spatiales (CNES) (Babusiaux 2004). This interface was removed before the commencement of this project, therefore all simulations were run through the command line interface. This is described in Babusiaux et al. (2015).

4.2.3 GIBIS input

Using the command line interface, all GIBIS simulation parameters are defined in a `.GibisInput` file (Babusiaux et al. 2015). This file makes reference to a `.pix` file from which user-defined sources are read. The parameters defined in these `.pix` files are motivated in Sections 4.3 and 4.4. Most instrument parameters were left as the Gaia defaults to simulate a realistic Gaia observation; however, some parameters were changed to simplify the investigation and reduce

²The VPA binary files are proprietary and could not be obtained so simulations were run externally by Carine Babusiaux.

computation time.

As described in Chapter 3, Gaia gathers data for a source over five years, crossing it at a different angle each time. Each time it passes over a source it collects data on its many CCD columns. This technique was chosen to maximise astrometric performance, but this thesis aims to investigate Gaia’s potential to perform science which falls outside its primary astrometric goal. Many of the features that are employed to maximise astrometric performance have been implemented in GIBIS, but are disabled in this work in order to decrease computational time.

The main question addressed in this work is whether a TDE is detected. Since TDEs occur on top of galaxies, these will also be investigated, on their own and with a TDE. Though gathering more data would improve statistics for each detected source, the ‘yes or no’ detection happens in the SM and AF1 column (leaving the answer in AF2), thus the AF3–9, BP, RP and RVS columns are not simulated as it was deemed to be a better use of computational time to answer this question for more sources than to improve statistics on the detected sources. For the same reason, the scanning law was disabled in the simulations, limiting ‘observations’ to one per source. This has the caveat that the detection of extended sources should depend on the angle at which which Gaia crosses the source (due to the rectangular pixels and the AC pixel binning), but this effect was accounted for by varying the position angle of the simulated galaxies (see Section 4.3.2).

GIBIS is an extensive application and simulations are computationally expensive so efforts were made to reduce the number of simulations: A grid of sources was placed on each simulated field. These were placed at wide enough intervals so as not to affect each others’ detection (discussed in Section 4.5). This makes the simulated field unrealistic, but each source is detected and reduced separately so this is unimportant. The sky background was disabled as it would obscure many of the sources in the grid due to the artificially high source density. This has no effect on the simulations except that in reality, some of the sources would be totally or partially obscured by background stars, perhaps rendering them unidentifiable or identifying them as another object.

4.3 Galaxy simulations

TDEs generally occur around a SMBH at the centre of a galaxy. When observing potential TDEs, it is likely that the parent galaxy will also be detected. This galaxy can affect observations of the TDE in several ways: If the galaxy, particularly its bulge, is bright, then this light can ‘dilute’ that which is coming from the TDE, potentially to the point where the TDE is never identified; if spectral imaging is undertaken, the galaxy will make a contribution to the spectrum which must be subtracted. These problems may be overcome by subtracting photometric or spectral data taken before or after the occurrence of the TDE, however, this depends on the existence of these data and is therefore not always possible.

This information may also be used to infer (or at least improve certainty of) the existence of a TDE as these must occur around extremely massive objects, such as the SMBHs found at the

centre of all galaxies. It is particularly important to understand Gaia’s response to galaxies in TDE detection as Gaia will only detect objects above a certain brightness (see Section 3.4.1), and in some cases this may not include the galaxy but may include the TDE. Also, Gaia will have been decommissioned years before the archive data are released so it will often not be possible to take follow-up data. As part of this investigation, Gaia’s response to galaxies was explored with the view to better understanding what would be observed if a TDE occurred in such galaxies. This work is complementary to that of de Souza et al. (2014).

4.3.1 Galaxy samples

GIBIS contains a predefined galaxy type whose parameters may be set in the input files. Two samples of galaxies were obtained in the interest of extracting a distribution range for each parameter. Both these samples were extracted from the SDSS (York et al. 2000) database. SDSS is a 2.5m optical survey telescope in New Mexico which began operation in 2000 (York et al. 2000). It is still operational and in the time it has been active has produced 13 large data releases (SDSS Collaboration et al. 2016), including a large sample of galaxies (e.g. Kim et al. 2016). This makes it ideal for extraction of a sample of galaxies for simulation with GIBIS.

The first sample is from a study by Kim et al. (2016) (and will be referred to as the ‘Kim sample’) whereby a database of 14 233 two dimensional bulge-disk decompositions was created using the *GALFIT* software (Peng et al. 2010; Peng et al. 2002). This is a very useful sample as many of the parameters derived are those which are required by GIBIS as inputs, and fit to galaxy bulges and disks; however, only SDSS *g* and *r* band data are provided, making it difficult to derive GIBIS’s desired colour data (*Johnson V – I*) using standard transformations³. This sample also only contains spiral galaxy data. Galaxies were selected from SDSS data release (DR)12 which were brighter than $r = 17.77$ mag within the redshift range $0.005 < z < 0.05$ (Kim et al. 2016).

To accommodate the lack of *V – I* data and include ellipticals, a second sample was obtained. This sample was extracted directly from the SDSS archive using a Structured Query Language (SQL) query (and will be referred to as the ‘SQL sample’) which is shown in listing 4.1. This sample utilises information from the *Galaxy Zoo* project (Lintott et al. 2008), a *citizen science* project which derives galaxy classifications from votes by approximately 2×10^5 citizen scientists through a web interface⁴. Through this interface objects are voted as spiral galaxies, elliptical galaxies, mergers or something else/inconclusive (Lintott et al. 2008). These data are fed back into the SDSS database as an SQL table from which data may be extracted.

Galaxies were chosen with a debiased⁵ vote fraction greater than 0.8 (Lintott et al. 2011). From these galaxies, the *cModelMag* value for the *g*, *r* and *i* filters was extracted. These values are obtained by fitting de Vaucouleurs and exponential profiles to the object (as GIBIS uses).

Listing 4.1: SQL query for attaining SDSS filter data

³<http://www.sdss.org/dr13/algorithms/sdssubvritransform/>.

⁴galaxyzoo.org.

⁵Interestingly, human psychology introduces biases and data must therefore be *debiased* (Lintott et al. 2011).

```

SELECT ALL
    p.objid,p.ra,p.dec,p.cModelMag_g,p.cModelMag_r,p.cModelMag_i,
    z.spiral, z.elliptical
FROM PhotoObj AS p
JOIN zooSpec AS z ON z.objid = p.objid
WHERE
    z.spiral = 1
    OR z.elliptical = 1

```

4.3.2 Galaxy simulation parameters

Using the conversions from Lupton (2005), Johnson V and I band data were derived from SDSS's g , r and i data. The preset galaxy simulations are achieved using *Stuff* (Bertin 2009). Galaxy bulges follow a de Vaucouleurs profile of effective radius R_B , i.e.

$$I_B(r) \propto \exp\left(-7.67\left(\frac{r}{R_B}\right)^{1/4}\right); \quad (4.1)$$

while galaxy disks follow an exponential profile with disk scale length R_D , i.e.

$$I_D(r) \propto \exp\left(-\frac{r}{R_D}\right). \quad (4.2)$$

Galaxy parameters were chosen to provide a broad sample and are described below. Key parameters such as brightness are varied between three values. Minor or incidental parameters such as position angle are assigned a random value within a valid range. Each combination of key parameters is simulated 500 times for ellipticals and 100 times for spirals (each with a unique combination of incidental parameters). As simulations are done in a Monte Carlo fashion it is necessary to simulate a large number of galaxies so that the results are statistically significant. There are 3^n combinations of n key parameters. Some of these parameters were refined through test simulations carried out, and this process is discussed in Section 4.5.2.

Position

Source positions are defined with respect to the ‘observation centre’ in pixel displacement. As mentioned in Section 4.2.3, this observation centre falls on the centre of the sixth row of the focal plane CCD array and coordinates refer to the displacement in the AL and AC directions. As mentioned in Section 3.4.2, Gaia’s AF is able to handle an object density of approximately 1×10^6 sources deg $^{-2}$. Knowing that there are 4500×1900 pixels in each CCD, and each CCD corresponds to 59 mas \times 177 mas on the sky, leads to

$$\begin{aligned} 1 \text{ deg}^2 &= 1.296 \times 10^{13} \text{ mas}^2 \\ \implies 1 \times 10^6 \text{ sources deg}^{-2} &\approx 7.716 \times 10^{-8} \text{ sources mas}^{-2} \\ &\approx 8.058 \times 10^{-4} \text{ sources px}^{-1} \\ &\approx 6889 \text{ sources CCD}^{-1}. \end{aligned}$$

Laying these sources out in a rectangular grid which has the same aspect ratio as the CCD gives a grid of approximately 53.93×127.7 sources, and thus a source separations of 35.23 pixels, i.e. sources must be separated by at least this value to be detected separately. However, as described in Section 4.5.2, GIBIS was found to be unable to handle fields of this density. Source positions were chosen to optimise computation time with minimum effect on the results after several trial simulations.

Brightness

As an extended source, a galaxy's detected brightness will generally be lower than its intrinsic (apparent) magnitude due to the fact that some of the source will fall outside the detection window and to PSF fitting. A Johnson V magnitude and $V - I$ colour are provided to GIBIS, and extrapolated across the whole G band. For galaxies, according to preliminary simulation the G magnitude is found to be approximately 0.5 mag below the V value. Thus an upper magnitude was chosen as $V = 21$; beyond this value, no galaxies would be detected, and at this value the detection efficiency is expected to be heavily dependent on the size of the galaxy. V was varied in 3 magnitude steps down to 15th magnitude to give broad coverage while reducing the number of simulations.

Colour

The primary reason for acquiring the second SDSS data set was to obtain colour data. Elliptical galaxies are dominated by older stellar populations than spiral galaxies, giving them redder colours (Binney and Merrifield 1998). The SQL sample was separated into elliptical and spiral galaxies and their $V - I$ values histogrammed. The result is shown in Fig. 4.2.

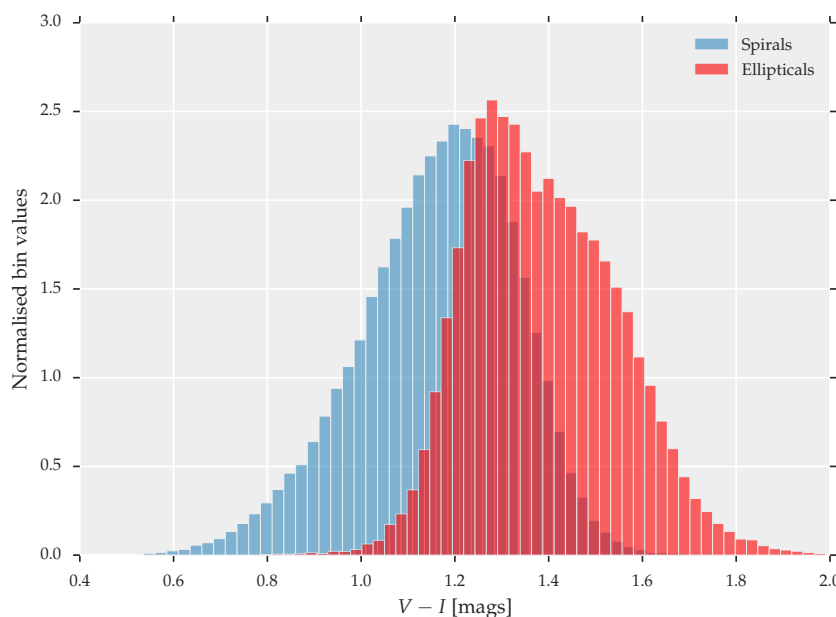


Figure 4.2: Histograms of spiral and elliptical $V - I$ values from the SQL sample of SDSS data.

For each elliptical simulation, $V - I$ was chosen uniformly from the range $[1.15, 1.6)^6$, chosen as approximately the mean minus and plus the interquartile range.

Spirals are bluer than ellipticals, but the spiral bulge approximates an elliptical and is therefore redder than the total galaxy. The overall $V - I$ value for a spiral galaxy will thus be a function of the bulge to total ratio, B/T . From the Kim sample, it is seen that there is an approximately linear relationship between B/T and $(V - I)_{\text{sp}}$. One also assumes that as $B/T \rightarrow 1$, $(V - I)_{\text{sp}} \rightarrow (V - I)_{\text{el}}$ (since ellipticals are approximated as spiral bulges). These assumptions provide the coordinates of two points on the $V - I$ vs B/T line and thus a linear relation. $V - I$ values are chosen according to this relation plus or minus a random value in the spiral interquartile range.

Size

Radii are provided to GIBIS in arcseconds. Gaia's maximum detection window size is 12×18 pixels (see Section 3.4.2). Converting this to arcseconds gives

$$(12 \times 18) (59 \text{ mas} \times 177 \text{ mas}) = 2.256 \times 10^6 \text{ mas}^2 = 2.256 \text{ as}^2. \quad (4.3)$$

Radii were chosen to provide a sample of galaxies the majority of whose light falls inside the detection window and a sample the majority of whose light falls outside the detection window, while also staying realistic (from the Kim sample).

Figure 4.3 shows the three radii which were chosen as effective radii for elliptical galaxies. As can be seen, most of the $0.5''$ galaxy's light will fall inside the detection window. The $5''$ galaxy is one which will have most of its light fall outside the detection window. The $2''$ galaxy provides a midpoint whereby most of the light will usually be detected.

These same radii were used for disk scale length of the spiral galaxies. The ratio of bulge effective radius to disk scale length was kept constant to reduce free parameters and thus simulation time. Two correlations can be seen in Fig. 4.4; one of these correlations has $R_{\text{disk}} < R_{\text{bulge}}$ and is discounted as the disk would be 'consumed' by the bulge and these would essentially just look like ellipticals; the other correlation has $R_{\text{disk}} \approx 3R_{\text{bulge}}$ and this was used for these simulations.

Ellipticity

Ellipticity is defined by Lapedes (1978) as

$$\epsilon = 1 - b/a,$$

where b/a is the minor to major axis ratio, which is what is fed as a parameter to GIBIS. The minor to major axis ratio was deemed to be a key parameter as stretching the galaxy, especially in the AL direction, may cause more of the galaxy light to fall outside the window. The minor

⁶The upper open nature of the range is due to a convention in the Python language; however, the high value is chosen up to machine precision of 1.6.

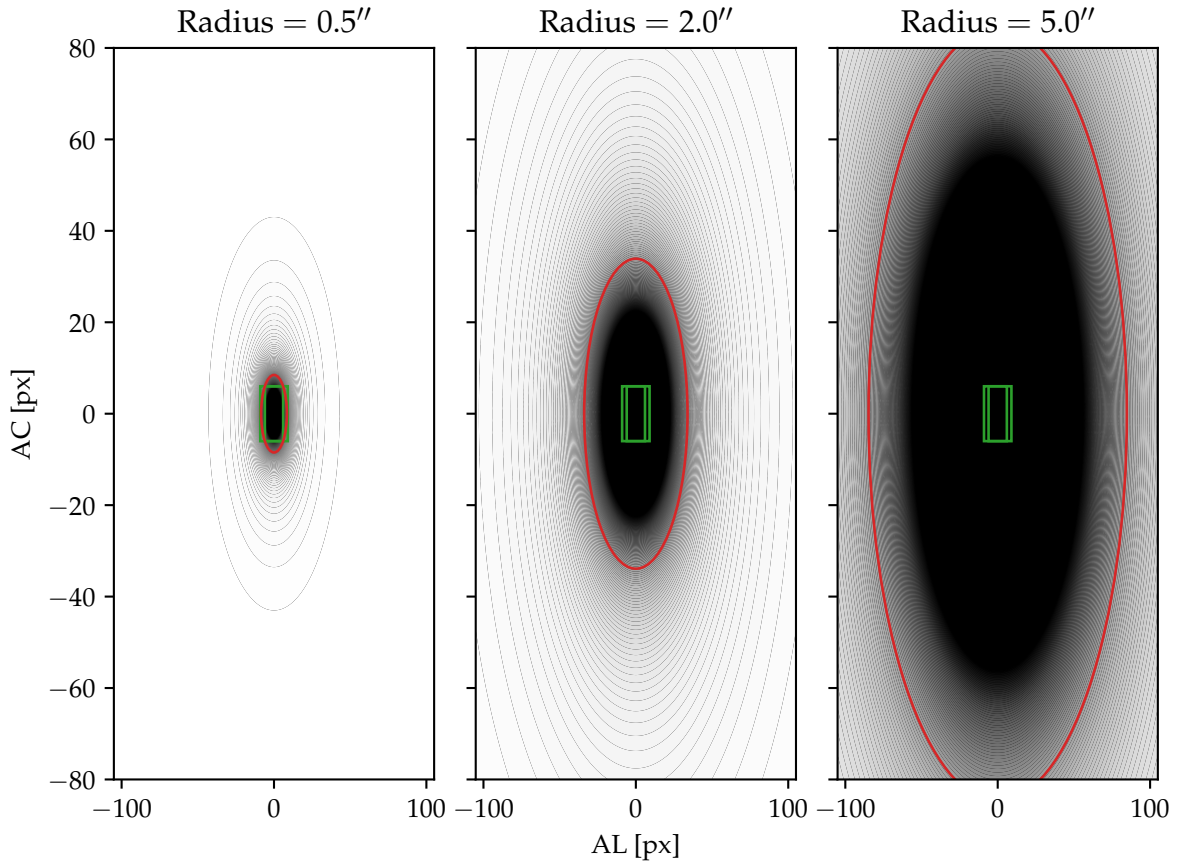


Figure 4.3: Elliptical galaxies with chosen effective radii. The red ellipses are the isophots containing 50% of the light from the galaxy. The green rectangles represent the 12×18 px and 12×12 px Gaia detection windows respectively.

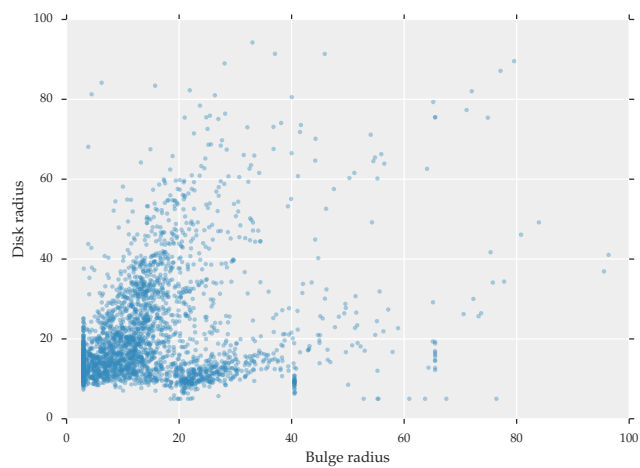


Figure 4.4: Disk radius vs Bulge radius for Kim sample. A correlation of $R_{\text{disk}} \approx 3R_{\text{bulge}}$ can be seen amongst the data and was employed in order to reduce simulation parameters.

to major axis ratio of the galaxies was chosen to represent different galaxy classifications as described by ‘Hubble’s tuning fork’ (Hubble 1926) (see Fig. 4.5). These were E0 (circular), E3/4 (elliptical) and E7 (highly elliptical).

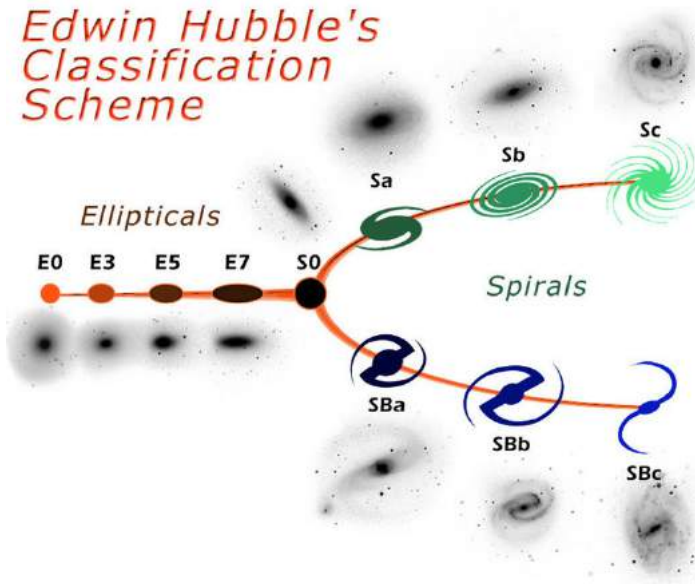


Figure 4.5: So-called ‘Hubble’s tuning fork’ diagram of galaxy classification. Elliptical E0, E3.5 and E7 galaxies were chosen for simulation. Image from ESA.

$\epsilon = 0$ is indicative of a circular E0 galaxy. $\epsilon = 0.7$ is representative of E7 galaxies, the most elliptical (van den Bergh 1998). $\epsilon = 0.35$ represents E3/4 galaxies. These values were also used for the spiral galaxy bulges. The disk was assigned a circular profile, again to reduce simulation time. Increasing the ellipticity also simulates tilting a galaxy around the axis perpendicular to an observer’s line of sight. In this way, information is also provided about how Gaia observes galaxies which have different inclinations.

Position angle

There is no reason to assume a bias in galaxy position angle since it is merely a result of the direction an observer views the galaxy. However, it is anticipated that this parameter will change the effect of the ellipticity. The bulge position angle (i.e. elliptical and spiral bulge position angles) were varied randomly from $0\text{--}360^\circ$. The relationship of the bulge and disk position angles was investigated in the Kim sample, and there was a correlation observed at approximately $\theta_{\text{bulge}} = \theta_{\text{disk}}$ (seen in Fig. 4.6). Therefore spiral galaxy disk position angles were set equal to bulge position angles.

Redshift

All photometric parameters which would vary with redshift (brightness, size, etc.) are explicitly specified, nullifying the redshift parameter in these simulations. The redshift is used solely for spectroscopic simulations in the BP, RP and RVS. Since this work is not concerned with

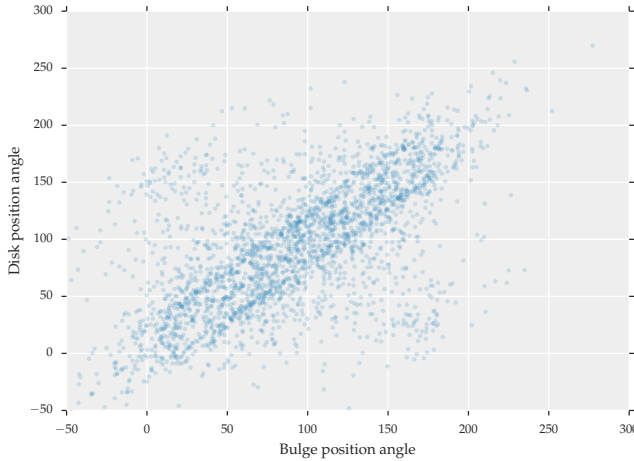


Figure 4.6: Disk vs bulge position angle showing correlation for $\theta_D \approx \theta_B$.

spectral data, and the generating instruments are not even read out, this parameter is completely inconsequential. The redshift was thus left at a constant value for all simulations.

Bulge/total ratio

GIBIS expects a bulge/total ratio (B/T), where the ‘total’ refers to the sum of the light from the bulge and the disk, i.e. $T = B + D$. B/T is thus related to B/D by

$$\begin{aligned} B/T &= \frac{B}{B+D} \\ &= \left(\frac{D+B}{B}\right)^{-1} \\ &= \left(\frac{D}{B} + 1\right)^{-1} \\ &= \frac{1}{B/D^{-1} + 1}. \end{aligned}$$

As mentioned above, ellipticals are assumed to be equivalent to spiral bulges in this work, thus giving $B/T_{\text{el}} = 1$. For spirals, there is a wide spread of B/T values seen in the Kim sample; though lower values are more common. In this work as $B/T \rightarrow 1$ the galaxy tends to being elliptical, so high (close to 1) B/T value spirals are avoided as these would be quite similar to ellipticals. $B/T = 0.1, 0.4$ and 0.7 were chosen to provide an even spread across the spiral B/T range.

4.4 TDE simulations

The strategy for simulating Gaia’s response to TDEs is to place a TDE (a point source whose light curve exhibits a sharp rise to a peak before falling off as $t^{-5/3}$) on top of the centre of a galaxy and run the GIBIS simulator on this source pair.

4.4.1 Synthetic light curve

Functional model

GIBIS was not designed to simulate transient sources⁷, and as such, a time dependence may not be taken account of in a simulation. An easy way around this though is to estimate when Gaia will observe a transient object and simulate each observation as a snapshot in time. This is particularly suited to TDEs since they are transient over a relatively long period. In order to do this, a synthetic light curve was to be defined and sampled in a manner similar to Gaia.

The key characteristics of this synthetic light curve are a sharp rise to a peak brightness followed by a decay which tends to $t^{-5/3}$. Accretion rates have been derived by several using hydrodynamical simulations (e.g. Bonnerot, Rossi and Lodato 2016; Evans and Kochanek 1989; Guillochon and Ramirez-Ruiz 2013; Lodato et al. 2009; MacLeod et al. 2012), which are shown to tend to the $t^{-5/3}$ rate at later times. As discussed in Section 2.4.1, this signature has also been seen in the optical luminosities. The light curve rise is a complex function of the system properties and thus requires hydrodynamical simulations to model. Hydrodynamical simulations were not feasible for the scale of this project so a simplified model was chosen where the light curve rises according to a power law.

The model employed for the TDE light curve was chosen such that it gives similar light curves to the simulations of Guillochon and Ramirez-Ruiz (2013). As the star is ripped apart and matter accreted onto the black hole, light is emitted according to an increasing power law, At^μ ; this corresponds to a line of slope μ in log space. The accreting matter eventually runs down and the light levels off before starting to fade, tending to $t^{-5/3}$. In derivative log space this starts off as a horizontal line at $y = \mu$, it smoothly drops passing through the x axis and levels off again at $y = -5/3$. This is the (upside-down) shape of a hyperbolic tangent function (shown in Fig. 4.7).

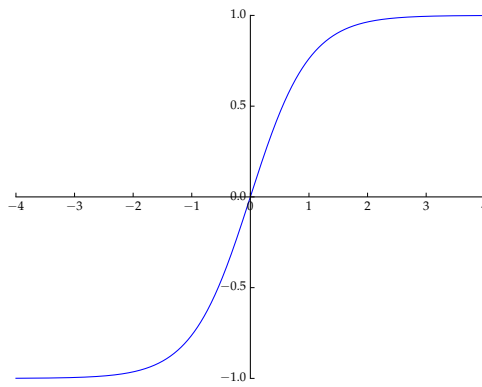


Figure 4.7: Hyperbolic tangent function. This function was adapted as the derivative of the TDE synthetic light curve.

By inverting, scaling and shifting this function, it can be made to aptly describe the slope of the

⁷This does not come as a surprise since transients are really an exploit of Gaia's scanning of the whole sky.

light curve in log space. Generally the slope of the light curve in log space would correspond to

$$f'(x) = -A \tanh(B(C+x)) + D.$$

For example setting $A = 5/3$ would correspond to a curve which rises according to $t^{5/3}$ and decays according to $t^{-5/3}$; by shifting the curve vertically these exponents may be fine-tuned, allowing a $t^{-5/3}$ decay and a steeper rise. Integrating gives

$$\begin{aligned} f(x) &= \int (-A \tanh(B(C+x)) + D) dx \\ &= Dx - \frac{A \log(\cosh(B(C+x)))}{B} + E. \end{aligned}$$

The light curve in linear space is therefore

$$F(t) = e^{f(\log t)}. \quad (4.4)$$

B and D are free parameters; B determines how smooth the peak is and D determines how steep the initial rise will be. To achieve the $t^{-5/3}$, A is necessarily set to

$$A = D + 5/3.$$

C is used to defined the horizontal location of the peak and is given by

$$C = \frac{\tanh^{-1}(D/A)}{B} - \log t_{\text{peak}}.$$

E sets the brightness of the peak:

$$E = \log F_{\text{peak}}.$$

Applying these parameters to Eq. (4.4) gives, for example, Fig. 4.8. Here $t_{\text{peak}} = 20$ days and F_{peak} corresponds to a magnitude of 14. B and D were chosen to be 2 and 1 respectively; these parameters were iteratively refined so as to resemble the simulated light curve of Guillochon and Ramirez-Ruiz (2013) (so units are ignored). The dim part at the start of the curve has been added artificially to represent the star before disruption (disruption starts at $t = 0$).

Sampling

A general TDE light curve was defined over a period of 500 days. Figure 3.5b shows Gaia's projected coverage of the sky according to its nominal scanning law. From this, a typical low, medium and high frequency sampling was chosen as 50, 70 and 120 respectively. Over five years these correspond to average cadences of approximately 37, 26 and 15 days. For simplicity points were sampled with these set cadences, even though this will vary as the satellite attitude evolves with the scanning law, and observations will usually come in shortly spaced pairs as the second telescope sweeps around almost the same area in approximately two hours.

Three unique light curves were defined, based on their peak magnitudes, which were chosen as 14, 16 and 18 in G . From the *Open Tidal Disruption Event Catalog*⁸ (Guillochon, Parrent et al.

⁸tde.space

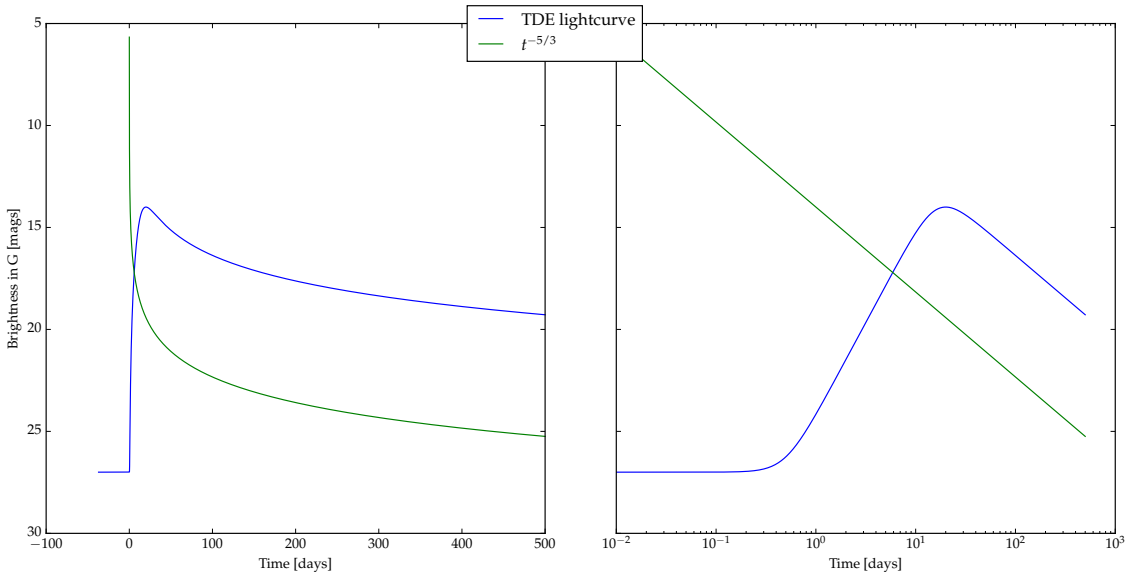


Figure 4.8: Synthetic TDE light curves in linear and log space exhibiting a power law rise, followed by a turn-around and a power law decay with index $-5/3$. A $t^{-5/3}$ curve is plotted for comparison.

2016), $G = 16$ and 18 can be seen as realistic peak magnitudes. $G = 14$ and 20 were considered as a third magnitude: At just above Gaia’s threshold, a 20th magnitude TDE would very quickly fade out of Gaia’s range so it would be fortunate to obtain one or two detections. At a high signal to noise it may also be difficult to distinguish it from the galaxy. A 14th magnitude source was favoured as a bright ‘edge case’, but if one occurs Gaia is more likely to spot it and observe for a longer period; it is therefore more likely that on-ground follow up will be achieved.

In preliminary simulations light curves were sampled *a priori* so as to reduce post-processing, but this was later disfavoured. Complete light curves (sampled in one day intervals) were simulated. These were sampled according to Gaia’s cadence *a posteriori* so as to avoid duplicate simulations and wasting computational time. This is discussed further in Section 4.5.3. This sampling emulates observing the light curve at a different phase as illustrated in Fig. 4.9. As there is a point of the lightcurve for every day, different samplings could be used to resemble different rise times if desired.

4.4.2 TDE simulation parameters

Harbouring galaxy

It is important to understand how the harbouring galaxy affects TDE detection; however, to simulate galaxies as in Section 4.3, and then variable TDEs on top of all of them would require too much computational time. Instead, galaxy radius and brightness were varied, and all other parameters were kept constant. Elliptical galaxies were used, setting B/T to 1 and disk parameters to 0. The other parameters were fixed as elliptical averages as described in Section 4.3.2.

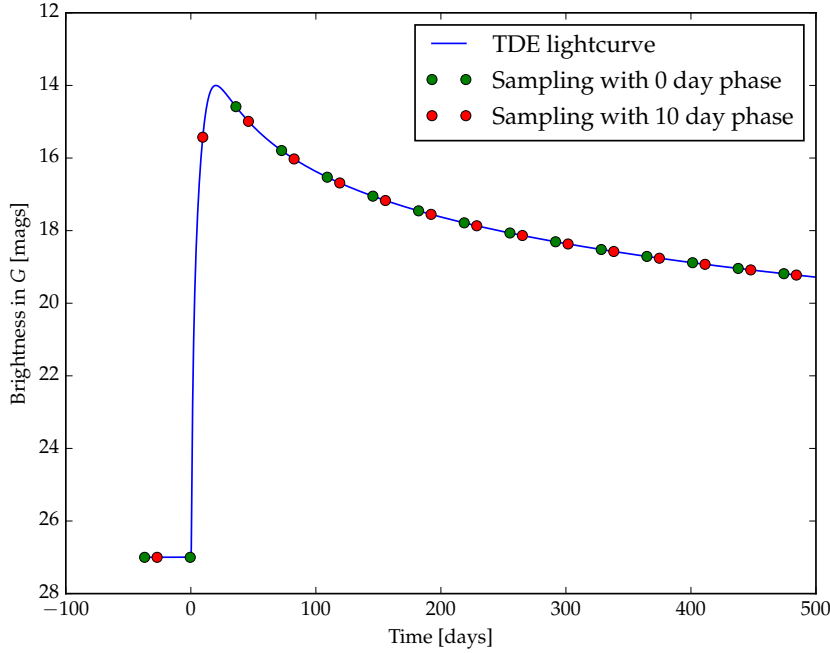


Figure 4.9: Lightcurve sampling for TDE with peak magnitude of 14. This sampling is according to a cadence of 37 days and is plotted for 0 and 10 day phases with no limiting magnitude.

Positions were chosen in a similar fashion to the galaxy simulations. Galaxy radii were varied as in the first part. Galaxy brightnesses were simulated as 16, 18 and 20. This was done to better match TDE brightnesses used, described in Section 4.4.1; this provides a spread of galaxies which are dimmer, fainter and of comparable magnitude to the TDEs (with the majority being dimmer as this is the ideal case).

TDE

Each lightcurve snapshot was defined as a separate object input to GIBIS, and each snapshot of the same lightcurve was placed on top of a constant galaxy at its centre. The input files therefore alternate between TDEs and galaxies, each pair having the same coordinates. There are nine types of galaxies which remain constant for each group of TDEs. In each group, the TDE brightness is the only parameter to vary, with the magnitude value coming from the TDE peak brightness and time.

Positions were allocated in the same way as the first part, except that each position contained two objects (the TDE and harbouring galaxy). The TDE was defined for GIBIS as a custom point source. This source requires a G magnitude and a spectrum (between 300 and 1100 nm). The spectrum is used purely for BP, RP and RVS simulations and is thus inconsequential for this work; however, a sensible spectrum of a 20 000 K blackbody was employed.

4.5 Performance of simulator

4.5.1 Simulation outputs

For each simulation run, GIBIS outputs a directory which contains generated images (FITS files, e.g. Fig. 4.10) and source detection information. Most of the detection information is found in a `gibis_information.txt` file (Babusiaux et al. 2015). This file contains a dump of the VPA processing data. Although the *StripmapVisualization* tool usefully combines the VPA output with the images and draws detection windows (among other background processes such as charge injection) allowing users to visualise the Gaia detection process, it does not provide a facility to ‘batch interact’ with the data. The brightness of the sources dictates that either a 12×18 pixel window or a 12×12 pixel window be used. These windows are shown in Fig. 4.11.

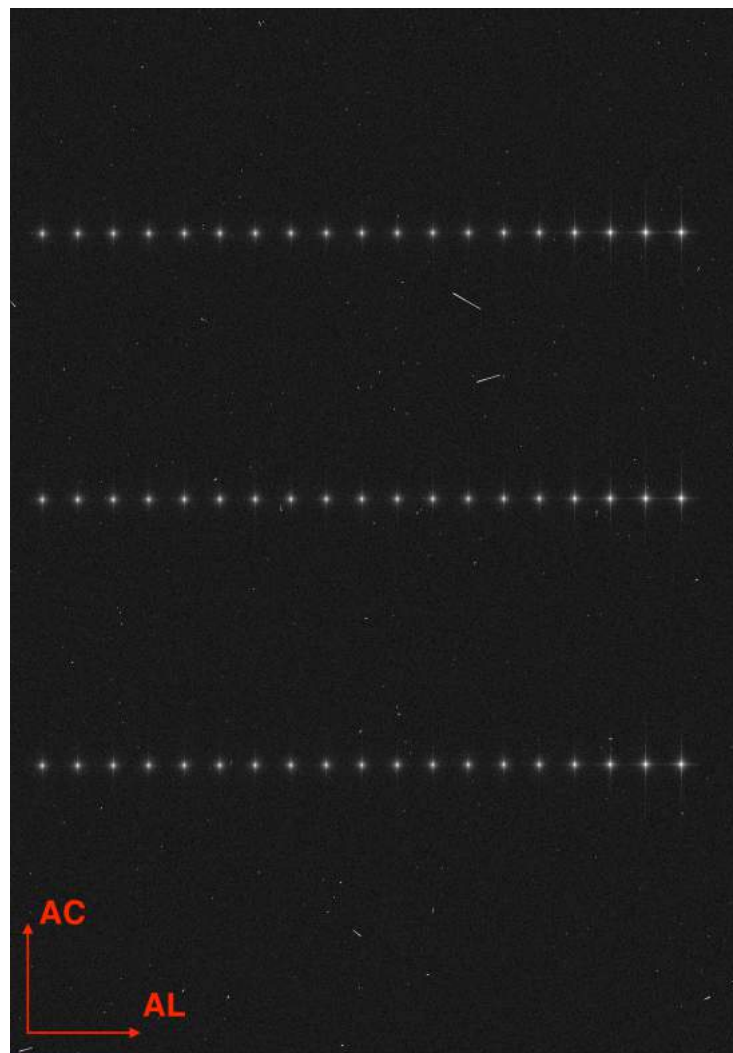


Figure 4.10: Sample output image from GIBIS with axes superimposed. The sources were laid out in a grid to reduce computation time. Some background and spurious sources can be seen.

As the `gibis_instrument.txt` file is very complicated, a parsing toolkit was developed to allow users to extract physical parameters. This toolkit was developed by Diana Harrison, and was obtained through DPAC. It provides input coordinates (right ascension and declination)

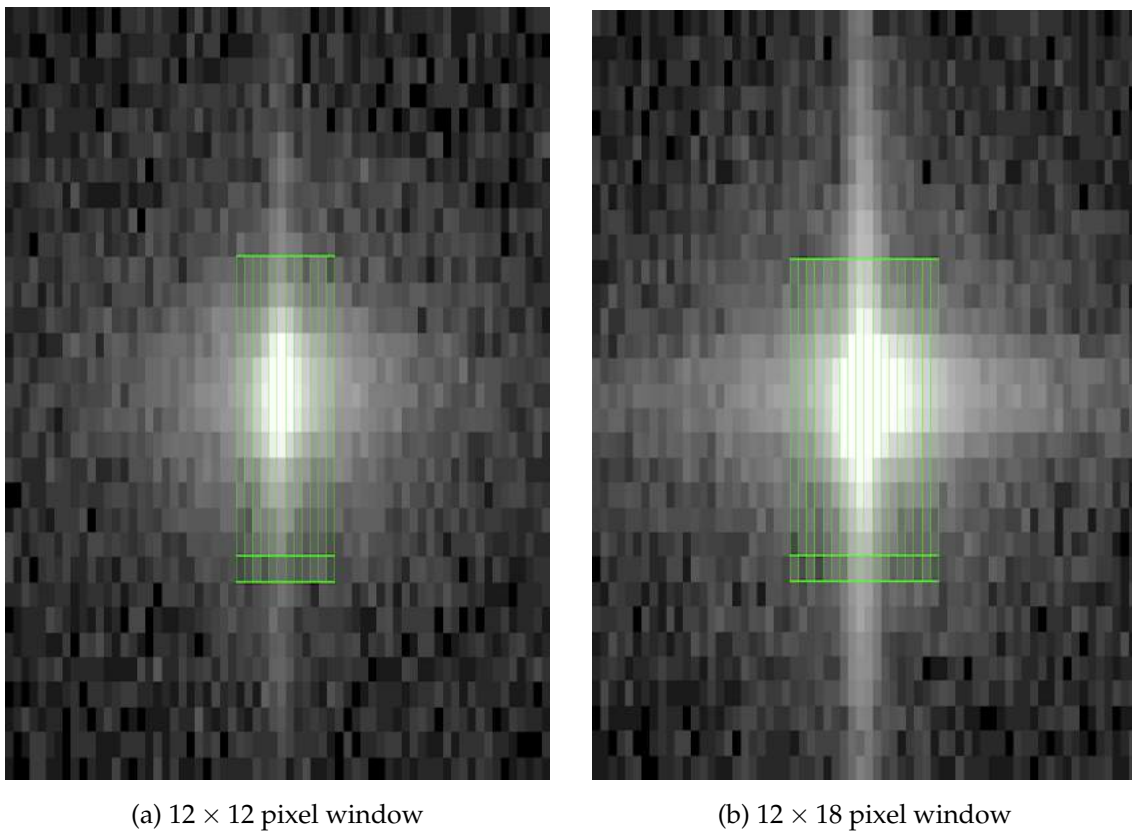


Figure 4.11: Two detection windows used to detect sources in this work overlayed on sources. 12×18 px windows are used for sources brighter than 16th magnitude, and 12×12 px windows are used for dimmer sources down to 20.7th magnitude.

and a G magnitude for every source (particularly useful for galaxies whose brightnesses are specified with a V magnitude) and an output G magnitude and astrometry data per detected source. These data were written to comma separated value (CSV) files, which are easily interpreted using common numerical frameworks.

4.5.2 Preliminary simulations

Due to the complexity of the simulator, test simulations were performed iteratively in order to gain a better understanding of its operation. The first large scale simulation was run with sources placed on a 50×50 px grid. As this spacing satisfies the 35 px spacing which Gaia employs (see Section 4.3.2), it was not anticipated that there would be any problems regarding the spacing of the sources. Given that the majority of the simulation parameters favoured detection, a large majority of the sources (or source pairs in the case of the TDE simulations) were expected to be detected. 31% of the TDE source pairs were detected, significantly lower than expected.

On investigation of the output images using GIBIS’s *StripmapVisualization* tool, it was clear that many sources which should have been detected were not. Also present was a strange detection efficiency periodicity, which most noticeably caused a rise in detection efficiency at the end of many of the light curves. Figure 4.12 shows one of the light curves; as the brightness drops off so does the detection efficiency, as one would expect (though the drop off is larger than expected), but the efficiency appears to increase at the end of the light curve indicating that Gaia is better able to detect some dimmer sources than brighter, which does not have a physical basis.

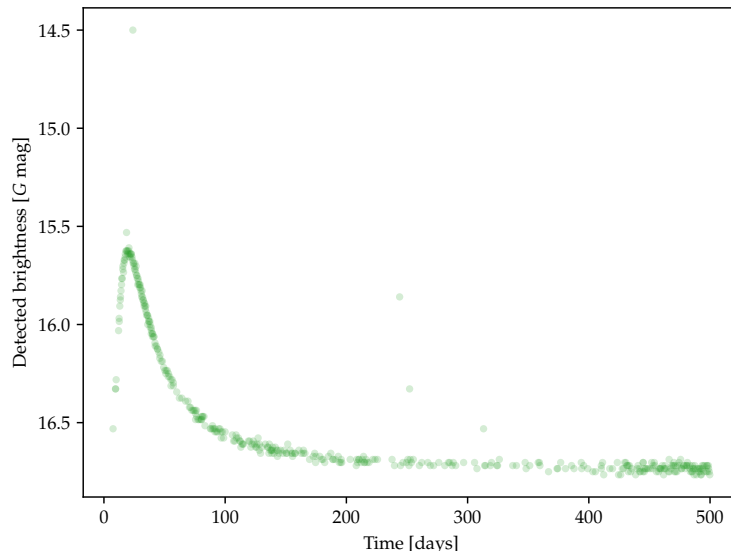


Figure 4.12: Typical light curve output from preliminary simulations showing a higher detection rate at the end of the light curve and thus lower brightnesses. This is physically unfounded and suggests a problem with the simulations.

A detection bias was seen in the ζ (AC) coordinate whereby lower ζ values were detected preferentially. This feature is not accounted for by a physical characteristic of Gaia and is illustrated in Fig. 4.13. It was considered that the brighter sources may have coincidentally been placed on this side of the CCD due to a periodicity in the light curve which matches the periodicity of the grid. The 2D histograms show that this is not the case as a drop off as ζ increases is seen in the detected sources and not in the simulated sources.

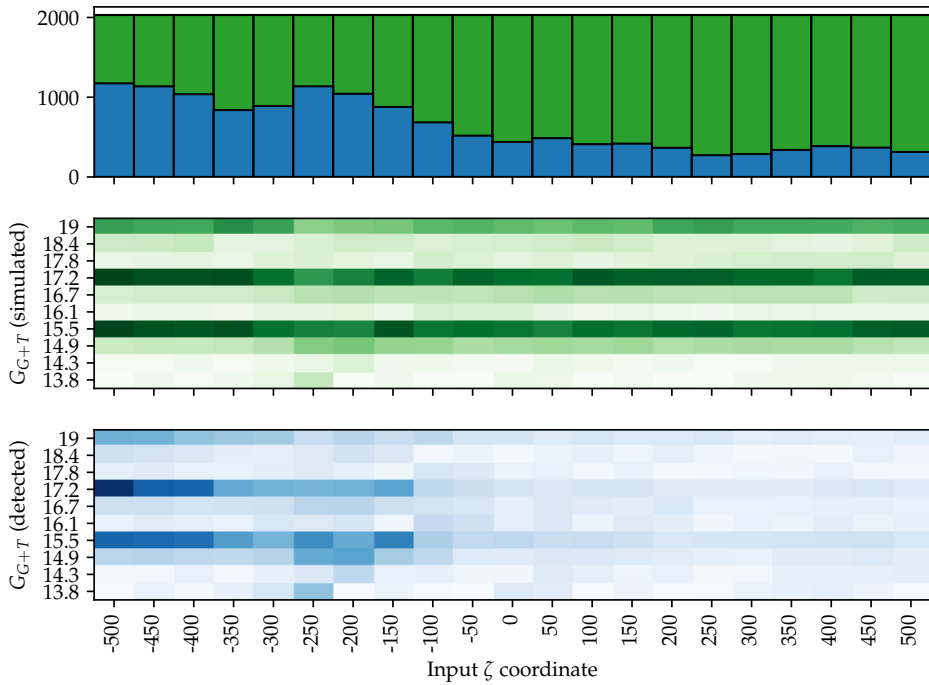


Figure 4.13: Histograms illustrating bias in ζ (AC) coordinate. Green represents the data which were simulated, while blue represents data which were detected (see last paragraph of Chapter 1 for data representation convention). The 2D histograms show that for each brightness, the input sources are spread isotropically distributed in ζ , whereas the detected sources are not, indicating that this bias is not due to the bright sources occurring on one side of the CCD. The G value here is the sum of the galaxy and TDE input G values.

It is posited that the VPA implementation utilised in GIBIS, although supplied by the manufacturer, has a lower resource limitation than Gaia. GIBIS's VPA scans across the CCD, and as it does, objects are allotted a certain amount of VPA resources. These are used up as more sources are detected. A lower resource limit implies that GIBIS is not able to handle an object density field as high as Gaia. This explains the low detection efficiency and positional bias in detection. It is not clear whether this is a bug in GIBIS or the VPA implementation, a computer hardware dependent feature, or whether the VPA implementation was produced before VPA characteristics were finalised.

In order to determine the optimal source spacing to achieve realistic Gaia detection, more test simulations were performed. The issue was deemed to be binary in that no source degradation (in brightness or other parameters) was occurring; it was merely a case of (for a bright enough source) the source being detected or not. In order to determine the optimal source spacing, a

sample was run through GIBIS in various spacing arrangements which should have a virtually 100% detection efficiency. Table 4.1 shows the detection efficiency at various input spacing arrangements.

rows \ spacing	50 px	100 px	200 px
1		97% (36/37*)	100% (19/19*)
3	96% (181/189)	99% (110/111*)	
5		98% (181/185*)	
9	61% (116/189)		77% (255/333*)
21	28% (53/189)		

Table 4.1: Detection efficiency for various spacing arrangements. It can be seen to rise as the number of rows decreases and the source spacing increases. * indicates maximum sources per simulation file. 21×21 was the preliminary spacing, and 28% is the efficiency for one simulation with 189 source as opposed to 31% mentioned in the main text which is the efficiency for all simulations. Note that these efficiencies are of sources which should have a 100% efficiency and so indicate the efficiency of the simulation itself.

4.5.3 Final simulations

From Table 4.1, a grid of 3×19 (57) sources was chosen as optimal; three columns was observed to fall below the VPA resource limitation and a 200 px spacing ensured little to no extended source overlap. This new spacing decreased the number of sources per simulation by approximately 7.74 times. As this change significantly increased the total number of simulations to be performed, duplicate TDE simulations (which were originally included) were removed, and light curves would have to be constructed *a posteriori*. This does not affect the statistical results pertaining to individual observed light curves as each light curve is considered separately, so duplicate observations provide no statistical refinement. Some statistics are lost in considering the whole sample. Galaxy simulation parameters were unchanged apart from the input spacing.

Remaining detection bias

Figure 4.14 shows the coordinate bias present in the final simulations. It is clear that the bias has not been eliminated completely but has been reduced to a level which does not affect the overall results. Somewhat strangely it can be seen that the bias is now on the opposite side of the CCD. In assuming that the $\zeta = 500$ is at the correct detection level, the bias leads to a 2% drop in efficiency for ellipticals and spirals and a 1% drop for TDEs (primarily concentrated at $\zeta = -500$).

Overall this effect is very small, but in the case of the galaxies, this 2% discrepancy is concentrated $V = 15$, $R = 2''$ and $R = 5''$, and must be taken into account for these simulations.

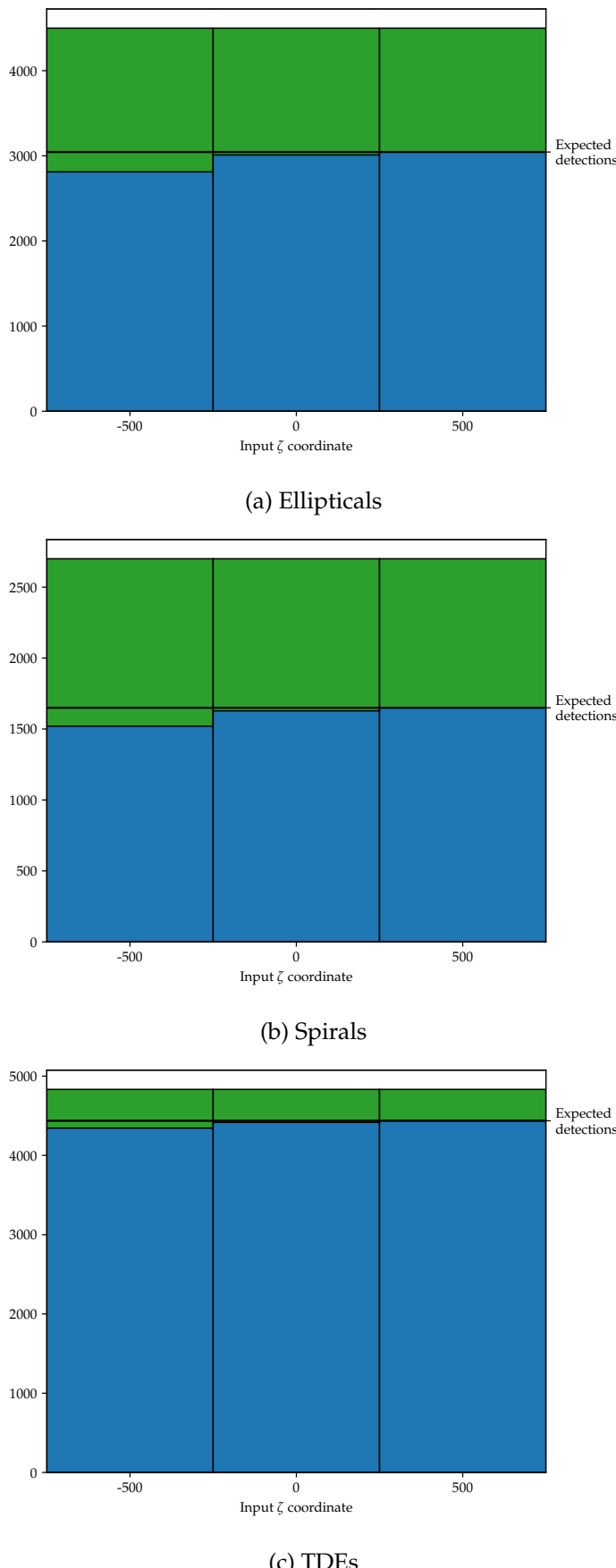


Figure 4.14: Detection bias across coordinates in all three final simulations. A small bias can still be seen. This caused a 2% drop in efficiency for the galaxies and a 0.7% drop in efficiency for the TDE.

Figure 4.15 shows this effect for ellipticals. $R = 2''$ shows losses of 10% and $R = 5''$ shows losses of 2%. The 100% efficiency at $\zeta = 0$ indicates that this effect is only a bias and does not cause a drop in detection efficiency across all ζ values.

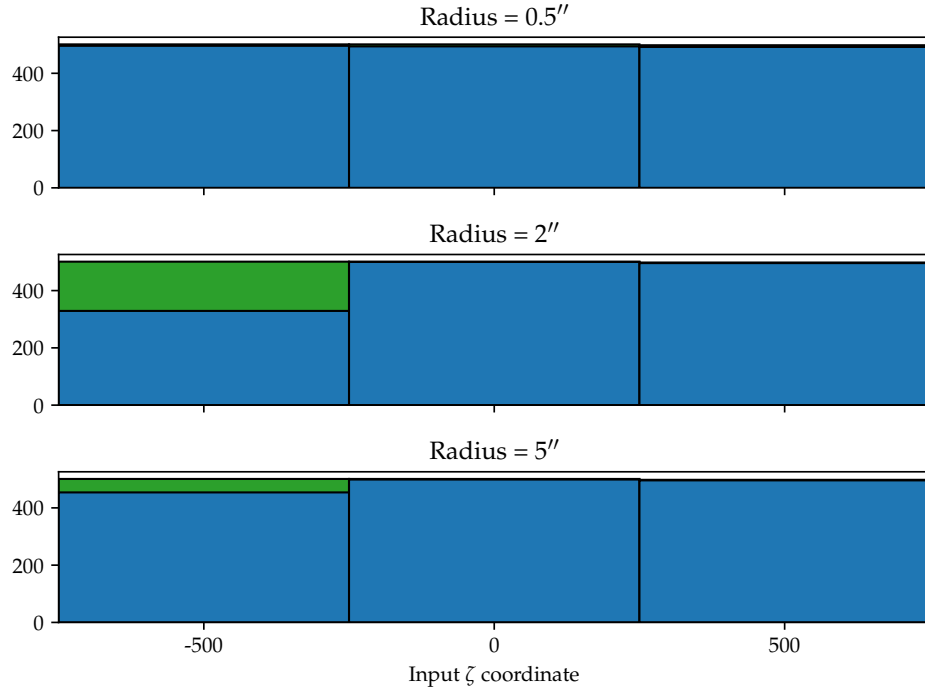


Figure 4.15: Detection bias in ellipticals with $V = 15$. The detection bias was found to be concentrated in the brighter galaxies.

Output parsing

It was also noticed that the VPA was incorrectly rejecting some sources in the AF1 CCD. This rejection phase exists so that cosmic rays and other spurious sources which may be detected in the SM will not be read out along the AF, so any astrophysical source which is bright enough to be detected in the SM should also be detected in AF1. However, a small number of the simulated sources were found to be detected in the SM and incorrectly rejected in AF1.

The GIBIS outputs are parsed using Interactive Data Language (IDL) scripts developed within DPAC. These scripts, however, only read out data from user-defined sources (thus ignoring spurious sources other than those which occur on top of a user-defined source), but appear to include AF1 rejections. Rejected spurious detections are still not read out because they are not user-defined but rejected user-defined sources are read out. This was presumably done to negate this AF1 rejection issue. This effectively emulates Gaia's detection process while cutting spurious detections out all together. The only spurious detections which are detected by the process are those which occur directly on top of a user-defined source, however, these would also be detected within Gaia.

Summary

Due to the lack of transient data in the Gaia archive for several years, TDEs are simulated using DPAC simulation tools, particularly GIBIS. This is an extensive Java application which is run through a command line interface. Simulations are defined with just galaxies and galaxy-TDE pairs, the parameters of which are motivated in detail. TDE light curves are simulated in daily intervals to be sampled according to Gaia's cadence in post-processing. Although some issues were encountered with the simulator, these were mitigated and little effect is anticipated in the results.

Chapter 5

Results

The results of the investigation are presented and discussed in the following chapter. Elliptical and spiral galaxy simulations are presented first; efficiencies are derived for a variety of galaxy types, providing a relation between each galaxy parameter and Gaia detection efficiency. Also investigated is the variation of Gaia’s response with each parameter. A relation is derived relating galaxy V magnitude to detected Gaia G magnitude for each galaxy type, which will be used in the TDE results.

Similarly, the detection efficiency and Gaia’s response is investigated for galaxy-TDE pairs. Light curves which were simulated are reconstructed in their original 1 day sampling to provide an overview as to how Gaia responds to these light curves, and were then sampled with three typical Gaia cadences show how a realistic TDE light curve will appear. A small correction was applied to detection efficiencies as per Section 4.5.3 to account for simulator detection bias. An overall adjusted efficiency of 68% was observed for ellipticals, 61% was observed for spirals and 91% was observed for TDE-galaxy pairs.

In an effort to illustrate how one might look for a TDE in the Gaia archive, a $-5/3$ index power-law fit is performed and compared with two other simple fits. In the same way an arbitrary power law was also fit to the light curves to illustrate how accurately Gaia returns the $-5/3$ index. Both these exercises return positive results for TDEs with peak brightnesses above 18th magnitude. Overall the results were positive with a median index of -1.66 for the arbitrary power law.

5.1 Galaxies

As part of the investigation into galaxy detection with Gaia, 379 simulations comprising 21 600 galaxies were run in total, divided into ellipticals and spirals. These simulations generated GIBIS’s usual output images and text files, and are discussed in the following sections.

5.1.1 Ellipticals

Detection efficiency

13 500 elliptical galaxies were simulated in GIBIS and were detected with a total efficiency of 66%. Applying a correction to account for coordinate bias illustrated in Fig. 4.14, gives a total efficiency of 68%. This 2% discrepancy is small but is concentrated in a subset of galaxy types and so plays a bigger role for them.

The key parameters affecting galaxy detection are brightness and radius. Figure 5.1 shows how detection varies with input radius and V magnitude. Each tile of this 2D histogram encompasses 1500 simulations, of which the number detected is represented by a shade of blue. The minimum detection efficiency is found in the top right of the plot and the maximum in the bottom left, and a gradient can be seen joining them. $V = 21$ corresponds to approximately $G = 20.6$ so at $R = 0.5''$ there is just enough light for approximately half to be detected. Likewise, $V = 18$ corresponds to approximately $G = 17.6$, which is well above the detection threshold; however at $R = 5''$ much of this light falls outside the detection window at the efficiency is lowered significantly.

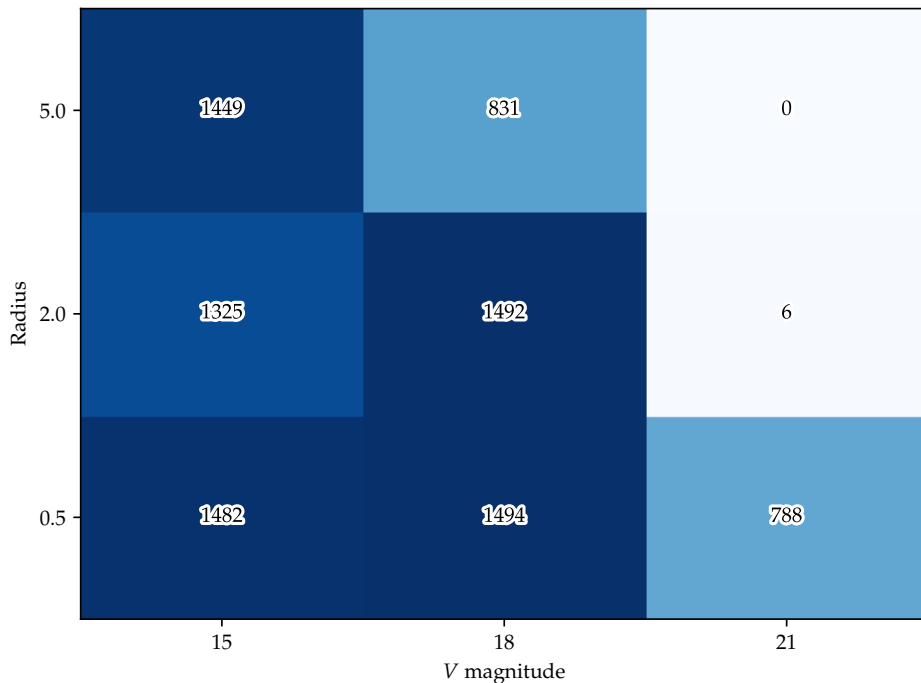


Figure 5.1: Detections for input galaxy effective radius vs V magnitude. The detection efficiency in general rises with increasing brightness and decreasing radius. Each tile consisted of 1500 simulations.

Approximately all galaxies are expected to be detected at $V = 15$ and $V = 18$ for $R = [0.5'', 2'']$, so in particular, the numbers for $V = 15$, $R = 2''$ appear somewhat low. This reduced value may be roughly accounted for by the coordinate bias present in the simulator, specifically Fig. 4.15. As described in Section 4.5.3, there was a bias present in the simulator where high ζ values are detected with a higher efficiency than lower values; this effect was quite small in the

broad view of the simulations but was concentrated in the $V = 15$ parameter. By including the missing $\zeta = -500$ detections 1325 is adjusted to 1476.

Figure 5.2 shows a comparison between the detection efficiency attained in the above simulations and that from de Souza et al. (2014). Both studies contained similar galaxy types simulated in GIBIS. The coordinate bias has been corrected and a Gaussian interpolation has been applied to the data. The scales and resolution of the plots are quite different but they can be seen to compare quite well. The sharp cut-off seen in Fig. 5.2b would likely be seen here with a finer V and R resolution.

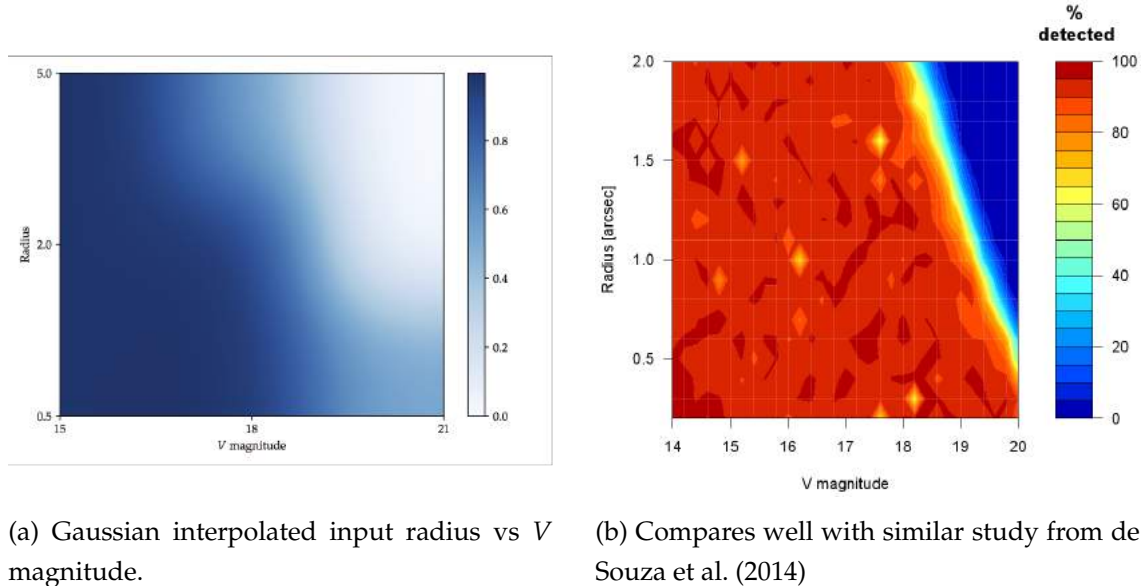


Figure 5.2: Comparison of elliptical detection efficiency in this work and de Souza et al. (2014). The plots are seen to compare well with a lack of detections at dim, large galaxies rising to an abundance of detections for bright, small galaxies. Note difference in axis scales.

Figure 5.3 is a histogram matrix comparing all influential input parameters. The 2D histograms compare detection efficiency for each pair of parameters while the 1D histograms on the diagonal display the detected number of each parameter against the simulated number. Detection is favoured in low b/a values; i.e. circular E0 galaxies are less likely to be detected than elliptical E7s. Colour index has no strong effect on detection efficiency.

Due to the rectangular size of the detection window, one would expect that for more elliptical (E7) galaxies, the position angle will affect the detection efficiency due to more or less of the galaxy falling into the window. The maximum efficiency position angle will depend on the size of the window (and thus the brightness of the galaxy) but every galaxy should have a minimum at $\theta = 0^\circ, 180^\circ$ and 360° . This is roughly observed to be the case, as shown in Fig. 5.4. In order to better constrain this conjecture, observations would be better made closer to the detection limit (where the rate drops off quicker). This demonstrates the effect of the angle at which Gaia scans across a source.

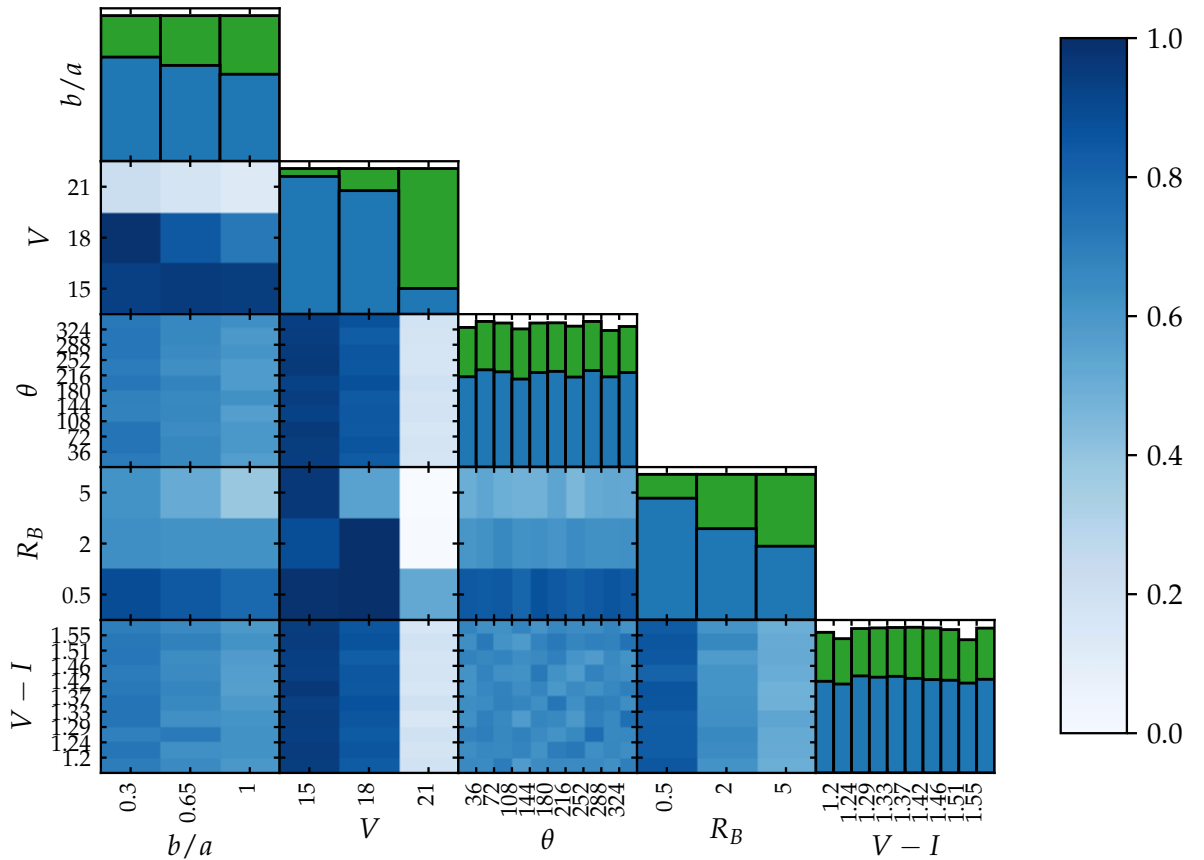


Figure 5.3: Detection efficiency for several input parameters in ellipticals. The 2D histograms represent the detection efficiency for each pair of parameters. The 1D histograms on the diagonal represent the detected data overlaid on the simulated data. The colour bar thus only applies to the 2D histograms. V has the largest effect with most $V = 21$ galaxies falling below Gaia's detection threshold. R has the effect that more light falls outside Gaia's detection window with larger values and so reduces the efficiency. b/a has a small effect where circular galaxies are less likely to be detected.

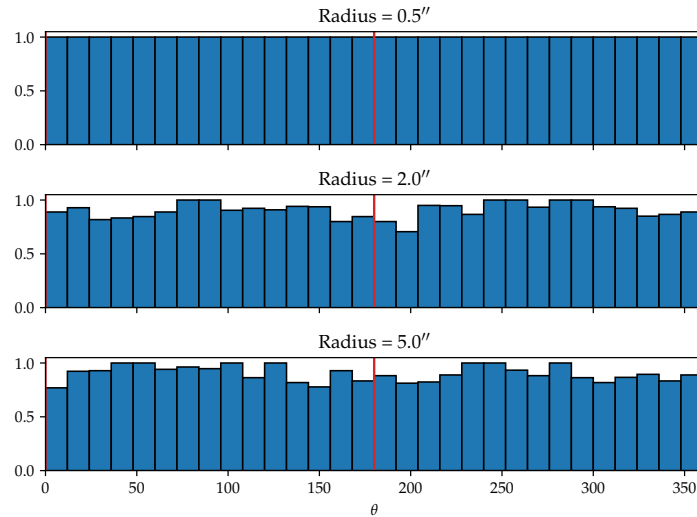
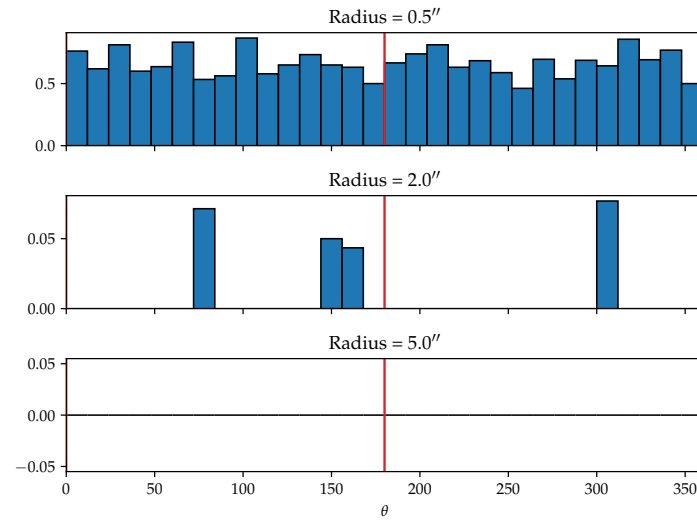
(a) Detection efficiency across θ for $V = 15$ (b) Detection efficiency across θ for $V = 21$. Note that there were little and no detections for $R = 2''$ and $R = 5''$.

Figure 5.4: Detection efficiency histogram across the full range of θ values for E7 galaxies. As these galaxies are elongated, it is anticipated that the position angle will cause more or less light to fall inside the rectangular detection window. This effect is small but observed. Expected minima are marked with red vertical lines.

Detected brightness

Figure 5.5 shows the raw source and found G magnitudes for the simulated elliptical galaxies. The source or intrinsic G magnitude is a straight conversion from the galaxy input filter data and does not take account of the other galaxy features which may affect the detection magnitude, whereas the found G magnitude is that which Gaia will detect and is based on the galaxy brightness, its other intrinsic parameters which affect detection (e.g. radius) and Gaia's detection process. This plot does not provide much insight into how a galaxy is detected, other than the fact that there is a spread, indicating that the detected brightness is affected by the input parameters. These detection brightnesses are broken down by parameter in Fig. 5.6 where a clear relationship emerges. It can be seen that there is a downward shift between the source brightness and the detected brightness. This shift is considerably affected by the galaxy radius and subtly affected by the galaxy ellipticity.

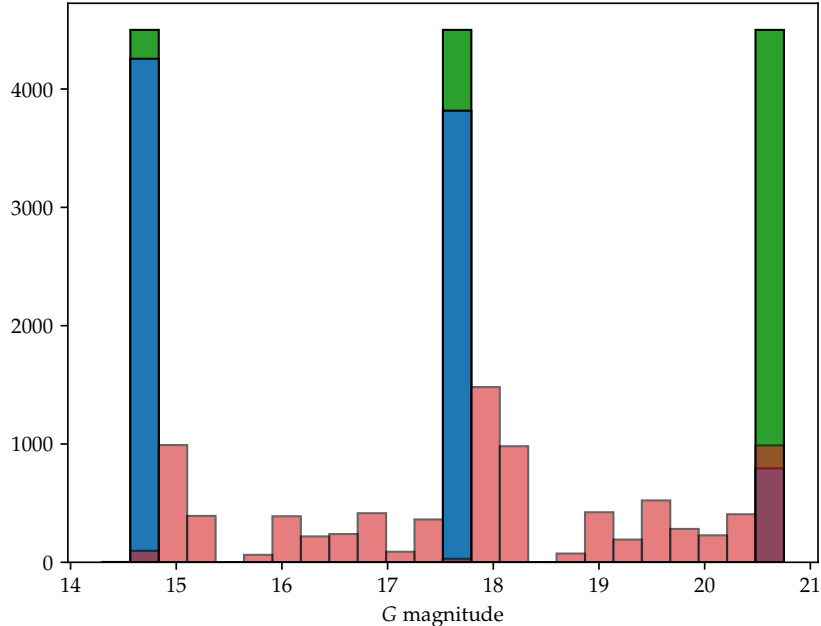


Figure 5.5: Histograms of intrinsic G magnitude (simulated in green, detected in blue) and detected G magnitude (transparent red). The green and blue histograms represent the simulated V data converted to a G magnitude, while the red histogram represents the detected G magnitude when accounting for the fact that part of the galaxy will fall outside the detection window; the total bin values of the red bins therefore will add up to the blue bin values. The detected values are quite spread out so it is difficult to see a pattern.

The smaller the radius and the ellipticity of the galaxy are, the closer the detected brightness gets to the source brightness. This is in agreement with Fig. 5.3 and the fact that more sources are detected with lower ellipticity; the shift in the measured magnitude may take it past the detection limit. The shift from the radius decreases with decreasing radius, but also visible is the fact that the difference in b/a shifts gets smaller with decreasing radius indicating the ellipticity plays a smaller role as the size of the source decreases.

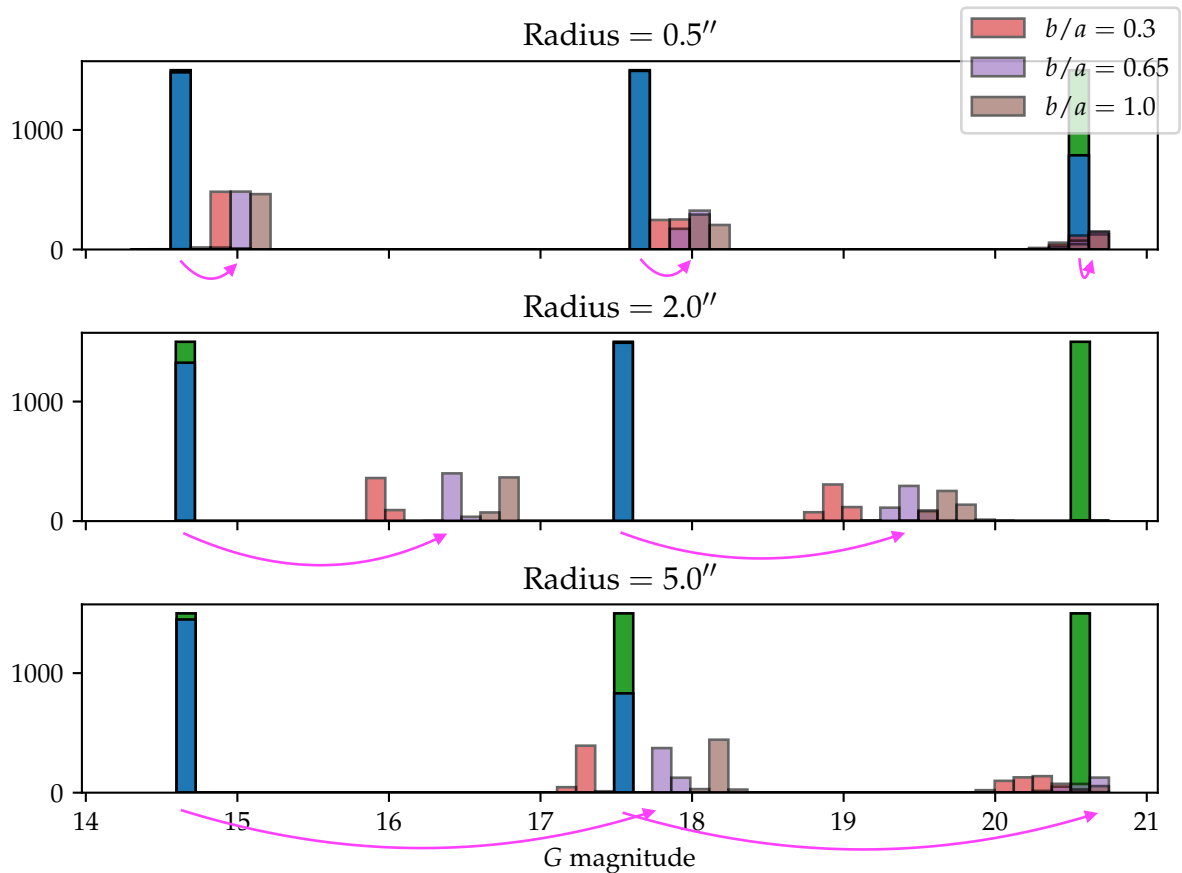


Figure 5.6: Histograms of intrinsic G magnitude (simulated in green, detected in blue) and detected G magnitude separated by radius and ellipticity (labelled). Now a clear pattern can be seen in detected magnitude groups, so a relation between intrinsic and detected magnitude can be derived per galaxy. Arrows illustrate the magnitude shift due to the detection window size; the coloured bins add up to the blue bin. Note that the detection deficiency for $R = 2''$, $G \approx 14.7$ is due to the coordinate bias described previously.

These simulations may be used to infer a relationship between galaxy parameters and Gaia detection brightnesses which may be used for galaxy subtraction in detection of other extragalactic sources. This is discussed further in the following section.

Galaxy modelling

If one wishes to perform extragalactic photometry with Gaia, it is imperative to be able to model galaxy brightness. When observing objects such as TDEs, it is critical to know how much light is coming from the TDE and how much from the galaxy. If the galaxy is not observed on its own with Gaia, it may be necessary to rely on observations made with another observatory. However, in order to attain the Gaia observation G magnitude of the galaxy, it is necessary to account for the filter conversion (discussed in Jordi et al. 2010), as well as the amount of light which falls into the area of the detection window. Therefore an empirical relation between intrinsic parameters (brightness, radius and ellipticity) and the G magnitude observed by Gaia has been derived. In order to do this, a normal distribution was fit to the magnitude detected with GIBIS for each galaxy variant. An example of this fit is shown in Fig. 5.7.

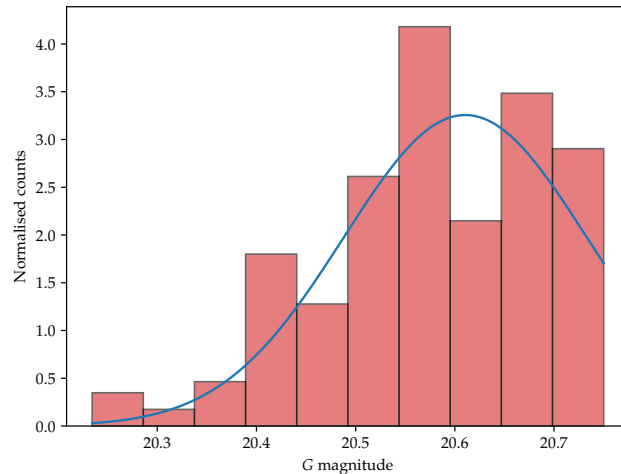


Figure 5.7: Example normal distribution fit to detected G magnitude data. This fit is for $R = 0.5$, $V = 21$ and $b/a = 0.3$. The edge of this particular Gaussian falls below Gaia's detection limit and is thus cut off, however a fit can still be made.

This relation is tabulated in Table 5.1. Several of the dim galaxy relations are missing due to their detection primarily falling below Gaia's detection threshold. With more simulations, however, it may be possible to determine these values by fitting a normal distribution to the edge of the sample. In this case the mean would fall below the detection threshold but the light reaching Gaia may still be estimated. These values appear to follow an approximately linear relationship so interpolation may provide a good estimate of the galaxy magnitude.

Using this approach one may derive a function which maps galaxy intrinsic parameters (in the space \mathbb{I}) to Gaia detected G magnitudes (in the space \mathbb{G}), i.e.

$$f : \mathbb{I} \rightarrow \mathbb{G}.$$

(a) Magnitude shifts for $R = 0.5''$			
b/a	15	18	21
0.3	14.86(2)	17.85(3)	20.6(1)
0.65	14.99(1)	17.99(3)	20.7(1)
1.0	15.13(4)	18.12(3)	-

(b) Magnitude shifts for $R = 2''$			
b/a	15	18	21
0.3	15.96(3)	18.94(7)	20.71(2)
0.65	16.45(2)	19.42(8)	-
1.0	16.75(2)	19.70(9)	-

(c) Magnitude shifts for $R = 5''$			
b/a	15	18	21
0.3	17.30(4)	20.2(2)	-
0.65	17.85(3)	20.6(1)	-
1.0	18.18(4)	20.67(8)	-

Table 5.1: Empirical relation between galaxy intrinsic parameters and G magnitude observed by Gaia. Values are magnitude shifts from V . Some shifts were indeterminable due to lack of detections.

This function is not injective and it is therefore not possible to map G to a set of intrinsic parameters or V . This has the implication that galaxies observed with Gaia may not be compared with galaxies observed with other instruments without some modelling which subtracts the galaxy light falling outside the window. Such a model might use pixel data or combine brightnesses measured at different scanning angles (e.g. Harrison 2011).

Elliptical galaxies: Summary

13 500 elliptical galaxies were simulated. A total detection efficiency of 66% was observed in these simulations; however, this included a 2% reduction due to a detection bias in the simulator whereby bright sources were detected with lower efficiencies on one side of the CCD. So the expected true efficiency was 68%. The two parameters which had the biggest effect on detection were V magnitude and effective radius. $V = 21$ corresponds to a Gaia G magnitude which falls just within the detection limit; however, at larger effective radii, enough of the galaxy's light falls outside Gaia's detection window that the observed G magnitude falls below the detection limit. Also seen is that there is a bias in Gaia towards higher ellipticity galaxies, with E7 galaxies having the highest detection rate. A small effect could be seen in position angle indicating that the angle at which Gaia scans a galaxy will have an affect.

Gaia's response to the intrinsic magnitudes was also investigated. A shift can be seen from all intrinsic brightnesses to detected brightnesses owing to the fact that galaxies are extended and a small fraction of the light will always fall outside the detection window, though for

$R = 0.5''$ this effect is quite small, with even many $V = 21$ galaxies being detected. This effect increases, however, to the point where no $V = 21$ galaxies are detected and the $V = 18$ efficiency is approximately halved. Also causing a magnitude shift is the ellipticity with less elliptical galaxies being detected at lower magnitudes. It was anticipated that the mean shift across b/a values would not be affected, but the variation would be broadened due to different position angles shifting the elongation along or across the Gaia scanning direction, but this was not observed. Using these shifts a Gaussian curve was fit to each response. These allow a relation between galaxy intrinsic parameters and Gaia detected parameters to be formed, which will be employed in the TDE part.

5.1.2 Spirals

Detection efficiency

8100 spiral galaxies were simulated in GIBIS and were detected with a total efficiency of 59%. Applying a correction to account for coordinate bias illustrated in Fig. 4.14, gives a total efficiency of 61%. Again, there is a 2% discrepancy which is small but is concentrated in a subset of galaxy types and so plays a bigger role for them.

Similar to the ellipticals, Fig. 5.8 shows a histogram matrix of all the influential input parameters. B/T is now included to account for its effect on the detection efficiency. The disk radius is included but not the bulge radius as it is just a constant times the disk radius and so all histograms would look the same. Similarly the disk ellipticity is not included since it is fixed at 1, and θ refers to the bulge and disk position angle since they are set equal.

The approximate shape of each of the parameters is the same as before since both represent observation of extended sources by a satellite which is optimised for detection of point sources. The main conclusion drawn from Fig. 5.8 is that Gaia will not see much by way of spiral disks. The spiral bulge will primarily be detected due to its more favourable profile (see Eqs. (4.1) and (4.2)). Therefore the more light that is concentrated in the bulge the higher the detection efficiency, hence the shape of the B/T histogram.

This also has a knock on effect for the rest of the parameters. The radius (scale length) of the galaxy has less of an effect as the size of the elliptical and spiral galaxies were chosen to be equal but the spiral bulge effective radius was set at 1/3 times the disk scale length. Because it is primarily the bulge which Gaia is sensitive to, it is these radii which must fall inside the detection window, and their sizes are such that most of their light does.

Similarly, $(b/a)_B$ has a lesser effect as despite a large ellipticity, most of the light from the spiral bulges simulated in this work will still fall in the detection window. A small variation can be seen for $(b/a)_B = 0.3$, where the galaxy is just elliptical enough that some of the light starts to fall outside the detection window and for dim galaxies this will impact their detection. The θ effect is lesser than before. Since most of the galaxy bulge fits in the detection window and the disk is circular (and faint), the position angle will not have a large affect. It is expected that θ would have a larger effect, similar to ellipticals, for larger bulges and thus

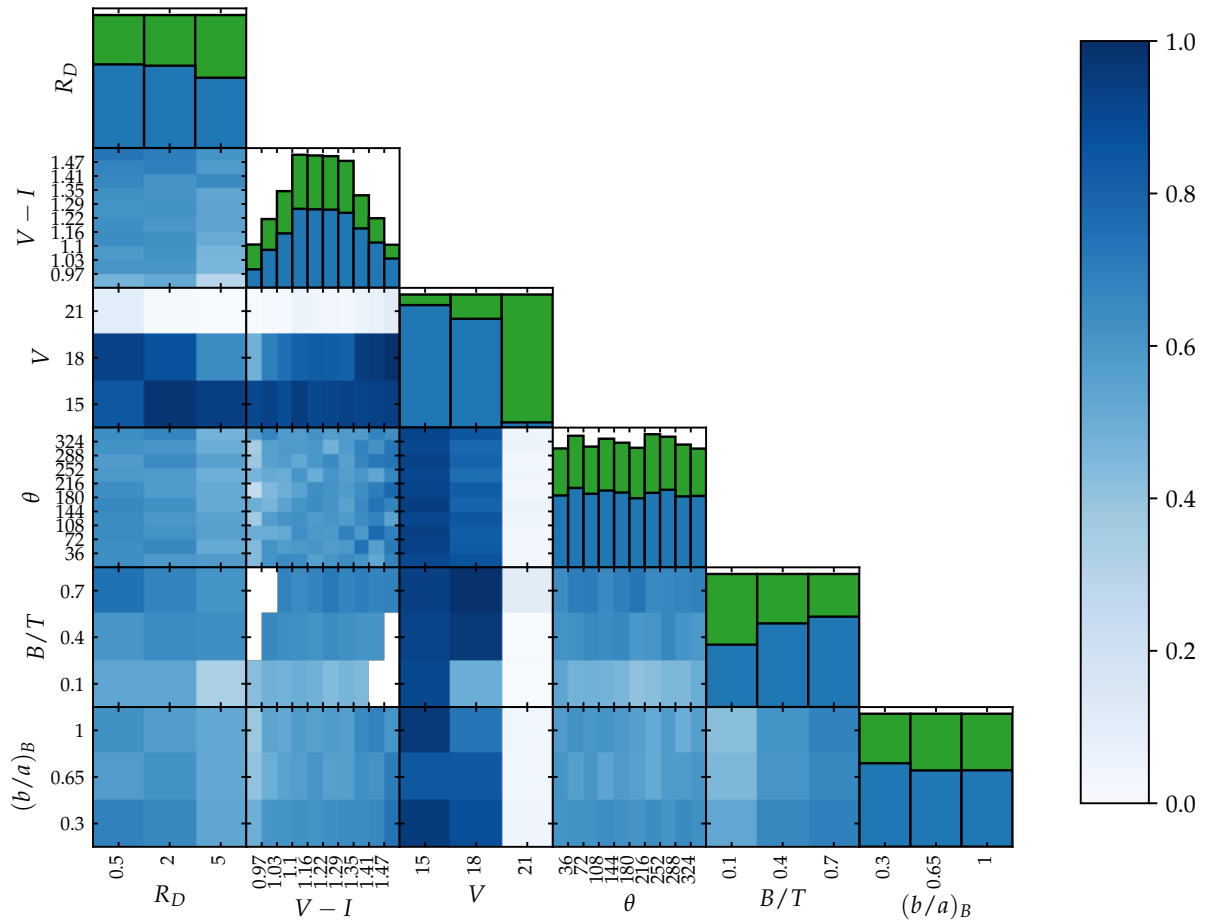


Figure 5.8: Detection efficiency for several input parameters in spirals. The 2D histograms represent the detection efficiency for each pair of parameters. The 1D histograms on the diagonal represent the detected data overlayed on the simulated data. The colour bar thus only applies to the 2D histograms. Not much by way of galaxy disks are detected. This manifests in the variation of several parameters: R_D has a smaller effect than the elliptical galaxy effective radius as the detection is really only of the bulge, and as the bulge effective radii are three times smaller than the disk scale length these mostly all fall well inside Gaia's detection window. For the same reason the ellipticity effect is reduced. The lack of detections at $V = 21$ is exaggerated as when any sort of substantial fraction of light is attributed to the disk instead of the bulge the galaxy is strongly affected. The bulge to total ratio highlights Gaia's potential for detection of the disk as when the ratio is reduced and more light is attributed to the disk instead of the bulge, the efficiency drops.

larger galaxies.

The effect on V magnitude detection is enhanced for the same reason. This brightness is set for the whole galaxy, including the bulge and the disk. $V = 21$ magnitude ellipticals were just about detected when the radius was very small and most of their light fell inside the detection window. With spirals, however, this light is also spread across the disk, which Gaia is not as sensitive to. If the bulge is the dominant feature of the galaxy, i.e. $B/T = 0.7$ then it may be just about possible to detect some spirals. Figure 5.9 illustrates this in a 2D histogram of B/T vs V .

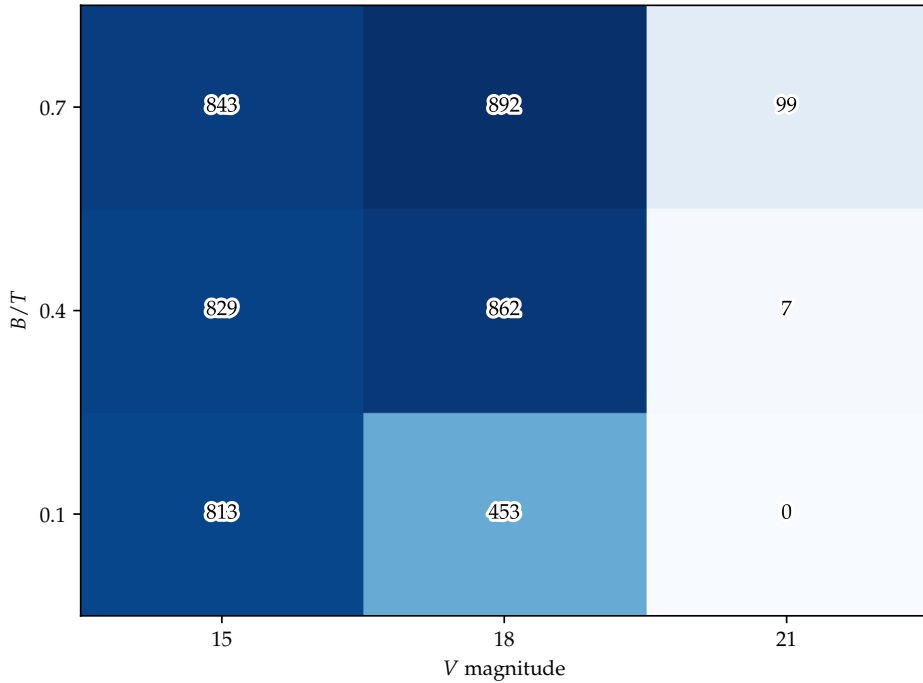


Figure 5.9: 2D histogram of detections with input B/T vs V for spirals. Again, efficiency is seen to reduce with larger brightnesses. Efficiency also increases with increasing bulge to total ratio. This indicates that Gaia is not very sensitive to galaxy disks and thus the higher the fraction of light in the bulge the higher the efficiency. All tiles represent 900 simulations.

Detected brightness

Figure 5.10 shows an overview of the source and detected brightnesses for spirals. The detected brightnesses are more evenly spread out suggesting a larger smearing effect. This is not surprising since there are more varying parameters in spirals. Figure 5.11 shows the measured magnitudes separated by bulge to total ratio and radius (not bulge ellipticity). It can be seen that the bulge to total ratio has a large impact on the detected magnitude. As discussed in the previous section, Gaia's sensitivity to spiral disks is poor so as a larger fraction of the total light is shifted to the disk, less is detected by Gaia.

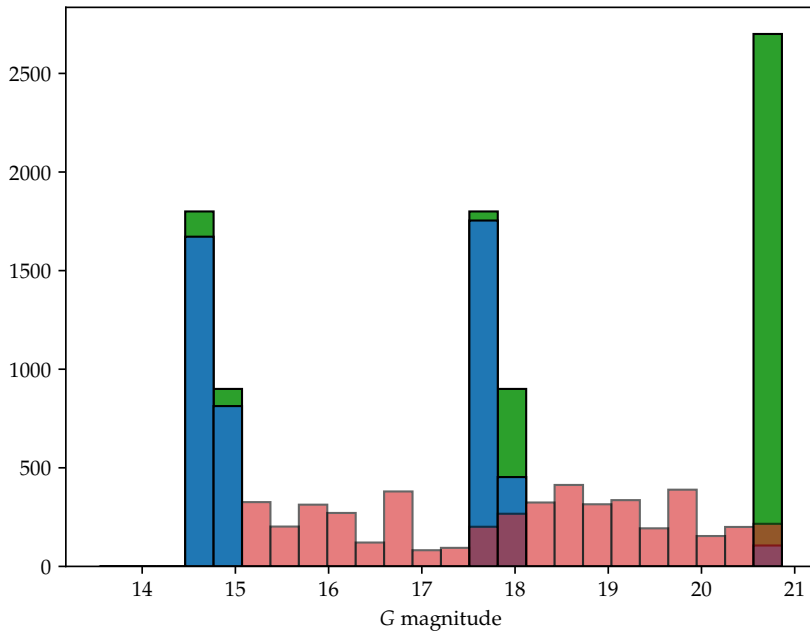


Figure 5.10: Histograms of source G magnitude (simulated in green, detected in blue) and detected G magnitude (transparent red).

Galaxy modelling

In the same way as ellipticals (see Section 5.1.1), normal distributions were fit to galaxy detected brightnesses in order to derive a relation between galaxy intrinsic brightness and observed G magnitude. A sample fit is shown in Fig. 5.12, and the data are tabulated in Table 5.3. There is an extra free parameter in the spiral simulations which results in nine tables instead of three.

Spiral galaxies: Summary

8100 spiral galaxies were simulated. A total detection efficiency of 59% was observed in these simulations; however, as before this included a 2% reduction due to a detection bias in the simulator whereby bright sources were detected with lower efficiencies on one side of the CCD. Gaia's response to galaxy disks was seen to be quite poor. Spirals with the same radius (scale length vs effective radius) and brightness as ellipticals were used with a lower overall detection efficiency. This is somewhat redeemed by the fact that if the galaxy bulge is bright it will be more likely to be detected as it is relatively much smaller compared to the overall size of the galaxy. If a large fraction of the overall light is attributed to the galaxy disk then the galaxy has a poor chance of being detected. Apart from this the same effects as ellipticals are expected. Effects on the bulge are reduced however due to its relatively smaller size in the detection window.

Gaia's response to the intrinsic magnitudes was also investigated. As before, a similar shift is observed for radius, brightness and ellipticity between intrinsic and detected brightnesses. A

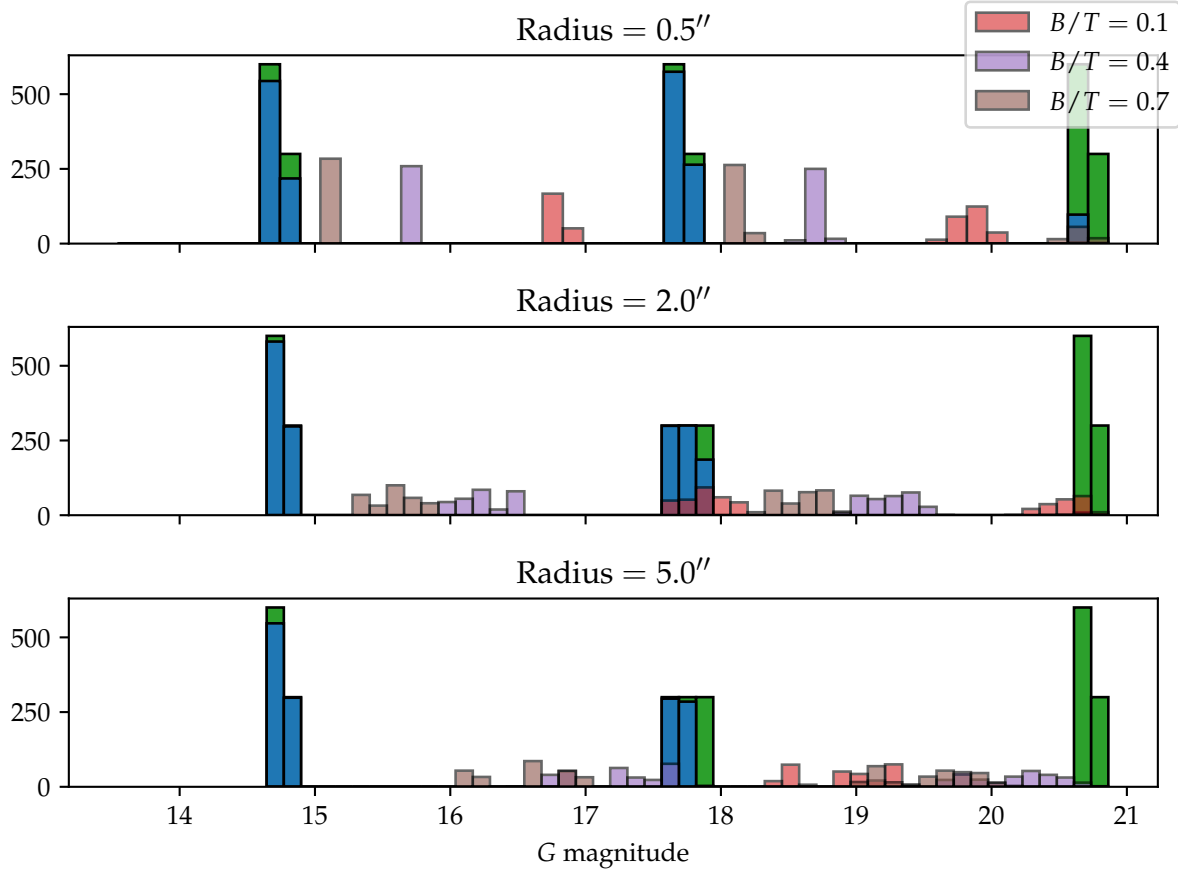


Figure 5.11: Histograms of source G magnitude (simulated in green, detected in blue) and detected G magnitude separated by radius and bulge to total ratio (labelled). The groups of detected G magnitudes still contain all values of bulge ellipticity, and despite the fact that it is reduced, it still causes a wider spread.

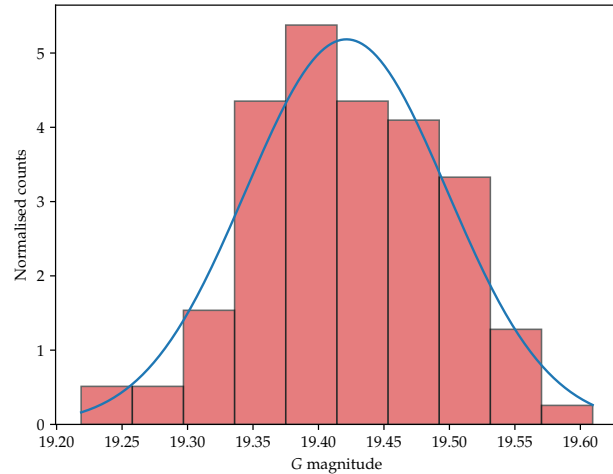


Figure 5.12: Example normal distribution fit to detected magnitude data. This fit is for $R_D = 2$, $V = 18$, $(b/a)_B = 1$ and $B/T = 0.4$.

(a) Magnitude shifts for $R_D = 0.5, V = 15$			
	0.3	0.65	1
0.1	16.81(3)	16.82(2)	16.83(3)
0.4	15.69(2)	15.70(1)	15.72(2)
0.7	15.13(2)	15.13(4)	15.15(2)

(b) Magnitude shifts for $R_D = 0.5, V = 18$			
	0.3	0.65	1
0.1	19.8(1)	19.9(1)	19.9(1)
0.4	18.70(5)	18.71(4)	18.71(5)
0.7	18.13(3)	18.14(3)	18.15(4)

(c) Magnitude shifts for $R_D = 0.5, V = 21$			
	0.3	0.65	1
0.1	-	-	-
0.4	20.75(1)	-	20.67(2)
0.7	20.67(7)	20.73(5)	20.69(8)

(d) Magnitude shifts for $R_D = 2, V = 15$			
	0.3	0.65	1
0.1	17.71(3)	17.90(2)	18.06(4)
0.4	16.04(3)	16.27(2)	16.44(2)
0.7	15.39(2)	15.61(2)	15.79(2)

(e) Magnitude shifts for $R_D = 2, V = 18$			
	0.3	0.65	1
0.1	20.5(2)	20.7(1)	20.66(8)
0.4	19.03(7)	19.24(8)	19.42(8)
0.7	18.39(5)	18.60(5)	18.77(5)

(f) Magnitude shifts for $R_D = 2, V = 21$			
	0.3	0.65	1
0.1	-	-	-
0.4	-	-	-
0.7	20.72(5)	-	-

(g) Magnitude shifts for $R_D = 5, V = 15$			
	0.3	0.65	1
0.1	18.49(6)	18.96(6)	19.28(5)
0.4	16.81(3)	17.29(3)	17.59(3)
0.7	16.15(4)	16.62(3)	16.94(3)

(h) Magnitude shifts for $R_D = 5, V = 18$			
	0.3	0.65	1
0.1	20.66(2)	-	-
0.4	19.79(9)	20.2(1)	20.5(2)
0.7	19.14(7)	19.61(8)	19.87(9)

Table 5.3: Empirical relation between spiral intrinsic parameters and G magnitude observed by Gaia. Some shifts were indeterminable due to lack of detections. No shifts were derived for $R_D = 5, V = 21$.

significant shift is also seen due to the bulge to total ratio. The disks are more diffuse and so a smaller bulge to total ratios give a smaller shift in detected brightness. As with the ellipticals, a Gaussian curve was fit to each response to calculate the mean shift in the brightness due to each parameter.

5.2 TDEs

5.2.1 Galaxy modelling

As mentioned in Section 5.1.1, in order to quantify the amount light which is being detected from a TDE or other extragalactic source, the light from the galaxy must be accounted for. There are several ways to do this: The simplest way is to assume it is negligible and ignore it. This is a reasonable assumption if the galaxy is at or near the detection limit and the TDE is bright. If for example, one observed a TDE of magnitude 16 atop a galaxy which is just below the detection limit (21st magnitude), the TDE will be approximately 98 times brighter. This means that the galaxy will only contribute to 1% of the total light collected by Gaia, which may be a reasonable compromise.

Arguably the best way to account for the galaxy is to use observations made of the galaxy on its own, either before the source flares or after it has subsided. This method does not rely on any modelling or outside knowledge of the galaxy and merely requires a simple (magnitude) subtraction, but is not always possible, perhaps due to the galaxy being dimmer than Gaia's detection limit. Another reason a source may not be observed is if its flare lasts longer than Gaia's lifetime; however this is not likely to be a problem for TDEs, whose decay times tend to be less than five years.

It is also possible to account for the galaxy brightness using other observations of the galaxy. This requires accurate galaxy models or simulation. Knowing the galaxy intrinsic parameters, one may convert its brightness to Gaia's G band and integrate the light over Gaia's detection window. Another possibility, which is what was achieved in the first part of this work, is to fold the galaxy through Gaia simulation software to derive an empirical relation between its intrinsic parameters and Gaia observation.

A problem may arise with these methods if the galaxy is dimmer than 16th magnitude and the TDE is brighter as the window size will change with the addition of the bright source collecting more galaxy light. This effect is believed to have occurred in Fig. 5.17b giving the unusual periodicity. It may be very difficult to account for this effect for galaxies on the threshold. It is negated if the galaxy is very small or if it is significantly dimmer than the TDE. This effect would make it very difficult to identify a TDE when sampled with Gaia's cadence.

5.2.2 Detection efficiency

14 472 galaxy-TDE pairs were simulated across 254 runs. As can be seen in Fig. 4.13, the simulator coordinate bias had a very small effect in these simulations, approximately 0.7%. From the

previous part, it is expected that almost all of the galaxies would be detected. $V = 20$ galaxies were not simulated so their exact response is unknown but a large proportion of detections is expected and virtually all of the $V = 16$ and $V = 18$ galaxies are expected to be detected. These are simulated along with a point source, whose detection is very well understood (Prusti et al. 2016). This hypothesis is confirmed with 91% of the source pairs being detected. This part, however, is primarily concerned with how TDEs are detected and what can be expected from the results.

This high detection efficiency can be seen in the darker shades of blue in Fig. 5.13 which shows several 2D histograms comparing simulated and detected parameters (cf. Figs. 5.3 and 5.8). As described in Section 4.4, all galaxies are elliptical and have been reduced to two varying parameters: V magnitude and effective radius. TDEs only have one varying parameter which is its brightness and this varies according to time.

Figure 5.14 shows the detection efficiency with time. The detection efficiency always stays above 68% as this would be the efficiency of detecting the galaxies by themselves. This is the same detection efficiency as the ellipticals, indicating that at these three radii there is not a large difference in detection of $V = 20$ and $V = 21$ magnitude galaxies. It starts off at this minimum, before the occurrence of tidal disruption. The efficiency rises above this minimum as tidal disruption occurs and ascends to a peak of almost 100%, indicating that the peak of virtually all simulated TDEs is observed. This efficiency then drops off with the TDE brightness. The efficiency still remains approximately 17% above this minimum at the end of the simulated time, indicating that many of the brighter TDEs will remain visible to Gaia 500 days and more after disruption. The detection efficiency behaves as one would expect, but how these events are detected is discussed in the following section.

5.2.3 Detected brightness

Figure 5.15 shows the simulated and detected source pair magnitudes. The reason for the decreasing spikes with G magnitude is that these values are the input galaxy G magnitude and input TDE G magnitude added together. In adding two magnitudes in general, if they are similar then the resultant magnitude is almost one mag larger (each successive magnitude is 2.5 times smaller than the last); alternatively, if one value is a few magnitudes brighter than the other, the resultant is approximately the larger magnitude. These spikes are therefore at the locations of the galaxy magnitudes and the larger magnitudes are favoured. However, all magnitude contributions from the galaxies are slightly or largely shifted down depending on the size of the radius (as explained in the previous part), so the detected magnitude spread is quite different.

Detected magnitudes are broken down by galaxy magnitude and radius in Fig. 5.16. The usual general radius effect can be seen whereby the detected magnitude is shifted further with increasing galaxy radius as a larger fraction of the light falls outside the detection window. The general shape of the detected magnitude histogram is essentially the inverse of the light curve. This is because the magnitude plateaus and there are thus more occurrences of these lower

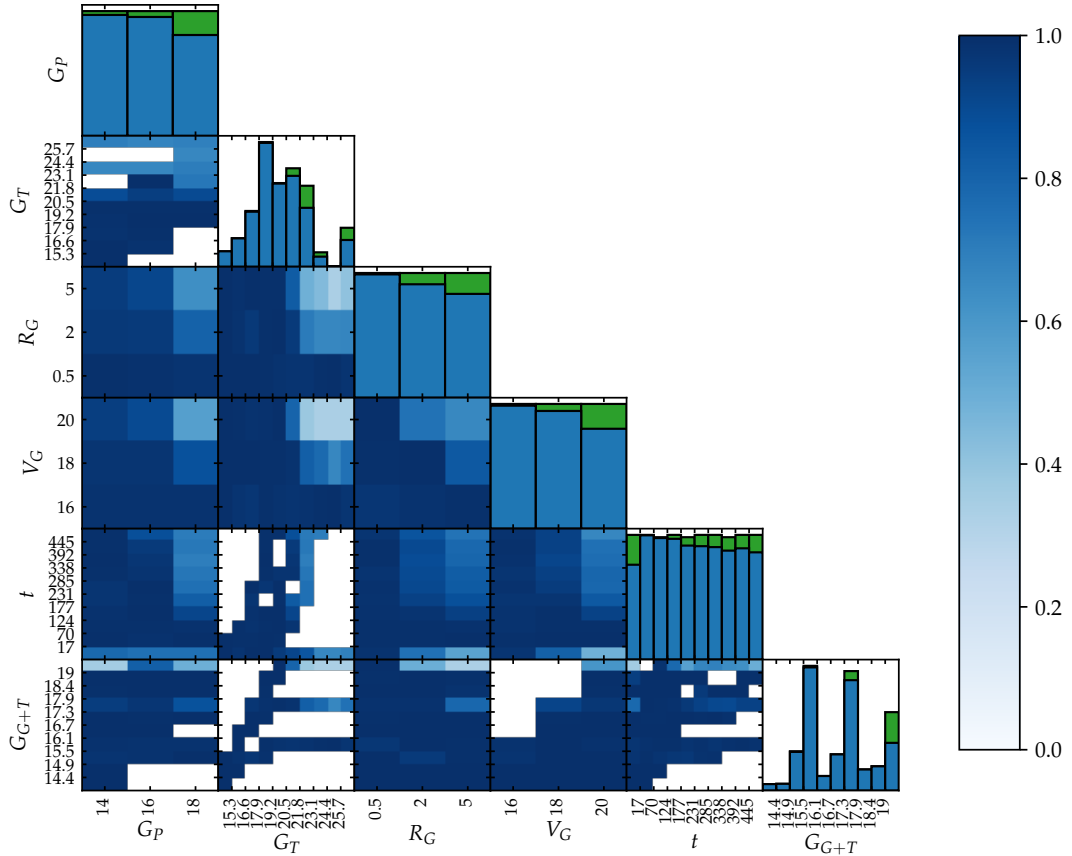


Figure 5.13: Detection efficiency of several input parameters in galaxy-TDE pairs. As before, the 2D histograms represent the detection efficiency for each pair of parameters. The 1D histograms on the diagonal represent the detected data overlaid on the simulated data. The colour bar thus only applies to the 2D histograms. G subscripted parameters belong to the galaxies and T subscripted parameters belong to TDEs, G_P refers to the peak TDE G magnitude per light curve. G_T values include all timesteps. The overall darker shades compared to Fig. 5.3 indicate that adding the point source the centre of the galaxy raises the detection efficiency (as expected), though the dim galaxies are also one magnitude brighter. The TDE peak luminosity has the largest effect on the efficiency since these events fade to magnitudes below Gaia's detection limit more quickly, and thus if the galaxy alone is not bright enough nothing will be detected. Note that units are excluded from this plot to reduce the amount of information; t is in days and all other quantities have their usual units.

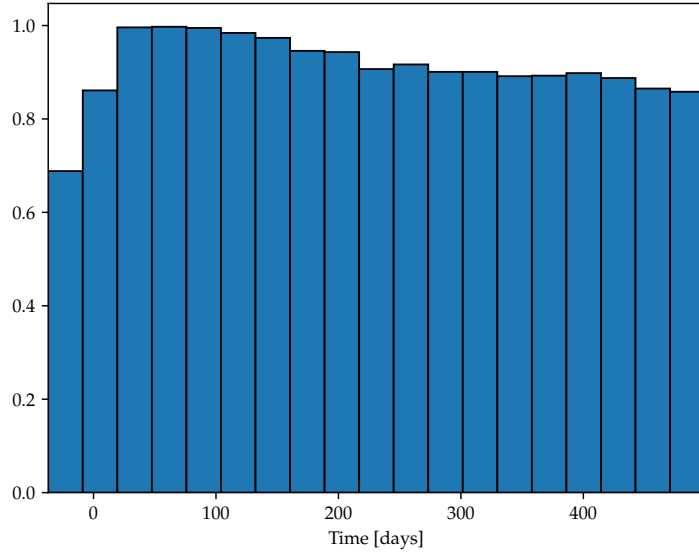


Figure 5.14: Detection efficiency of TDE-galaxy pairs with time. The efficiency mirrors the TDE light curve in that it starts off low before disruption, then rises with the accretion rate to a peak, before decaying.

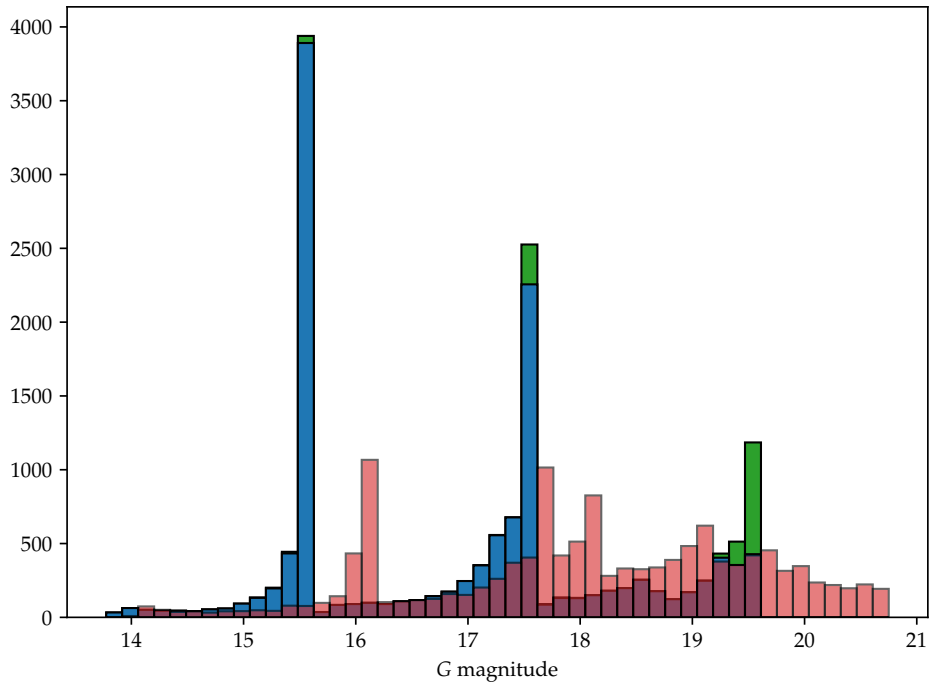


Figure 5.15: Histograms of intrinsic G magnitude (simulated in green, detected in blue) and detected G magnitude (transparent red). The green and blue histograms represent the simulated V data converted to a G magnitude, while the red histogram represents the detected G magnitude when accounting for the fact that part of the galaxy will fall outside the detection window; the total bin values of the red bins therefore will add up to the total blue bin values. Again, the detected magnitudes are quite varied but the galaxy brightnesses remain constant leading to the three peaks.

brightnesses.

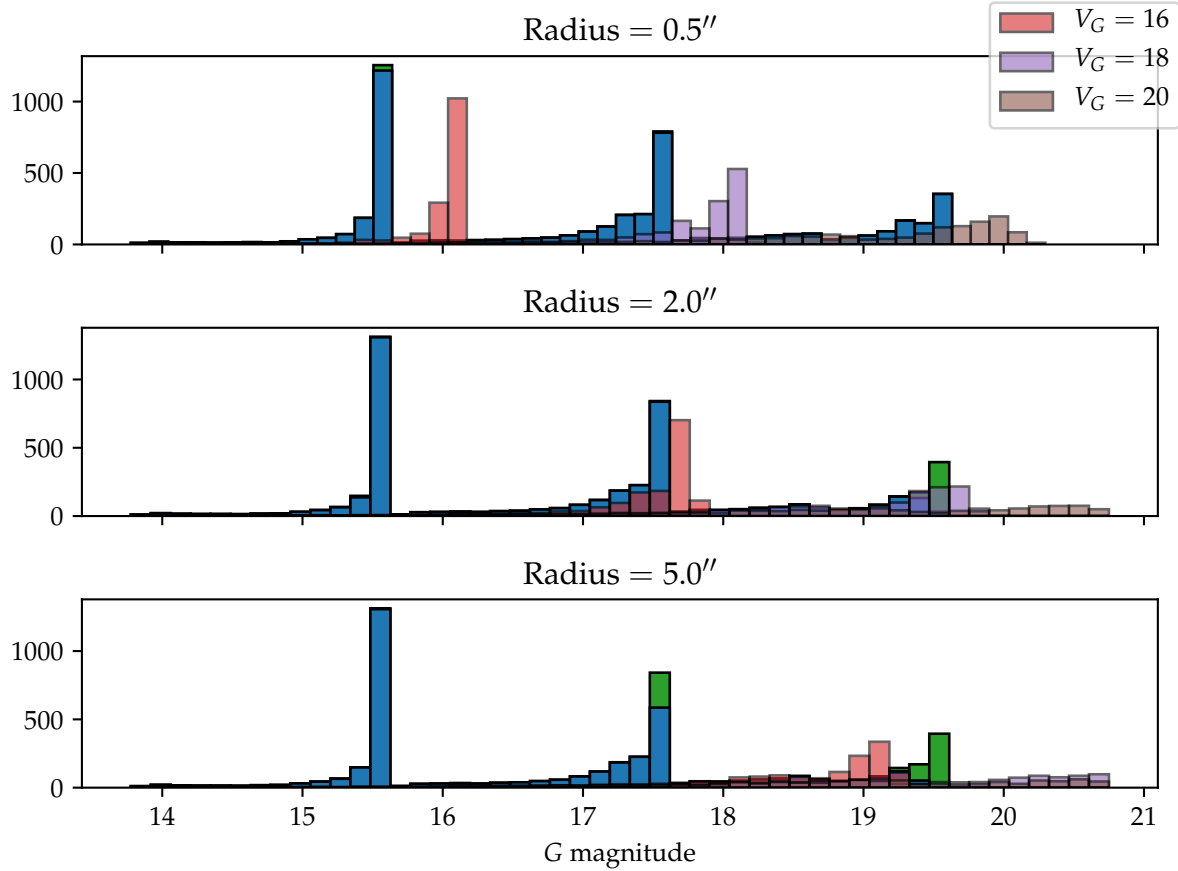


Figure 5.16: Detected G magnitudes separated by galaxy radius and V magnitude. The galaxy radius still causes a large shift in the detected G magnitude, however bright detections are still seen for each group as when the TDE peaks, it usually dominates the light yield.

5.2.4 Photometry

The TDEs which were simulated in grids were parsed and sorted into their respective light curves. A representative selection of these light curves is shown in Fig. 5.17. These light curves show the simulated and detected magnitudes of each galaxy-TDE pair. These are sampled at daily intervals. In order to conserve simulation time, sampling according to Gaia's cadence was done *a posteriori* so that there were no simulated duplicates, the results of which are discussed in the following section.

Although Gaia sampling will be much more infrequent, these complete light curves are useful for understanding how Gaia observes TDEs. Particularly interesting pairs, including bright TDEs and galaxies, dim TDEs and galaxies, a bright TDE and dim galaxy, etc. have been chosen so that patterns may be identified. It can be seen that at the peak of disruption, the flare usually dominates, and as this comes from a point source (where all the light is detected), the simulated and detected curves converge. Before disruption and at the plateau of the curve, the galaxy (if observed) usually makes a more significant contribution to the total detected light. Due to a

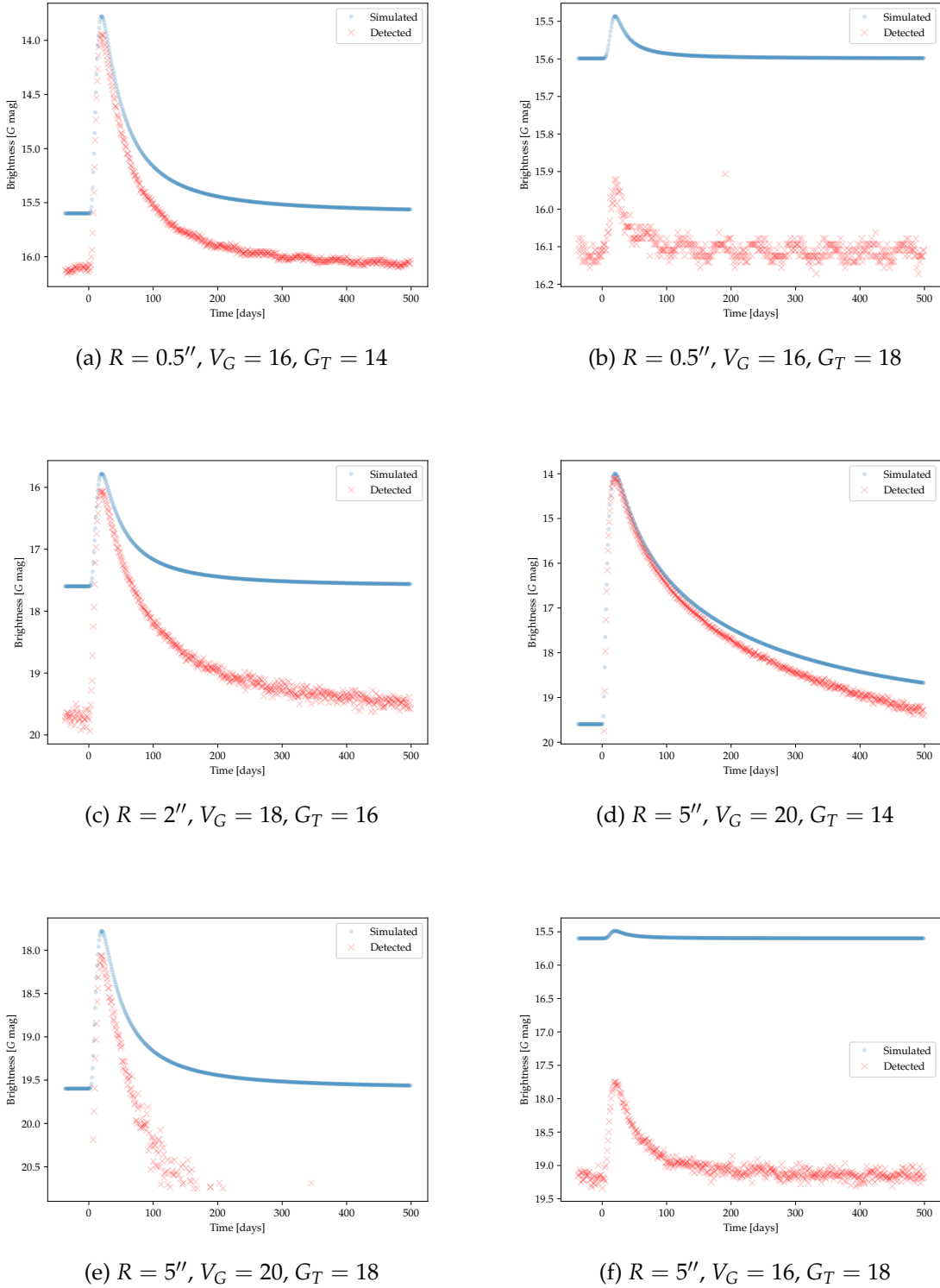


Figure 5.17: Six of 27 unsampled light curves comparing the input and the detected magnitudes. In general the detected light curve shows more exaggerated features of the input light curve due to it focusing on the galaxy centre. But the light curve is returned quite well (before sampling). b shows a strange periodicity in the detected light curve. This periodicity is not present in the input light curve and is suspected to be a result of the detection window size changing. The window size changes from 12×12 px to 12×18 px as sources get brighter than 16th magnitude. This light curve will be very difficult to detect as a TDE in Gaia after sampling.

fraction of the light from the galaxy falling outside the detection window there is often a large discrepancy between the simulated and detected curves.

This has the positive effect of making the detected curve steeper than the simulated curve, and thus making changes in source brightness (which would be used to initially identify a TDE) more apparent. A prime example of this is Fig. 5.17c, where the detected curve is significantly steeper than the simulated curve, and Fig. 5.17f whose simulated magnitude barely fluctuated at all. This, however, also causes regions of the curve to fall below Gaia’s detection limit as seen in Fig. 5.17e. If the TDE is very bright and the galaxy very dim, as in Fig. 5.17d there will not be much variation in the curves. The spread in detected points is larger at dimmer magnitudes due to a lower signal-to-noise ratio.

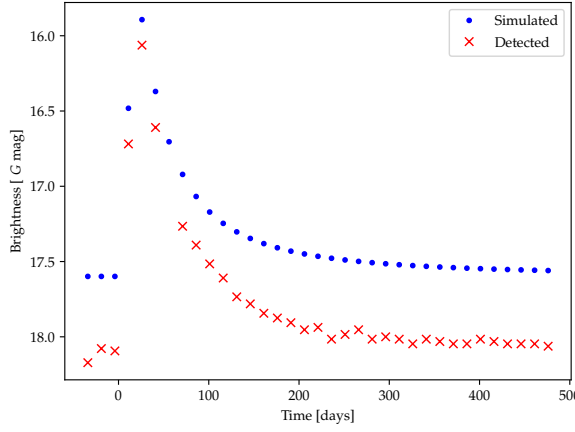
Figure 5.17b shows a strange periodicity in detected magnitude values. This may be due to a change in detection window size as the combined light from the galaxy and TDE crosses 16th magnitude. In this case the galaxy brightness is very close to 16th magnitude; the TDE is relatively dim but is bright enough to push it past 16th magnitude at the peak, where the effect is not seen. The periodicity may occur in sources which are very close to 16th magnitude and other subtle effects push the VPA detected magnitude above or below the threshold. It is not clear whether this effect occurs in Gaia or is just a result of the source spacing and other simulator effects. However, this is expected to occur in some form in Gaia; for example, in an elliptical galaxy which is near the threshold, the angle at which Gaia crosses it may push it above or below the threshold. It may also occur in transients flaring in galaxies which are very close to 16th magnitude as in this case. This effect was not seen in any other light curves, however, and so is expected to occur infrequently.

Sampled light curves

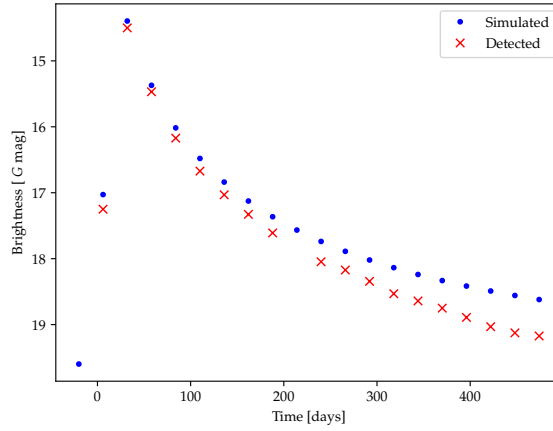
These daily sampled light curves were next sampled according to Gaia’s cadence, as described in Chapter 4. By sampling with varying cadence and a phase this resulted in 2106 light curves. Three of these are shown in Fig. 5.18. These represent what Gaia will observe in a TDE. Upon identifying a potential TDE as a source exhibiting a large increase in magnitude (or as a source ‘appearing’ during the Gaia lifetime), one may attempt to fit a light curve to its photometric data to further constrain its variability as TDE-like. In order to attain a light curve of the transient alone, the light from the galaxy must be accounted for. These problems are discussed in the following sections.

Light curve fitting

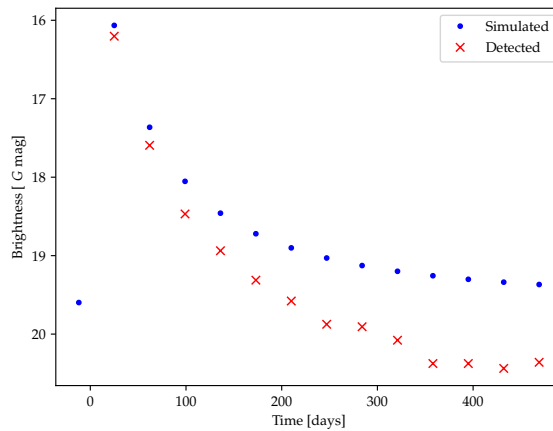
To account for the galaxies’ contributions to the light curves, elliptical galaxy data obtained in the previous part (Table 5.1) were interpolated to provide approximate G magnitudes. These data were found to vary approximately linearly on each table column/row, so a linear interpolation was used to generate the values seen in Table 5.5. Using these values emulates one having prior knowledge of the galaxy using data from another observatory as discussed previously. In reality one would probably use Gaia data taken before or after the TDE flare, however



(a) High cadence sampling with $R_G = 0.5''$, $V_G = 18$ and $G_T = 16$



(b) Medium cadence sampling with $R_G = 2''$, $V_G = 20$ and $G_T = 14$



(c) High cadence sampling with $R_G = 2''$, $V_G = 20$ and $G_T = 16$

Figure 5.18: Representative selection of high, medium and low sampled light curves. Comparing with Fig. 5.17, it is much harder to identify features of the light curves; however, the high cadence sample may enough resolution to identify light curve features.

this will not be possible for a galaxy which falls below Gaia's detection threshold (one third of the galaxies in Table 5.5).

	16	18	20
0.5	16.1	18.1	20.1
2	17.7	19.7	21.7
5	19.0	20.7	22.3

Table 5.5: Magnitude of galaxy within Gaia's detection window, obtained from linear interpolation of Table 5.1. V magnitudes are varied in rows and radii are varied in columns.

If one was doing a blind search of transient objects, ignoring the galaxy brightness and searching for

$$f = a(t + b)^{-5/3} + c$$

would give a good sense of the fit. Here a will account for the scaling of the light curve and b will account for any horizontal shifts in the light curve and c will account for the contribution from the galaxy. This was tested for several bright magnitude galaxies where it was found to hold; c returned a value approximately equal to the galaxy magnitude. To better constrain the model, the function which is to be fit to the flux data is

$$f = a(t + b)^{-5/3} + f_G,$$

where f_G is the flux from the galaxy. Accounting for the galaxy contribution reduces the number of free parameters, which is desired when performing a fit.

The process of batch fitting a $-5/3$ index power law is not something which would be done to claim conclusive discovery of a TDE, nor would it be feasible to do on the entire 2 PB archive, however it will be useful in eliminating other transient events whose light curves exhibit different properties. For comparison, the data were also fit by an exponential and a linear function of the forms

$$ae^{-t} + b \quad \text{and} \quad at + b.$$

A time shift is not included in these functions as it is absorbed into the other parameters. In reality, one would more likely want to fit possible AGN and SN light curves for comparison.

Fitting was done using an orthogonal distance regression algorithm (Boggs and Rogers 1990). This algorithm works by fitting a curve to a data set such that it minimises the sum of the squares of the orthogonal distances from each point to the curve. If successful, the algorithm converges on a minimum sum and provides an estimate to the best fit function parameters. The distances from each point to the curve are known as the residuals. The goodness of fit was estimated using a scaled standard deviation of the residuals, σ_r . This term provides a qualitative comparison for goodness of fit. The fit was applied from the maximum point on the light curve and from the point after the maximum, and the best fit chosen from these two. This second fit is to account for the possibility of the maximum being on the ascent or before the power law decay dominates the curve. The synthetic light curves defined in this work are quite

well behaved and tend to the $t^{-5/3}$ rather quickly, but realistic light curves may take longer so the fit may need to start at a later time.

Examples of the three fits to one light curve are shown in Fig. 5.19. Each plot shows the fit from the maximum point and the succeeding point. It can be seen that the exponential fit is very poor, which is generally the case. The linear fit is clearly a bad model, but would fit the plateau region quite well; therefore if peak observations were missed the TDE is likely to be missed. The power law fit, generally provides a very good fit to the data, as expected.

The mean σ_r value for each of the fits is 0.08, 2.23, 3.18 respectively, indicating that the power law provides a significantly better fit than the other two curves. These values do not change much with galaxy parameters; however, they are significantly affected by the TDE peak magnitude. Table 5.6 indicates the ratio of σ_r for the power law to the other fits. These ratios are seen to increase dramatically with increasing peak magnitude, indicating that the exponential and linear fits get comparatively better with decreasing TDE peak brightness. This suggests that this method of blind searching for light curves becomes less effective as TDE brightness decreases.

	linear	exponential
14	0.02	0.01
16	0.07	0.05
18	0.35	0.25

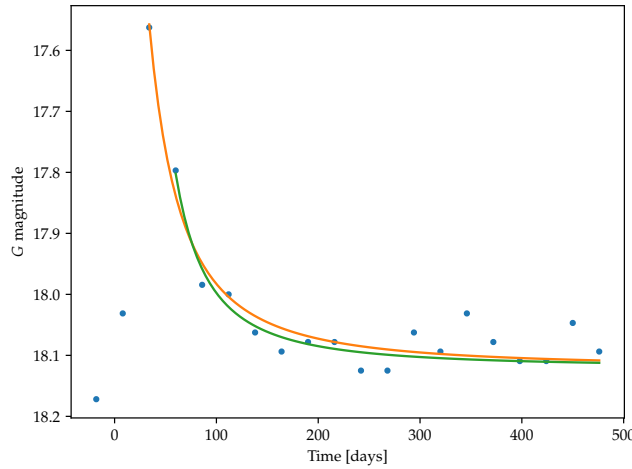
Table 5.6: Ratio of σ_r for power law fit to other fits for varying peak TDE brightnesses. 1 indicates an identical fit, less than 1 indicates a worse fit and greater than one indicates a better fit. Both fits are very poor for bright TDEs but improve as TDE brightness decreases. This does not mean that these fits get better with decreasing TDE brightness, but is instead because the power law fit also becomes very poor.

Power law fitting

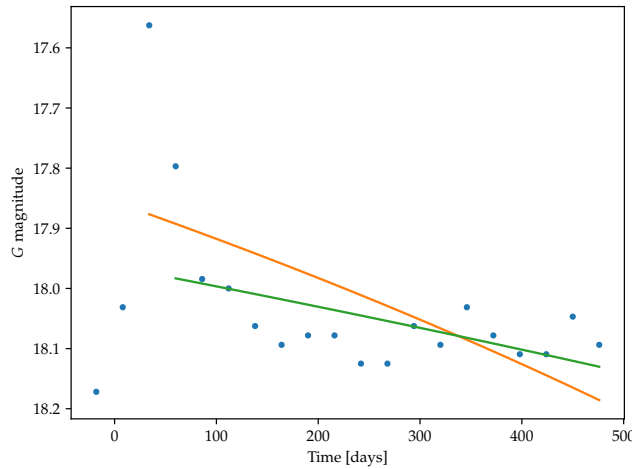
A similar approach may be used to test how well Gaia recovers the $-5/3$ index power law. This time it is assumed that the data are best fit by a power law, but the index is left free in the regression and fit to the data. The fitting function thus becomes

$$a(t + b)^n + f_G, \quad (5.1)$$

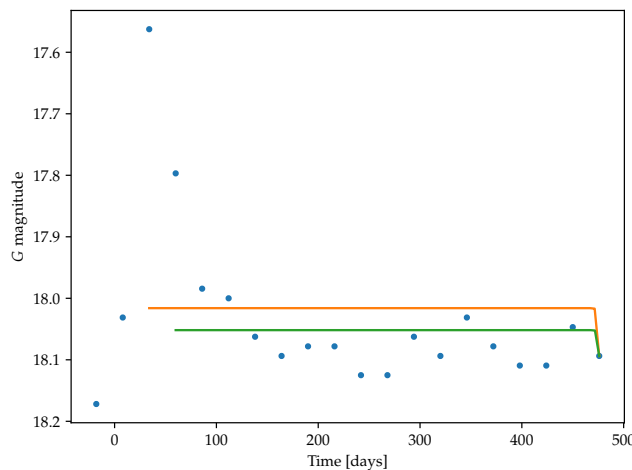
and a , b and n are determined by the same orthogonal distance regression algorithm as before. As there is an extra parameter to be fit and it is an exponent it will be more difficult for the fitting algorithm to converge. This function was fit to the 2106 Gaia-sampled light curves. As before, it was fit to the light curve from the maximum and the second from maximum points onward. If both fits converged the best fit of the two was chosen and the determined power law index selected. A representative selection of histograms of the recovered power law indices for each source parameter are shown in Fig. 5.20.



(a) Example power law fit



(b) Example linear fit



(c) Example exponential fit

Figure 5.19: Example $-5/3$ index power law, linear and exponential fits to light curve data. Note that these fits were done in linear space and converted to magnitudes. As expected, the power law fits quite well to the data, and the exponential and linear fits are poor.

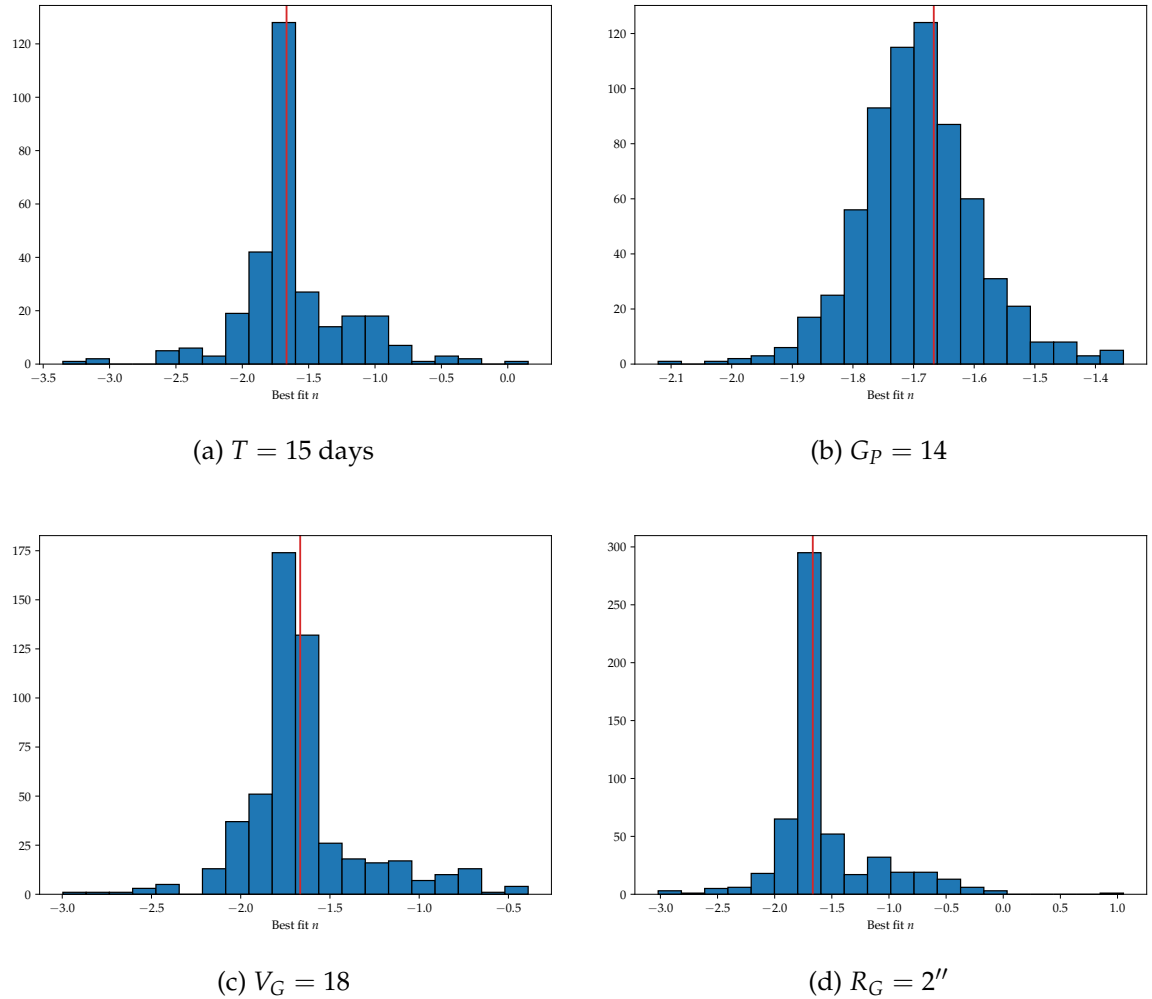


Figure 5.20: Representative sample of power law indices for varying source parameters. $-5/3$ is marked with a red line. The index is seen to be returned quite well through Gaia observation. T represents cadence here and all other symbols have their usual meaning.

Table 5.7 shows the mean best fit power law index and standard deviation, and the number of fits which did not converge for each parameter. The $-5/3 \sim -1.67$ index is returned reasonably well for all parameters except peak TDE brightness $G_P = 18$. The median index obtained from all fits is -1.66 , a very good response. The peak TDE brightness is seen to play a very important role in power law recovery: At $G_P = 14$ the mean index is quite accurate and there is a small spread in values. At $G_P = 16$ the mean index is less accurate and the spread gets larger. At $G_P = 18$ the mean index is quite inaccurate and the spread is larger still; looking at the large number of non-convergents, this was clearly not a good fit.

	mean index	non-convergents
$T = 37$	$-1.5(6)$	194/999
$T = 26$	$-1.5(5)$	112/702
$T = 15$	$-1.6(4)$	108/405
$V_G = 16$	$-1.5(8)$	183/702
$V_G = 18$	$-1.7(3)$	172/702
$V_G = 20$	$-1.5(4)$	59/702
$R_G = 0.5$	$-1.4(4)$	78/702
$R_G = 2$	$-1.6(4)$	147/702
$R_G = 5$	$-1.7(7)$	189/702
$G_P = 14$	$-1.7(1)$	36/702
$G_P = 16$	$-1.8(4)$	38/702
$G_P = 18$	$-0.8(6)$	340/702

Table 5.7: Best-fit power law indices with number of non-convergents for each source parameter. The index is returned quite accurately for all parameters except $G_P = 18$, which also had a very high non-convergence rate. T represents cadence in days here and all other symbols have their usual meaning.

414 fits did not converge in total, and 340 of these were for $G_P = 18$. This gets spread across all the other parameters raising their fractional non-convergents. For cadence values, the mean index is seen to get more accurate with increasing cadence¹ as these curves have more points and so a curve can be better constrained; however, the relative number of non-convergents is higher. Looking at the galaxy magnitudes, it is seen that the lesser magnitudes give rise to a better mean index, suggesting that the smaller the galaxy's contribution to the light curve the better it can be constrained. There may also be a small contribution from the light curve whose detection window size changed skewing the results slightly.

This effect is not seen with the radii however, as larger radii will give rise to a smaller G magnitude, as seen in Section 5.1. At lower radii, the fit is better constrained, and there are less non-convergents. This may be due to inaccuracies in the galaxy modelling, as there is a larger shift in the Gaia detected magnitude and galaxy intrinsic magnitude so the amount of light falling outside Gaia's detection window must be estimated. This illustrates the limitations of observing a TDE without observation of the galaxy on its own.

¹Increasing cadence corresponds to a decrease in the cadence value as seen in Table 5.7.

5.2.5 Potential of Gaia

Although better left to ground-based telescopes optimised for transient detection such as ASAS-SN or iPTF if possible, with astrometric, photometric and spectroscopic data, Gaia has a strong potential for TDE detection. The astrometric data will help to constrain the TDE to the centre of a galaxy, where the SMBH resides. The photometric data are taken at regular intervals which are not ideal for TDE observations but are such that they may provide a reasonable sampling of the light curve decay. TDEs occurring in very well observed regions of the sky may have a high enough sampling to discern peak features. The spectroscopic data will provide a low resolution spectral energy distribution across the optical band. This may not have enough resolution to observe emission lines, but will provide a sense of the colour and temperature of the source.

The methodology employed in this work will likely not provide a ‘smoking gun’ but may be used to obtain a narrow set of potential TDEs, on which more detailed analysis can be done. This work employed simplified models but in obtaining a narrow sample, more involved models may be fit, and supplementary spectroscopic data analysed. This work will be made available to the community so that when transient archive data are released, this methodology may be employed in a framework such as GAVIP (Section 3.7.2) for analysis.

Summary

Gaia’s response to elliptical and spiral galaxies was examined in a large scale simulation using GIBIS. A detailed picture of what types of galaxy Gaia will detect has been provided by examining the variation on detection efficiency across a wide range of parameters. This efficiency is a function of galaxy parameters, primarily brightness and radius. For $R = 5''$ the cut-off is approximately 21st magnitude in Johnson V , for $R = 2''$ the cut-off is approximately $V = 18$ th magnitude. The detected magnitudes were also analysed to provide an image of how Gaia is detecting these galaxies and what its response is. An empirical relation between intrinsic galaxy parameters, particularly V magnitude and radius, and detected G magnitude was derived. TDE light curves were also simulated in GIBIS to provide an image of Gaia’s response to them. The same analysis is applied to examine detection efficiencies and output magnitudes. The output light curves tend to exhibit more exaggerated features to the input light curves due to the fact that Gaia only observes a window of the galaxy. Using the empirical galaxy relation derived previously, multiple curves were fit to the data, including the desired $-5/3$ power law which generally fit the data quite well. This power law was also fit with the index as a free parameter, where it was found to generally return to approximately $-5/3$, for all sources except dim TDEs.

Chapter 6

Conclusions and Future Work

6.1 Summary conclusions

Though the field is very young, tidal disruption physics is growing at a very fast rate. It provides a unique avenue for probing black hole and accretion physics, which are otherwise difficult to explore. A theoretical framework was laid down by Phinney (1989) and Rees (1988), but much of the theory has developed in the last number of years as more strong candidates are discovered. It is widely believed that the process for occurrence of a tidal disruption event is a star within a galaxy nucleus gets perturbed onto a supermassive black hole loss cone orbit with pericentre within the tidal radius, i.e. the radius at which the tidal forces acting on the star from the black hole overcome the star's self gravity. The strength of disruption depends on the ratio of the tidal radius to the pericentre of the star's orbit, and the star may be survived by a core. Half of the matter is bound to the black hole and accreted, and half is unbound.

The accreting matter circularises at a rate which depends on the black hole mass and eventually tends to a fallback rate of $t^{-5/3}$. This rate has been observed to correlate with luminosities across different bands, including optical. Optical photometric and spectroscopic data have been taken for many potential TDEs leading to many strong candidates, including the well-sampled PS1-10jh (Gezari et al. 2012), and TDE1 and TDE2 which were discovered through SDSS archive data (van Velzen et al. 2011). There are still many open questions in the field, however, including the discrepancy in theoretical and observed TDEs rates, and the low energy yield compared to theoretically determined yields. As the field continues to evolve, it is imperative to obtain more candidates, and from as many different bands/instruments as possible to mitigate the possibility of an instrument bias, which may account for the reduced rate.

Gaia is an optical observatory which was launched in 2013 is predicted to detect 100–150 TDEs in its five year life cycle down to magnitude 19 in its 300–1100 nm G band (Blagorodnova et al. 2015). Gaia is an astrometric mission which is optimised for observing point point sources to fulfil its primary purpose of mapping out 1% of the Milky Way. It is the successor to Hipparcos, which before Gaia, had made the most accurate map of the Milky Way. Gaia consists of two telescopes which observe different parts of the sky simultaneously and focus light onto a

focal plane housing three primary instruments. These are an astrometric instrument, a photometric instrument and a spectroscopic instrument. Astrometry, photometry and low resolution spectroscopy across the G band are obtained for all sources and high resolution spectroscopy is obtained for sources down to a magnitude of approximately 17.

Gaia observes each part of the sky an average of 70 times over the course of the mission, each time crossing it at a different angle. This is done in order to constrain each source's location very well; these data are fed into a global astrometric solution whose final result will be the extremely precise map of the galaxy. Though this process is optimised for astrometry of point sources, the multiple observations make it useful for transient astronomy. The average cadence of ~ 30 days makes it suitable for detection of the decay in a TDE. If a transient is identified as it is detected it is released to the community so that follow-up may be attained, but it is anticipated that many transients will not be identified at this stage and will not appear until the archive. These data are not scheduled for release until 2023 and so have been simulated in this work.

Simulations were carried out using GIBIS which was developed before Gaia's launch to prepare for Gaia's observations and data stream. GIBIS allows simulation of several predefined sources, such as galaxies and user-defined sources. Since TDEs will generally be detected within a host galaxy, simulations were carried out with just galaxies as well as galaxies and TDEs to provide insight into how Gaia responds to these sources. GIBIS simulations are computationally expensive so many sources were simulated in each run and spaced in a grid.

The simulator was analysed to investigate its effectiveness and become aware of any possible defects it may possess. It was found that there was a bias in detection efficiency in the AC direction on the CCD which lowered the overall detection efficiency significantly. This effect was observed to depend on the number of sources per column. In order to mitigate this effect, the number of sources per column were reduced to three. Though this did not eliminate the bias completely, it reduced it such that it could be accounted for with a small correction. The effect lowered the overall efficiency by approximately 2% in the galaxy simulations and less than 1% in TDE simulations; however, it was found to affect bright sources more than dim ones and so gave a larger percentage error for these.

Galaxy parameters were chosen from two samples taken from SDSS database to give a broad coverage of elliptical and spiral galaxies which may harbour a TDE. 13 500 elliptical galaxies were simulated with a total adjusted efficiency of 68%. The elliptical galaxy effective radius and brightness were found to have the largest effects on the detection efficiency. The G brightness was found to be approximately 0.4 magnitudes less than the V brightness, allowing approximately half of the $V = 21, R = 0.5''$ galaxies to be detected. However, for larger radii much of the light falls outside the detection window dropping the brightness within the window to less than Gaia's limit. At $V = 15$, over 95% of the sources are detected consistently as expected. A slightly higher efficiency is seen for more elliptical galaxies, i.e. E7 galaxies. This suggests that Gaia will favour detection of small, more elliptical galaxies.

The detection window size also gives rise to a shift in the intrinsic vs detected G magnitude. The detected G magnitude is seen to reduce more for larger radii and ellipticities. By fitting a

Gaussian curve to the detected G magnitudes, an empirical relationship was derived between intrinsic galaxy parameters and detected G magnitude. Gaia's detection window will make it difficult to compare Gaia data of galaxies with other data. The relationship derived in this work allows one to convert observations made with another telescope (assuming the galaxy radius and ellipticity can be measured) to a Gaia magnitude; however, it will not be possible to convert a Gaia G magnitude to a Johnson V magnitude, for example, without galaxy modelling to determine how much of the light is falling inside the detection window.

Spiral galaxies have a lower efficiency overall than ellipticals. A detection efficiency of 61% was observed for 8100 spirals. By varying the bulge to total ratio parameter, the effect of the disk and bulge relative intensity could be compared. When the bulge dominated the light yield, a high efficiency was seen as the bulges were identical to the elliptical galaxies used in the previous simulations, except that they were three times smaller, allowing most of the light in general to fit in the detection window. When the disk dominated the light yield a low detection efficiency was seen indicating that Gaia is not suited to detection of spiral disks.

The detected magnitude shifts are similar to ellipticals except that the bulge to total ratio parameter also has an effect, with smaller bulge to total ratios causing larger detected G magnitude shifts. As with ellipticals an empirical relationship between spiral intrinsic parameters and detected Gaia G magnitude was derived. Comparing spirals to ellipticals, spirals are seen to have an overall slightly reduced efficiency (hence a larger magnitude shift); however, this efficiency depends largely on how dominant the disk is. So-called 'disky' galaxies will have poor detection efficiencies, whereas bulge-dominated galaxies will have high efficiencies.

For the TDE simulations, an elliptical galaxy with the same parameters except brightness and radius was employed for all simulations. TDE brightness was varied according to a synthetic light curve defined to exhibit a rise in luminosity according to a power law of undetermined index but whose shape roughly matches simulations by Guillochon and Ramirez-Ruiz (2013). Three different TDE peak brightnesses were used giving three different light curves. These light curves were sampled in one day increments and at each time a brightness was extracted. Each of these brightnesses were simulated as a separate point source and placed on top of one of nine galaxy types, providing 27 light curve simulations. These were simulated in a grid as with the galaxies and each grid point consisted of an elliptical galaxy with a TDE on top of its centre.

As the majority of galaxies simulated fall within Gaia's detection limit and each has a point source with a brightness up to 14th magnitude placed on top of it, the overall detection efficiency is quite high at 91%. Like the TDE brightness, this efficiency rises to a peak and falls off as the TDEs decay. The end of the light curve is higher than was observed for just galaxies of these magnitudes indicating that many bright TDEs will be seen 500 days and more after disruption. The TDE peak magnitude, galaxy effective radius and brightness all affect the efficiency as expected, with lower magnitudes and higher radii reducing detection efficiencies at late times. With two sources per detection, the detected brightnesses are slightly more unusual. The effect of each parameter can be seen, however, in line with the effects on efficiency. For very bright TDEs the decay will be long-lived and will thus be very well sampled by Gaia.

One of the daily sampled light curves showed a strange periodicity in its brightness. This is suspected to be due to the galaxy being very close to 16th magnitude, where the detection window changes size, collecting more or less of the galaxy light. Though it is rare for this have a large effect, it will make it very difficult to identify transients by their light curve which are affected.

Comparing the daily sampled light curves to the light curves sampled according to Gaia's cadence, the peak becomes more difficult to identify. A large rise may be seen from before disruption to after, however the location of the peak is difficult to identify. It may be possible in regions which are very highly sampled. This suggests that Gaia will in general not be suitable for determining the peak time of a TDE. It may be possible to determine the peak time for a slowly circularising black hole with a slow rising peak, i.e. lower mass SMBHs. This may even extend to IMBHs. Since this information is what may be used to estimate the mass of the disrupting black hole, in general it is not anticipated that this information will be made accessible through Gaia observations, without observations made with other telescopes. Gaia is, however, suited to sampling the $t^{-5/3}$ decay of a TDE.

Gaia's response to this power law was investigated by fitting an arbitrary power law to the observed light curves, and determining the index by orthogonal distance regression. Galaxy G magnitudes are modelled in the fit using the empirical relation derived earlier. This would be less effective than using observations made before or after the TDE flare of the galaxy on its own, but these data will not always be available. The overall response is good with a median best-fit index of -1.66 . However, the fit was very poor for a TDE peak magnitude of 18, with a high non-convergence rate. This suggests that it will be very difficult to identify TDEs with a peak magnitude at 18 or lower using just Gaia data. Blagorodnova et al. (2015) suggests 20–30 TDEs per year in Gaia with $G > 19$; however, many of these may be unidentifiable as TDEs using Gaia data alone.

The light curve data were also batch fit with a $-5/3$ index power law, and some other simple fits for comparison. The other fits used were simply an exponential and a linear function. Across the sample, the power law provided a significantly better fit to the data, however, the relative quality of this fit compared to the other fits declined with decreasing TDE peak brightness, similar to the arbitrary power law fit. The relative goodness of fit also degraded as the cadence decreased, indicating that there will be a bias towards finding TDEs in parts of the sky better-sampled by Gaia; this is simply a result of the Gaia scanning law. This blind search method would likely only be used to narrow down the sample to a more manageable number which could then be analysed more rigorously, making use of the low-resolution spectra, and if available, other survey observations.

Overall, Gaia shows good potential for TDE detection. Ideally, a detection will be released as a photometric alert and follow-up may better constrain its properties; however, there should also be many in the archive. The suggested 100–150 over its lifetime will likely be much higher than the number which are actually identifiable. A previous archival search of SDSS by van Velzen et al. (2011) yielded two TDEs. A similar approach in the Gaia archive could yield more results. This archival search will be facilitated by GAVIP.

6.2 Future work

Although the simulations were designed and analysed as part of this work, it was not possible to run the proprietary software locally; this limited computational time. Further simulation will provide better statistics and allow a higher parameter resolution; e.g. galaxy brightnesses could be varied in 1 magnitude increments to better refine the Gaia detection cut-off for each radius. Hydrodynamical simulations would provide a more accurate light curve simulation, including the rise time. These simulations could be done for a variety of black hole masses to determine for what mass Gaia can constrain the peak time and will thus be best suited to detecting. SNe and AGN will likely be the largest contaminants for TDE identification. Simulations of various classes of SNe and AGN will provide an idea of how these objects compare photometrically in Gaia.

As spectra are provided for a user-defined source in GIBIS, it may be useful to insert a realistic spectrum and view the output of the simulated BP and RP. These spectra are very low resolution so emission lines will likely not be resolved but it should allow identification of a blue source, and may facilitate fitting of a blackbody spectrum to allow an estimate of the temperature. Similar exercises could be done for SNe and AGN for comparison. This will also provide consistent measurements of a bright enough source as it decays, so if a TDE is identified through another survey, these spectral data can be supplementary, providing information on the evolution of the colour and temperature.

The largest piece of future work which should be done is in 2023, when the final Gaia archive is released. The work done here could be easily ported into an AVI to run in GAVIP and perform analysis on the Gaia archive. Many of the sources in the archive will be classified so the first data reduction which could be done is eliminating everything which is classified as something other than a unknown transient. This number could be cut further by eliminating sources with a peak magnitude less than a user-defined value; this could be set to 18 for example to cut out faint TDEs (and other sources) or set higher if the number of sources is too large. A further reduction could be done by comparing the highest magnitude recorded with the last magnitude recorded and looking for a Δ above a certain threshold; again this threshold could be used as a filter to raise or lower numbers. AGN and SN would be eliminated using methods described above. The strictness of these conditions would be set to return a final number which is manageable to fit TDE models, and look for potential data taken with other observatories.

This could also be extended to test TDE hypotheses or measure rates. By simulating a large sample of TDEs according to an hypothesis, this hypothesis can be tested by comparing the results of the simulations with the final archive. For example, by simulating TDEs according to a chosen rate (e.g. Stone and Metzger 2015's rate), and comparing this to the rate of detected TDEs in the final archive, one can get an estimate of the validity of their hypothesis. This could be applied to the host galaxies too. GOG would probably be a better tool for this purpose, however, since it outputs archive data and is better suited to examining large samples. A purpose-built TDE Gaia simulator, which allows would allow models to be inserted and would simulate TDEs across the sky throughout Gaia's lifetime, would be ideal; however, this would

be a large task.

In summary, further simulation, both in simulating TDEs (and other objects) and Gaia's response, would add greatly to this work. These simulations could be used to train Gaia to better identify TDEs in the catalogue when it is released. This could even lead to the development of a purpose-built TDE Gaia simulator which would take theoretical TDE models and simulate them within Gaia. This simulator could be used to test theories by examining features and rates and comparing them against the final catalogue when it becomes available. The software written over the course of this work should be applicable to real galaxy and TDE data, and may be found online so that astrophysicists may do so later.

Bibliography

Note that entry titles are hyperlinks in electronic version.

- Abbott BP et al. (2016). "Observation of gravitational waves from a binary black hole merger". In: *Physical Review Letters* 116.6, pp. 1–16.
- Alexander T (2012). "Stellar dynamics and tidal disruption events in galactic nuclei". In: *EPJ Web of Conferences* 39. Ed. by R Saxton and S Komossa, p. 05001.
- Antiche E et al. (2014). "The Gaia Object Generator (GOG)". In: *EAS Publications Series* 67-68.2014. Ed. by N Walton et al., pp. 355–355.
- Arcavi I et al. (2014). "A Continuum of H- to He-rich Tidal Disruption Candidates with a Preference for E+A Galaxies". In: *The Astrophysical Journal* 793.1, p. 38.
- Arianespace (2013). *Gaia Launch*. Tech. rep.
- Babusiaux C (2004). "The Gaia Instrument and Basic Image Simulator". In: *4e Semaine de l'Astrophysique Francaise*, pp. 417–420.
- Babusiaux C et al. (2015). *The Gaia instrument and basic image simulator User Guide*. Tech. rep. Gaia Data Processing and Analysis Consortium.
- Bailer-Jones C (2010). "The ILIUM forward modelling algorithm for multivariate parameter estimation and its application to derive stellar parameters from Gaia spectrophotometry". In: *Monthly Notices of the Royal Astronomical Society* 403.1, pp. 96–116.
- Bertin E (2009). "SkyMaker: astronomical image simulations made easy." In: *Memorie della Società Astronomica Italiana* 80, p. 422.
- Binney J and Merrifield M (1998). "Galactic Astronomy". Princeton University Press.
- Blagorodnova N et al. (2015). "Gaia transient detection efficiency: hunting for nuclear transients". In: 14.November, pp. 1–14.
- Boehle A et al. (2016). "An Improved Distance and Mass Estimate for Sgr A* from a Multistar Orbit Analysis". In: *The Astrophysical Journal* 830.1, p. 17.
- Boggs PT and Rogers JE (1990). "Orthogonal distance regression". In: *Contemporary Mathematics* 112, pp. 183–194.
- Bonnerot C, Rossi EM and Lodato G (2016). "Long-term stream evolution in tidal disruption events". In: 15.August, pp. 1–15.
- Bonnerot C, Rossi EM, Lodato G and Price DJ (2016). "Disc formation from tidal disruptions of stars on eccentric orbits by Schwarzschild black holes". In: *Monthly Notices of the Royal Astronomical Society* 455.2, pp. 2253–2266.
- Bower RG et al. (2006). "Breaking the hierarchy of galaxy formation". In: *Monthly Notices of the Royal Astronomical Society* 370.2, pp. 645–655.

- Brown AGA et al. (2016). "Gaia Data Release 1: Summary of the astrometric, photometric, and survey properties Gaia". In: *Astronomy & Astrophysics* 595, A2.
- Campbell HC et al. (2015). "Total eclipse of the heart: the AM CVn Gaia14aae/ASSASN-14cn". In: *Monthly Notices of the Royal Astronomical Society* 452.1, pp. 1060–1067.
- Carrasco JM et al. (2016). "Gaia Data Release 1: Principles of the photometric calibration of the G band". In: *Astronomy & Astrophysics* 595, A7.
- Charvet P (2006). "Gaia Payload Module Description". In: 621.1, p. 23.
- Crowley C et al. (2016). "Gaia Data Release 1: On-orbit performance of the Gaia CCDs at L2". In: *Astronomy & Astrophysics* 595, A6.
- Dai L, McKinney JC and Miller MC (2015). "Soft X-ray Temperature Tidal Disruption Events from Stars on Deep Plunging Orbits". In: *The Astrophysical Journal* 812.2, p. L39.
- De Bruijne J, Kohley R and Prusti T (2010). "Gaia: 1,000 million stars with 100 CCD detectors". In: *Space Telescopes and Instrumentation 2010: Optical, Infrared, and Millimeter Wave* 7731.Figure 1, pp. 1–15.
- De Bruijne JHJ (2012). "Science performance of Gaia, ESA's space-astrometry mission". In: *Astrophysics and Space Science* 341.1, pp. 31–41.
- De Souza RE et al. (2014). "Detection of galaxies with Gaia". In: *Astronomy & Astrophysics* 568, A124.
- Downes R, Webbink RF and Shara MM (1997). "A Catalog and Atlas of Cataclysmic Variables- Second Edition". In: *Publications of the Astronomical Society of the Pacific* 109.1998, p. 345.
- Einstein A (1939). "On a Stationary System With Spherical Symmetry Consisting of Many Gravitating Masses". In: *The Annals of Mathematics* 40.4, p. 922.
- Eisenhauer F et al. (2005). "SINFONI in the Galactic Center: Young Stars and Infrared Flares in the Central Light-Month". In: *The Astrophysical Journal* 628.1, pp. 246–259.
- Evans CR and Kochanek CS (1989). "The tidal disruption of a star by a massive black hole". In: *The Astrophysical Journal* 346, p. L13.
- Fabricius C et al. (2016). "Gaia Data Release 1: Pre-processing and source list creation". In: *Astronomy & Astrophysics* 595, A3.
- Frank J, King A and Raine D (2002). "Accretion Power in Astrophysics". 3rd ed. Cambridge University Press.
- Freedman RA (2016). "Sears and Zemansky's university physics". 14th ed. Vol. 1. Pearson Education.
- French J et al. (2004). "Watcher: A Telescope for Rapid Gamma-Ray Burst Follow-Up Observations". In: *AIP Conference Proceedings*. Vol. 727. 2004. AIP, pp. 741–744.
- French KD, Arcavi I and Zabludoff A (2016). "Tidal Disruption Events Prefer Unusual Host Galaxies". In: *The Astrophysical Journal* 818.1, p. L21.
- Gebhardt K et al. (2000). "A Relationship between Nuclear Black Hole Mass and Galaxy Velocity Dispersion". In: *The Astrophysical Journal* 539.1, pp. L13–L16.
- Gezari S (2016). "Observations of Tidal Disruption Events". The Ninth Harvard-Smithsonian Conference on Theoretical Astrophysics.
- (2014). "The tidal disruption of stars by supermassive black holes". In: *Physics Today* 67.5, pp. 37–42.

- Gezari S et al. (2012). "An ultraviolet-optical flare from the tidal disruption of a helium-rich stellar core." In: *Nature* 485.7397, pp. 217–20.
- Gezari S et al. (2015). "PS1-10jh Continues to Follow theFallback Accretion Rate of a Tidally Disrupted Star". In: *The Astrophysical Journal* 815.1, p. L5.
- Gezari S et al. (2008). "UV/Optical Detections of Candidate Tidal Disruption Events by GALEX and CFHTLS". In: *The Astrophysical Journal* 676.2, pp. 944–969.
- Giannios D and Metzger BD (2011). "Radio transients from stellar tidal disruption by massive black holes". In: *Monthly Notices of the Royal Astronomical Society* 416.3, pp. 2102–2107.
- Gielesen W et al. (2013). "Gaia basic angle monitoring system". In: *Proceedings of SPIE* 8442.8863, 88630G.
- Guillochon J, Manukian H and Ramirez-Ruiz E (2014). "PS1-10jh: The Disruption of a Main-sequence Star of Near-solar Composition". In: *The Astrophysical Journal* 783.1, p. 23.
- Guillochon J, McCourt M et al. (2016). "Unbound Debris Streams and Remnants Resulting From the Tidal Disruptions of Stars By Supermassive Black Holes". In: *The Astrophysical Journal* 822.1, p. 48.
- Guillochon J, Parrent J and Margutti R (2016). "An Open Catalog for Supernova Data". In: p. 24.
- Guillochon J and Ramirez-Ruiz E (2015). "A Dark Year for Tidal Disruption Events". In: *The Astrophysical Journal* 809.2, p. 166.
- (2013). "Hydrodynamical Simulations To Determine the Feeding Rate of Black Holes By the Tidal Disruption of Stars: the Importance of the Impact Parameter and Stellar Structure". In: *The Astrophysical Journal* 767.1, p. 25.
- Haas R et al. (2012). "Tidal Disruptions of White Dwarfs From Ultra-Close Encounters With Intermediate-Mass Spinning Black Holes". In: *The Astrophysical Journal* 749.2, p. 117.
- Harrison DL (2011). "A fast 2D image reconstruction algorithm from 1D data for the Gaia mission". In: *Experimental Astronomy* 31.2-3, pp. 157–175.
- Hawking SW (1975). "Particle creation by black holes". In: *Communications In Mathematical Physics* 43.3, pp. 199–220.
- Hills JG (1975). "Possible power source of Seyfert galaxies and QSOs". In: *Nature* 254, pp. 295–298.
- Hodgkin ST et al. (2013). "Transient astronomy with the Gaia satellite". In: *Philosophical Transactions of the Royal Society A: Mathematical, Physical and Engineering Sciences* 371.1992, pp. 20120239–20120239.
- Holoién TWS et al. (2016). "Six months of multiwavelength follow-up of the tidal disruption candidate ASASSN-14li and implied TDE rates from ASAS-SN". In: *Monthly Notices of the Royal Astronomical Society* 455.3, pp. 2918–2935.
- Hopman C and Alexander T (2006). "Resonant Relaxation near a Massive Black Hole: The Stellar Distribution and Gravitational Wave Sources". In: *The Astrophysical Journal* 645.2, pp. 1152–1163.
- Hubble EP (1926). "Extragalactic nebulae." In: *The Astrophysical Journal* 64, p. 321.
- Hudec R, Šimon V and Hudec L (2010). "Photometry and Low Dispersion Spectroscopy with ESA Gaia". In: *Advances in Astronomy* 2010, pp. 1–7.

- Ivanov PB, Polnarev AG and Saha P (2005). "The tidal disruption rate in dense galactic cusps containing a supermassive binary black hole". In: *Monthly Notices of the Royal Astronomical Society* 358.4, pp. 1361–1378.
- James O et al. (2015). "Gravitational lensing by spinning black holes in astrophysics, and in the movie Interstellar". In: *Classical and Quantum Gravity* 32.6, p. 065001.
- Jones MH and Lambourne RJ (2007). "An Introduction to Galaxies and Cosmology". Cambridge University Press.
- Jordi C et al. (2010). "Gaia broad band photometry". In: *Astronomy & Astrophysics* 523, A48.
- Kaiser N and Pan-STARRS Team (2002). "The Pan-STARRS Optical Survey Telescope Project". In: *American Astronomical Society Meeting Abstracts*. Vol. 34. Bulletin of the American Astronomical Society, p. 1304.
- Kangas T et al. (2016). "Gaia16apd – a link between fast-and slowly-declining type I superluminous supernovae". In: 12.December, pp. 1–12.
- Karas V and Šubr L (2007). "Enhanced activity of massive black holes by stellar capture assisted by a self-gravitating accretion disc". In: *Astronomy and Astrophysics* 19, pp. 11–19.
- Kerr RP (1963). "Gravitational Field of a Spinning Mass as an Example of Algebraically Special Metrics". In: *Physical Review Letters* 11.5, pp. 237–238.
- Khokhlov A and Melia F (1996). "Powerful Ejection of Matter from Tidally Disrupted Stars near Massive Black Holes and a Possible Application to Sagittarius A East". In: *The Astrophysical Journal* 457.2.
- Kim K et al. (2016). "The Demographics of Galactic Bulges in the SDSS Database". In: *The Astrophysical Journal Supplement Series* 225.1, p. 6.
- Kızıltan B, Baumgardt H and Loeb A (2017). "An intermediate-mass black hole in the centre of the globular cluster 47 Tucanae". In: *Nature* 542.7640, pp. 203–205.
- Kochanek CS (2016). "Tidal disruption event demographics". In: *Monthly Notices of the Royal Astronomical Society* 461.1, pp. 371–384.
- Komossa S (2015). "Tidal disruption of stars by supermassive black holes: Status of observations". In: *Journal of High Energy Astrophysics* 7, pp. 148–157.
- Komossa S and Merritt D (2008). "Tidal Disruption Flares from Recoiling Supermassive Black Holes". In: *The Astrophysical Journal* 683.1, pp. L21–L24.
- Lapedes DN (1978). "Dictionary of physics and mathematics". McGraw-Hill.
- Laurikainen E, Reynier Peletier R and Gadotti D (2016). "Galactic Bulges". Springer.
- Leloudas G et al. (2016). "The superluminous transient ASASSN-15lh as a tidal disruption event from a Kerr black hole". In: *Nature Astronomy* 1.1, p. 0002.
- Lin D et al. (2017). "A likely decade-long sustained tidal disruption event". In: *Nature Astronomy* 1, p. 0033.
- Lindgren L and Bastian U (2011). "Basic principles of scanning space astrometry". In: *EAS Publications Series* 45.2010, pp. 109–114.
- Lindgren L and Perryman MAC (1997). "GAIA: Global astrometric interferometer for astrophysics". In: *European Space Agency, (Special Publication) ESA SP* 402, pp. 799–802.
- Lindgren L et al. (2016). "Gaia Data Release 1: Astrometry: one billion positions, two million proper motions and parallaxes". In: *Astronomy & Astrophysics* 595, A4.

- Lindgren L et al. (2012). "The astrometric core solution for the Gaia mission: Overview of models, algorithms, and software implementation". In: *Astronomy & Astrophysics* 538, A78.
- Lindgren L et al. (2008). "The Gaia mission: science, organization and present status". In: *Proceedings of the International Astronomical Union* 3.S248, pp. 217–223.
- Lintott CJ et al. (2011). "Galaxy Zoo 1: Data release of morphological classifications for nearly 900 000 galaxies". In: *Monthly Notices of the Royal Astronomical Society* 410.1, pp. 166–178.
- Lintott CJ et al. (2008). "Galaxy Zoo: Morphologies derived from visual inspection of galaxies from the Sloan Digital Sky Survey". In: *Monthly Notices of the Royal Astronomical Society* 389.3, pp. 1179–1189.
- Liu FK, Li S and Chen X (2009). "Interruption of Tidal-Disruption Flares By Supermassive Black Hole Binaries". In: *The Astrophysical Journal* 706.1, pp. L133–L137.
- Liu FK, Li S and Komossa S (2014). "A Milliparsec Supermassive Black Hole Binary Candidate in the Galaxy SDSS J120136.02+300305.5". In: *The Astrophysical Journal* 786.2, p. 103.
- Lodato G (2012). "Challenges in the modeling of tidal disruption events lightcurves". In: *EPJ Web of Conferences* 39. Ed. by R Saxton and S Komossa, p. 01001.
- Lodato G, King AR and Pringle JE (2009). "Stellar disruption by a supermassive black hole: Is the light curve really proportional to $t^{-5/3}$?" In: *Monthly Notices of the Royal Astronomical Society* 392.1, pp. 332–340.
- Lodato G and Rossi EM (2011). "Multiband light curves of tidal disruption events". In: *Monthly Notices of the Royal Astronomical Society* 410.1, pp. 359–367.
- Loreggia D et al. (2004). "Fizeau interferometer for global astrometry in space". In: *Applied Optics* 43.4, p. 721.
- Luri X, Babusiaux C and Masana E (2005). "Modelling the Instruments and Simulating the Data Stream". In: *The Three-Dimensional Universe with Gaia*, pp. 357–360.
- Luri X et al. (2014). "Overview and stellar statistics of the expected Gaia Catalogue using the Gaia Object Generator". In: *Astronomy & Astrophysics* 566, A119.
- MacLeod M, Guillochon J and Ramirez-Ruiz E (2012). "the Tidal Disruption of Giant Stars and Their Contribution To the Flaring Supermassive Black Hole Population". In: *The Astrophysical Journal* 757.2, p. 134.
- Makarov VV (1998). "Absolute measurements of trigonometric parallaxes with astrometric satellites". In: *Astron. Astrophys* 340.1, pp. 309–314.
- Masana E et al. (2005). "The Gaia System Simulator". In: *The Three-Dimensional Universe with Gaia*.
- Matthews TA and Sandage AR (1963). "Optical Identification of 3c 48, 3c 196, and 3c 286 with Stellar Objects." In: *The Astrophysical Journal* 138, p. 30.
- Melia F (2003). "The Edge of Infinity: Supermassive Black Holes in the Universe". Cambridge University Press, p. 148.
- Mignard F et al. (2007). "Gaia: organisation and challenges for the data processing". In: *Proceedings of the International Astronomical Union* 3.S248.
- Miller MC and Colbert EJM (2004). "Intermediate-Mass Black Holes". In: *International Journal of Modern Physics D* 13.01, pp. 1–64.
- Milligan DJ (2016). "Flying ESA's ultra-precise Gaia Mission". In: *SpaceOps 2016 Conference*. May. Reston, Virginia: American Institute of Aeronautics and Astronautics, pp. 1–20.

- Milligan DJ et al. (2016). "ESA's billion star surveyor – Flight operations experience from Gaia's first 1.5 Years". In: *Acta Astronautica* 127, pp. 394–403.
- Misner CW, Thorne KS and Wheeler JA (1973). "Gravitation". Freeman and Company.
- Montmerle T et al. (2006). "3. Solar System Formation and Early Evolution: the First 100 Million Years". In: *Earth, Moon, and Planets* 98.1-4, pp. 39–95.
- Moore P (2007). "Philip's Atlas of the Universe". 6th ed. Vol. 1. Philip's, p. 316.
- Mora A et al. (2016). "Gaia: focus, straylight and basic angle". In: *Monthly Notices of the Royal Astronomical Society*. Ed. by HA MacEwen et al. Vol. 462. 4, p. 99042D.
- Mortlock DJ et al. (2011). "A luminous quasar at a redshift of $z = 7.085$ ". In: *Nature* 474.7353, pp. 616–619.
- Netzer H (2015). "Revisiting the Unified Model of Active Galactic Nuclei". In: *Annual Review of Astronomy and Astrophysics* 53.1, pp. 365–408.
- O'Flaherty K (1997). "The Hipparcos and Tycho Catalogues: Astrometric and Photometric Star Catalogues derived from the ESA Hipparcos Space Astrometry Mission". Vol. 2. ESA.
- O'Mullane W et al. (2011). "Implementing the Gaia Astrometric Global Iterative Solution (AGIS) in Java". In: *Experimental Astronomy* 31, pp. 215–241.
- Ostlie DA and Carroll BW (2007). "An Introduction to Modern Astrophysics". 2nd ed. Pearson Education.
- Özel F et al. (2010). "The Black Hole Mass Distribution in the Galaxy". In: *The Astrophysical Journal* 725.2, pp. 1918–1927.
- Peebles PJE (1972). "Star Distribution Near a Collapsed Object". In: *The Astrophysical Journal* 178, p. 371.
- Peng CY et al. (2010). "Detailed Decomposition of Galaxy Images. II. Beyond Axisymmetric Models". In: *The Astronomical Journal* 139.6, pp. 2097–2129.
- (2002). "Detailed Structural Decomposition of Galaxy Images". In: *The Astronomical Journal* 124.1, pp. 266–293.
- Perryman MAC (2008). "Astronomical Applications of Astrometry". Cambridge University Press, pp. 1–670.
- (2011). "EAS Tycho Brahe prize lecture 2011 Hipparcos: A retrospective". In: *Astronomy and Astrophysics Review* 19.1.
- (1997). "The Hipparcos and Tycho Catalogues: Introduction and Guide to the Data". Vol. 1. ESA.
- (2010). "The Making of History's Greatest Star Map". 1st ed. Springer.
- Perryman MAC et al. (2014). "Astrometric Exoplanet Detection with Gaia". In: *The Astrophysical Journal* 797.1, p. 14.
- Perryman MAC et al. (2001). "GAIA: Composition, formation and evolution of the Galaxy". In: *Astronomy & Astrophysics* 35, pp. 48–49.
- Perryman MAC et al. (1997). "The HIPPARCOS Catalogue". In: *Astronomy and Astrophysics* 323, pp. L49–L52.
- Phinney E (1989). "Manifestations of a Massive Black Hole in the Galactic Center". In: *The Center of the Galaxy: Proceedings of the 136th Symposium of the International Astronomical Union*, p. 543.

- Piran T et al. (2015). "Disk Formation Versus Disk Accretion—What Powers Tidal Disruption Events?" In: *The Astrophysical Journal* 806.2, p. 164.
- Prusti T et al. (2016). "The Gaia mission". In: *Astronomy & Astrophysics* 595, A1.
- Pudritz RE (2002). "Clustered Star Formation and the Origin of Stellar Masses". In: *Science* 295.5552, pp. 68–76.
- Rau A et al. (2009). "Exploring the Optical Transient Sky with the Palomar Transient Factory". In: *Publications of the Astronomical Society of the Pacific* 121.886, pp. 1334–1351.
- Recio-Blanco A et al. (2016). "Stellar parametrization from Gaia RVS spectra". In: *Astronomy & Astrophysics* 585, A93.
- Rees MJ (1988). "Tidal disruption of stars by black holes of 106–108 solar masses in nearby galaxies". In: *Nature* 333.6173, pp. 523–528.
- Reynolds CS and Fabian AC (2008). "Broad Iron-K α Emission Lines as a Diagnostic of Black Hole Spin". In: *The Astrophysical Journal* 675.2, pp. 1048–1056.
- Rudolph A et al. (2014). "Gaia Mission Operations Concept and Launch and Early Orbit Phase - In-Orbit Experience". In: *SpaceOps 2014 Conference*. May. Reston, Virginia: American Institute of Aeronautics and Astronautics, pp. 1–19.
- Saxton RD et al. (2012). "A tidal disruption-like X-ray flare from the quiescent galaxy SDSS J120136.02+300305.5". In: *Astronomy & Astrophysics* 541, A106.
- Saxton RD et al. (2015). "Was the soft X-ray flare in NGC 3599 due to an AGN disc instability or a delayed tidal disruption event?" In: *Monthly Notices of the Royal Astronomical Society* 454.3, pp. 2798–2803.
- Schwarzschild K (1999). "On the gravitational field of a mass point according to Einstein's theory". In: 35.5, pp. 951–959.
- SDSS Collaboration et al. (2016). "The Thirteenth Data Release of the Sloan Digital Sky Survey: First Spectroscopic Data from the SDSS-IV Survey MAPPING Nearby Galaxies at Apache Point Observatory". In: *eprint arXiv* 1608, arXiv:1608.02013.
- Shapiro SL and Teukolsky SA (2004). "Black Holes, White Dwarfs, and Neutron Stars: The Physics of Compact Objects". Wiley-VCH.
- Shappee B et al. (2012). "The All Sky Automated Survey for Supernovae (ASAS-SiN)". In: *American Astronomical Society Meeting Abstracts #220*. Vol. 220. American Astronomical Society Meeting Abstracts, p. 432.03.
- Shcherbakov RV et al. (2013). "Grb060218 As a Tidal Disruption of a White Dwarf By an Intermediate-Mass Black Hole". In: *Edward C. Moran,1 Aaron J. Barth,2 Michael Eracleous,3 and Laura E. Kay* 85.
- Shiokawa H et al. (2015). "General Relativistic Hydrodynamic Simulation of Accretion Flow From a Stellar Tidal Disruption". In: *The Astrophysical Journal* 804.2, p. 85.
- Silk J and Rees MJ (1998). "Quasars and Galaxy Formation". In: *Monthly Notices of the Royal Astronomical Society* 324.1, pp. 128–140.
- Spruit H (2014). "Accretion disks". In: *Accretion Processes in Astrophysics*. Cambridge University Press, pp. 1–44.
- Stone NC (2015). "The Tidal Disruption of Stars by Supermassive Black Holes: An Analytic Approach". Cambridge: Springer.

- Stone NC and Metzger BD (2015). "Rates of stellar tidal disruption as probes of the supermassive black hole mass function". In: *Monthly Notices of the Royal Astronomical Society* 455.1, pp. 859–883.
- Strubbe LE and Quataert E (2009). "Optical flares from the tidal disruption of stars by massive black holes". In: *Monthly Notices of the Royal Astronomical Society* 400.4, pp. 2070–2084.
- (2011). "Spectroscopic signatures of the tidal disruption of stars by massive black holes". In: *Monthly Notices of the Royal Astronomical Society* 415.1, pp. 168–180.
- Tauris TM and van den Heuvel E (2003). "Formation and Evolution of Compact Stellar X-ray Sources". In:
- Thorne K (1995). "Black Holes & Time Warps: Einstein's Outrageous Legacy". WW Norton & Company.
- Trümper J (1982). "The ROSAT mission". In: *Advances in Space Research* 2.4, pp. 241–249.
- Vagg D et al. (2016). "GAVIP: A Platform for Gaia Data Analysis". In: 9913, pp. 1–19.
- Van den Bergh S (1998). "Galaxy Morphology and Classification". Cambridge University Press.
- Van Leeuwen F (2007). "Hipparcos, the New Reduction of the Raw Data". In: *Astrophysics and Space Science Library* 350.
- Van Leeuwen F et al. (2016). "Gaia Data Release 1: The photometric data". In: *Astronomy & Astrophysics* 30064.
- Van Velzen S and Farrar GR (2014). "Measurement of the Rate of Stellar Tidal Disruption Flares". In: *The Astrophysical Journal* 792.1, p. 53.
- Van Velzen S et al. (2015). "A radio jet from the optical and X-ray bright stellar tidal disruption flare ASASSN-14li." In: *Science (New York, N.Y.)* c.September 1961, science.aad1182–.
- Van Velzen S et al. (2011). "Optical Discovery of Probable Stellar Tidal Disruption Flares". In: *The Astrophysical Journal* 741.2, p. 73.
- Volker B and Shrader C (2012). "Active Galactic Nuclei". Wiley-VCH.
- Volonteri M, Haardt F and Madau P (2003). "The Assembly and Merging History of Supermassive Black Holes in Hierarchical Models of Galaxy Formation". In: *The Astrophysical Journal* 582.2, pp. 559–573.
- Voss R et al. (2011). "On the association of ULXs with young superclusters: M82 X-1 and a new candidate in NGC 7479". In: *Monthly Notices of the Royal Astronomical Society: Letters* 418.1, pp. 2007–2011.
- Vosteen LLa et al. (2009). "Wavefront sensor for the ESA-GAIA mission". In: *Proc. SPIE*. Ed. by PG Warren et al. Vol. 7439, p. 743914.
- Wald RM (1984). "General relativity". 1st ed. University of Chicago Press.
- Wang J and Merritt D (2004). "Revised Rates of Stellar Disruption in Galactic Nuclei". In: *The Astrophysical Journal* 600.1, pp. 149–161.
- Wyrzykowski Ł et al. (2017). "OGLE16aaa – a signature of a hungry supermassive black hole". In: *Monthly Notices of the Royal Astronomical Society: Letters* 465.1, pp. L114–L118.
- York DG et al. (2000). "The Sloan Digital Sky Survey: Technical Summary". In: *The Astronomical Journal* 120.3, pp. 1579–1587.
- Zauderer BA et al. (2011). "Birth of a relativistic outflow in the unusual γ -ray transient Swift J164449.3+573451." In: *Nature* 476.7361, pp. 425–428.

Appendix A

Analysis

As discussed in Section 3.7.2, one of the scientific areas which GAVIP aims to improve is reproducibility. AVIs are hosted in the cloud and may be made publicly available. This work may be useful for astronomers who wish to analyse Gaia TDE data in the future; however, due to the proprietary licence of GIBIS, this project was not packaged into an AVI. All analysis software produced in the course of this work, however, is publicly available on *GitHub* at <http://github.com/doloinn/tde-analysis>. Here it may be revised and improved with time.

This repository includes all code written in this project to generate the simulation inputs and to parse and analyse the outputs. As GAVIP is heavily integrated with git, it should be trivial to clone this repository into one's AVI in the future and apply the code. This software may also be used to inspect any of the analysis performed in this thesis.